Theses and Dissertations   1. Thesis and Dissertation Collection, all items

2022-03

ADVANCED HYBRID SOLAR CELL DESIGN

Logar, Kevin M.

Monterey, CA; Naval Postgraduate School

http://hdl.handle.net/10945/69674

NAVAL
POSTGRADUATE
SCHOOL

MONTEREY, CALIFORNIA

THESIS

ADVANCED HYBRID SOLAR CELL DESIGN

by

Kevin M. Logar

March 2022

Thesis Advisor:	Sherif N. Michael
Second Reader:	Todd R. Weatherford

Approved for public release. Distribution is unlimited.

THIS PAGE INTENTIONALLY LEFT BLANK

REPORT DOCUMENTATION PAGE		*Form Approved OMB No. 0704-0188*

Public reporting burden for this collection of information is estimated to average 1 hour per response, including the time for reviewing instruction, searching existing data sources, gathering and maintaining the data needed, and completing and reviewing the collection of information. Send comments regarding this burden estimate or any other aspect of this collection of information, including suggestions for reducing this burden, to Washington headquarters Services, Directorate for Information Operations and Reports, 1215 Jefferson Davis Highway, Suite 1204, Arlington, VA 22202-4302, and to the Office of Management and Budget, Paperwork Reduction Project (0704-0188) Washington, DC, 20503.

1. AGENCY USE ONLY *(Leave blank)*	2. REPORT DATE March 2022	3. REPORT TYPE AND DATES COVERED Master's thesis	
4. TITLE AND SUBTITLE ADVANCED HYBRID SOLAR CELL DESIGN			**5. FUNDING NUMBERS**
6. AUTHOR(S) Kevin M. Logar			
7. PERFORMING ORGANIZATION NAME(S) AND ADDRESS(ES) Naval Postgraduate School Monterey, CA 93943-5000			**8. PERFORMING ORGANIZATION REPORT NUMBER**
9. SPONSORING / MONITORING AGENCY NAME(S) AND ADDRESS(ES) N/A			**10. SPONSORING / MONITORING AGENCY REPORT NUMBER**
11. SUPPLEMENTARY NOTES The views expressed in this thesis are those of the author and do not reflect the official policy or position of the Department of Defense or the U.S. Government.			
12a. DISTRIBUTION / AVAILABILITY STATEMENT Approved for public release. Distribution is unlimited.			**12b. DISTRIBUTION CODE** A

13. ABSTRACT (maximum 200 words)

Interdigitated back surface contact (IBC) and copper indium gallium diselenide (CIGS) solar cells have been explored by multiple former Naval Postgraduate School (NPS) students with mutual independence. This thesis marries IBC and CIGS into a single cell to explore its optical parameters before introducing a novel cell design to reduce recombination in the absorber by establishing a vertical electric field. Implementing the novel design established up to a 7.5kV/cm electric field in the absorber to promote the separation of charge carriers, resulting in significant increases in short circuit current and I-V curve knee extension to raise cell efficiency to 24.32% at 300 K. Comparing this cell to optimal designs of prior theses, our cell boasts a 79.45% reduction in cell thickness and relative efficiency increase of 5.74%. Modeling of this cell demonstrates its potential for use in low weight, high power equipment such as UAVs, satellites, and solar blankets used by warfighters.

14. SUBJECT TERMS solar, photovoltaic, PV, advanced, hybrid, copper indium gallium diselenide, CIGS, IBC, back surface contact, novel design, interdigitated back surface contact, IBC			**15. NUMBER OF PAGES** 123
			16. PRICE CODE
17. SECURITY CLASSIFICATION OF REPORT Unclassified	**18. SECURITY CLASSIFICATION OF THIS PAGE** Unclassified	**19. SECURITY CLASSIFICATION OF ABSTRACT** Unclassified	**20. LIMITATION OF ABSTRACT** UU

NSN 7540-01-280-5500

Standard Form 298 (Rev. 2-89)
Prescribed by ANSI Std. 239-18

THIS PAGE INTENTIONALLY LEFT BLANK

Approved for public release. Distribution is unlimited.

ADVANCED HYBRID SOLAR CELL DESIGN

Kevin M. Logar
Lieutenant, United States Navy
BE, State University of New York Maritime College, 2015

Submitted in partial fulfillment of the
requirements for the degree of

MASTER OF SCIENCE IN ELECTRICAL ENGINEERING

from the

NAVAL POSTGRADUATE SCHOOL
March 2022

Approved by: Sherif N. Michael
Advisor

Todd R. Weatherford
Second Reader

Douglas J. Fouts
Chair, Department of Electrical and Computer Engineering

THIS PAGE INTENTIONALLY LEFT BLANK

ABSTRACT

Interdigitated back surface contact (IBC) and copper indium gallium diselenide (CIGS) solar cells have been explored by multiple former Naval Postgraduate School (NPS) students with mutual independence. This thesis marries IBC and CIGS into a single cell to explore its optical parameters before introducing a novel cell design to reduce recombination in the absorber by establishing a vertical electric field. Implementing the novel design established up to a 7.5kV/cm electric field in the absorber to promote the separation of charge carriers, resulting in significant increases in short circuit current and I-V curve knee extension to raise cell efficiency to 24.32% at 300 K. Comparing this cell to optimal designs of prior theses, our cell boasts a 79.45% reduction in cell thickness and relative efficiency increase of 5.74%. Modeling of this cell demonstrates its potential for use in low weight, high power equipment such as UAVs, satellites, and solar blankets used by warfighters.

THIS PAGE INTENTIONALLY LEFT BLANK

TABLE OF CONTENTS

LIST OF FIGURES

THIS PAGE INTENTIONALLY LEFT BLANK

LIST OF TABLES

THIS PAGE INTENTIONALLY LEFT BLANK

LIST OF ACRONYMS AND ABBREVIATIONS

A	Ampere, unit of current
a-Si	amorphous silicon
AM	air mass
ARC	anti-reflective coating
AZO	aluminum zinc oxide
BSF	back surface field
c	speed of light
C	Celsius, unit of temperature (metric scale)
CdS	cadmium sulfide
CdTe	cadmium telluride
CGS	copper gallium selenide
CIGS	copper indium gallium diselenide
CIS	copper indium selenide
CO_2	carbon dioxide
Cu	copper
D	diffusion constant
eV	electron volt
E_C	conduction band energy level
E_F	Fermi energy level
E_G	bandgap energy
E_V	valence band energy level
EHP	electron-hole pair
F	Fahrenheit, unit of temperature (empirical scale)
FF	fill factor
FSF	front surface field
Ga	gallium
GaAs	gallium arsenide
Ge	germanium
h	Planck's constant
ħ	reduced Planck's constant

I	current
I_D	diffusion current
I_{MP}	max power peak current
I_S	drift current
I_{SC}	short circuit current
IBC	interdigitated back surface contact
In	indium
InP	indium phosphide
J	current density
J	Joule, unit of energy
J_{SC}	short circuit current density
k	Boltzmann constant
k	wave vector
K	Kelvin, unit of temperature (absolute scale)
L	diffusion length
m	meter, unit of length (metric scale)
Mo	molybdenum
O	oxygen
O_3	ozone
P	power
P_{MP}	max power peak power
PV	photovoltaic
q	electron charge
R	resistance
s	second, unit of time
Se	selenium
Si	silicon
SQ	Shockley-Queisser
SRH	Shockley-Read-Hall
V	voltage
V_{Br}	breakdown voltage
V_F	turn on voltage

V_{MP}	max power peak voltage
V_{OC}	open circuit voltage
Zn	zinc
ZnO	zinc oxide
α	absorption coefficient
η	efficiency
θ_z	zenith angle
μ	mobility
μ_n	electron mobility
μ_P	hole mobility
ε	permittivity
ρ	resistivity
σ	conductivity
τ	carrier lifetime
χ	electron affinity
Ω	Ohm

THIS PAGE INTENTIONALLY LEFT BLANK

ACKNOWLEDGMENTS

I would like to thank my advisor, Dr. Sherif Michael, and the ECE department staff at NPS for their guidance and support in helping me complete this thesis. I would also like to thank my family for encouraging me to keep charging and complete my studies.

THIS PAGE INTENTIONALLY LEFT BLANK

I.   INTRODUCTION

Many individuals and governments worldwide have made personal and operational changes to reduce their carbon footprint by shifting from fossil fuels to renewable energy sources. As technology continues to integrate its way into almost every aspect of life, power demands rise as we further incorporate rechargeable energy storage devices into modern gadgets. Integration of solar power into property energy systems and beyond has become commonplace to combat climate change, placing high demands on high efficiency cells. As silicon (Si) cell performance approaches its theoretical maximum, different materials have been introduced and researched in hopes of surpassing standing power and efficiency limits. Novel cell designs such as interdigitated back surface contacts (IBC) have also been explored as part of these research efforts, yielding increased short circuit currents and efficiencies.

Despite their heavy use from a utility standpoint, solar energy has many government and military applications too. From powering satellites and interplanetary rovers for NASA to portable devices used by warfighters, implementing solar power comes with additional challenges. Space-specific cells must be lightweight, highly efficient and radiation hardened (rad-hard) to maximize useful life of the spacecraft and minimize launch costs. Battlefront applications such as solar portable alternative communications energy system (SPACES) used by Department of Defense must be lightweight, portable, and physically rugged to withstand handling and environmental abuse. Based on such constraints, normal terrestrial use cells will need to meet mission objectives. For these reasons, cells such as copper indium gallium diselenide (CIGS) have been incorporated for their rad-hard, high-power characteristics.

A.   OBJECTIVE

While still relatively new in the world of photovoltaics, published IBC cell designs have been limited. SunPower explored IBC using polysilicon [1], promoting O'Connor [2] to explore the use of GaAs with an IBC design. The motivation for this thesis is to combine the advantages of IBC and CIGS into a single cell to determine its optical parameters under

nominal (AM1.5) conditions via simulation in Silvaco. To accomplish this, we will first simulate a conventional CIGS IBC design architecture. Upon verification that our model works and obtaining baseline optical parameters we will explore a novel design in which a vertical p-n junction is created to further promote the separation of charges in the absorber to minimize recombination losses. This design was first investigated by Herrera [3] in 2017, however additional variations, such as region sizing, are taken into consideration in this thesis.

B.   PAST WORK

Several Naval Postgraduate School (NPS) graduates have published research regarding the use of an IBC architecture and CIGS with mutual independence. Fotis [4] and Columbus [5] modeled CIGS solar cells in Silvaco with a conventional cell design, focusing on optimization via altering thicknesses and interchanging layer materials. Green [6] and O'Connor [2] modeled IBC cell architectures in Silvaco using Si and GaAs, respectively. Herrera [3] attempted to marry CIGS and IBC via Silvaco simulation, introducing a novel design to assist in the separation of charge carriers in the absorber region; however, the scope of his research was limited. Modeling techniques and optimal performance data from all the listed theses will be used to meet the objective of this thesis.

C.   ORGANIZATION

Chapter II provides a basic overview of the atomic and semiconductor physics essential to understanding the functionality of solar cells. Chapter III discusses basic solar cell operations, including the differences in conventional and IBC cell designs. Chapter IV provides a brief introduction to the Silvaco Atlas modeling software used in this thesis. Chapter V gives and in-depth explanation of all research completed prior to commencing modeling as well as a detailed analysis of all results found. Lastly, Chapter VI lists this the conclusion of this thesis and recommendations for future research.

II.   BACKGROUND

A.   ATOMIC PHYSICS

This chapter provides a review of atomic and semiconductor physics. It is assumed that the reader has a background in general sciences to understand the language used herein. Those with a background in these topics may skip to Chapter III.

Advances in atomic theory have come a long way since their dawn by the Greek philosophers Leucippus and Democritus in the fifth century B.C. To date, the most popular atomic model is that proposed by Niels Bohr in 1913, stating that electrons occupy quantized energy states, or shells, surrounding a positively charged nucleus. These electrons may transfer to different energy shells upon gaining or giving up energy but may not occupy the space between the states. The farther away from the nucleus the electron gets, the more potential energy it has and vice versa. The outermost shell in which an electron occupies is called the valence shell. At 0 K, all electrons are held tightly in place. However, as temperature rises, electrons gain kinetic energy and valence electrons begin to break free from their orbit. These are called free electrons and are directly responsible for the electrical conductivity of the material. An example of Bohr's atomic model is shown in Figure 1.
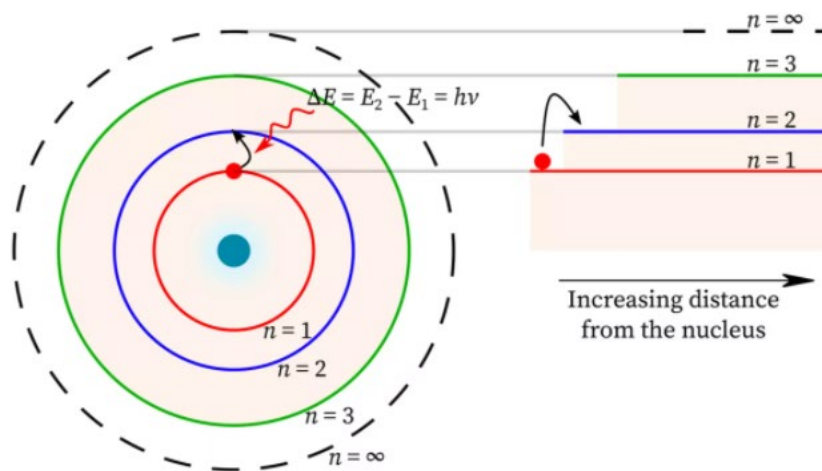
Figure 1.   Bohr's model of the atomic structure. Source [7].

Because there are seven energy levels which an electron may occupy, there are seven periods in the periodic table. Within each energy level there are four subshells, dictated as the S, P, D, or F, with S containing the least energy and F containing the highest energy. The orbital shape and number of electrons held is determined by which subshell is to be occupied, summarized in Table 1. The order in which the shells will be filled is 1s 2s 2p 3s 3p 4s 3d 4p 5s 4d 5p 6s 4f 5d 6p 7s 5f 6d 7p. The Pauli exclusion principle dictates that no two electrons may have the same quantum energy and spin; therefore, atomic orbitals may split into N discrete molecular orbits within a molecule containing N identical atoms. This leads to approximately 10^{22} closely packed energy states, where the energy level difference of each state is infinitesimal so that they may be considered continuous as an energy band. As shown in Figure 2, two energy bands exist, the conduction band and the valence band, the former containing higher negative (electron) energies or free electrons and the latter containing the lower energy electrons held tightly by their host atom. The difference between the highest energy of the valence band (Ev) and the lowest energy of the conduction band (Ec) is called the band gap (Eg) and is an important characteristic in determining the behavior of many materials. No energy states exist within the bandgap; therefore, it is often referred to as the forbidden zone.

Table 1.   Energy levels and subshell configuration. Source: [8].

Energy Level	Subshells	# of orbitals	# of electrons it can hold
1	1s	1	2
2	2s	1	2
	2p	3	6
3	3s	1	2
	3p	3	6
	3d	5	10
4	4s	1	2
	4p	3	6
	4d	5	10
	4f	7	14
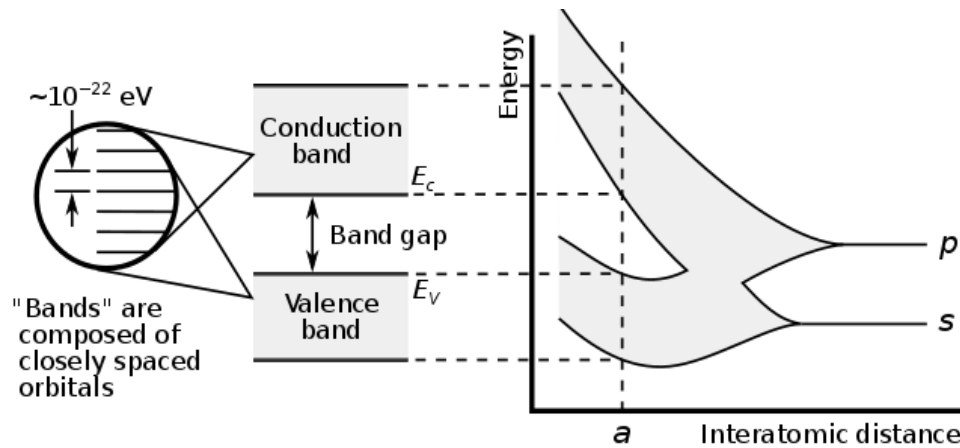
Figure 2.   Band construction and bandgap. Source: [9].

Orientation of the conduction and valence bands within a material are an important electrical property. As shown in Figure 3, materials with overlapping bands are conductive in nature (promote flow of electrons) and large bandgap materials are electrical insulators (inhibit electron flow). Consequentially, conductors have very low resistivity whereas insulators have very high resistivity. Materials containing overlapping bands are dubbed degenerate. Moderate bandgap materials are called semiconductors and located in Group IV (exclusively) on the periodic table. Semiconductors play an important role in many modern electronic devices for their ability to act as a conductor or insulator depending on their environment and use. Such devices include, but are not limited to, diodes, transistors and thyristors and are commonly made of silicon (Si) or germanium (Ge) due to their electrical properties, abundance, and cost benefits. Compound semiconductors can also be realized by combining different Groups of materials so long as the valence shell remains full, such as III-V and II-VI compounds. Examples of such materials are gallium arsenide (GaAs), indium phosphide (InP), cadmium sulfide (CdS), and zinc oxide (ZnO).
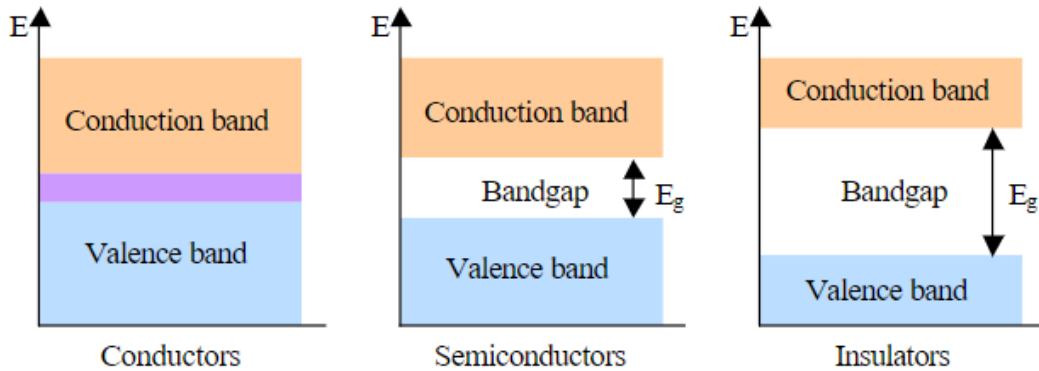
Figure 3.   Energy band orientation in various materials. Source: [10].

To achieve chemical stability, atoms require full valence shells. Except for the first shell containing two electrons, a complete valence shell always contains eight electrons. To achieve this stability, atoms with five or more electrons in their outer shell (Groups V+) will attract free electrons, increasing the net negative charge of the atom. The resultant stable atom is a negative ion. On the contrary, atoms with three or less electrons (Group III-) will seek to give up their outermost electrons to achieve stability, thus increasing their net positive charge and become a positive ion. When two ions of opposite polarity are attracted to each other, an ionic bond is formed. However, Group IV atoms do not give up or gain electrons to fill their outer shell. Instead, these atoms share their valence electrons with their neighbors to form covalent bonds.

Based on the resultant electrostatic forces imposed on each neighboring atom within a material, different symmetric lattices are formed. Each type of lattice creates a different unit cell, often called a crystal. Three types of unit cells exist, called simple cubic, body centered cubic, and face centered cubic, containing a total of one, two, and four atoms, respectively, as shown in Figure 4. Each crystal structure is defined by a lattice constant, which refers to the physical dimension of the unit cell. Matching of lattice constants is important in constructing compound semiconductor devices because it minimizes internal stress, ensures minimal defects are formed, and allows for a smooth transition between bandgaps without a change in crystalline structure.
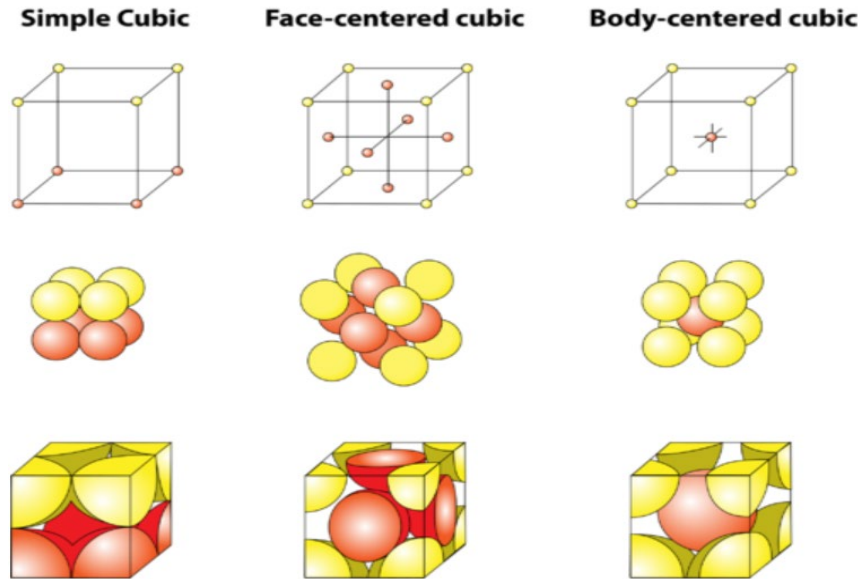
Figure 4.   Unit cell configurations. Source: [11].

As the electrons of a semiconductor absorbs energy, due to temperature or outside forces, they may gain enough energy to break their covalent bonds and become free. The resultant loss of an electron will leave behind a net positive charge on the host atom and a vacancy, called a hole. Holes contain and same magnitude charge as the electron, but positive, and are located where the free electron in the conduction band used to be. Both the free electron and hole are called an electron hole pair (EHP) and the process of their creation is called ionization or generation. As free electrons move throughout a crystal, they may combine with holes to cause the EHP to "disappear" via a process called annihilation or recombination. Several different recombination mechanics exist, as will be discussed later. The rate of generation and recombination within a material are strongly dependent on temperature and the concentration of EHPs within the material. In thermal equilibrium, rate of generation and recombination are equal to maintain a constant number of EHPs within the material.

Pure semiconductors, those that contain no foreign atoms, and called intrinsic semiconductors. At 0 K, no EHPs exist; however, the number of EHPs will increase logarithmically as temperature is increased. Since free electrons are responsible for conductivity, conductivity also rises due to this temperature change. The EHPs generated

are called intrinsic carriers and are only a fraction of the total number of atoms within the device. Intrinsic carries play an important role in the behavior of electronic devices.

Impurities, called dopants, may be added to intrinsic materials to alter their electrical properties. Group III materials are called acceptors since the tri-valent atom will seek to accept an electron from the intrinsic material to behave like a semiconductor, becoming net negatively charged. Conversely, Group V materials are called donors since their penta-valent atom will donate an electron to behave as a semiconductor, becoming net positively charged. Materials doped with acceptors are called p-type while those doped with donors are called n-type. The process of adding dopants to an intrinsic material is called doping and yields important electrical property changes to the new extrinsic material. Intrinsic and doped semiconductors are shown in Figures 5 and 6. Sometimes both types of doping are used to offset the unwanted impurities that exist within the intrinsic material and is called a compensated semiconductor.
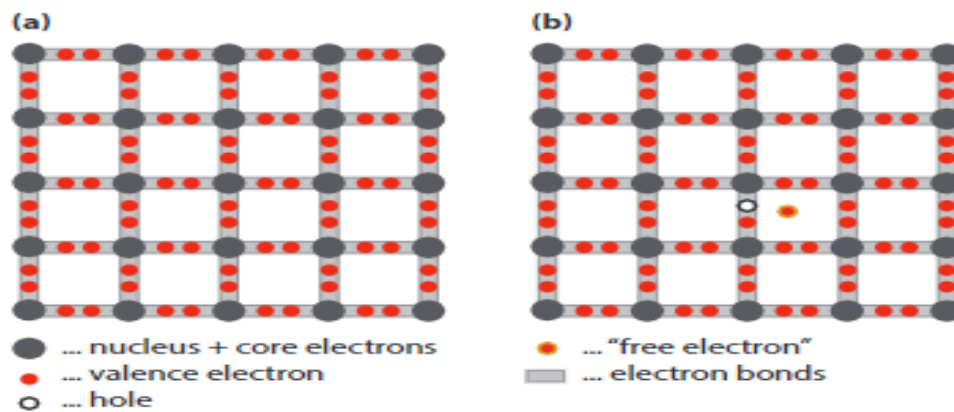
Figure 5.   Intrinsic semiconductor without EHP (a) and with EHP (b).
Source: [12].
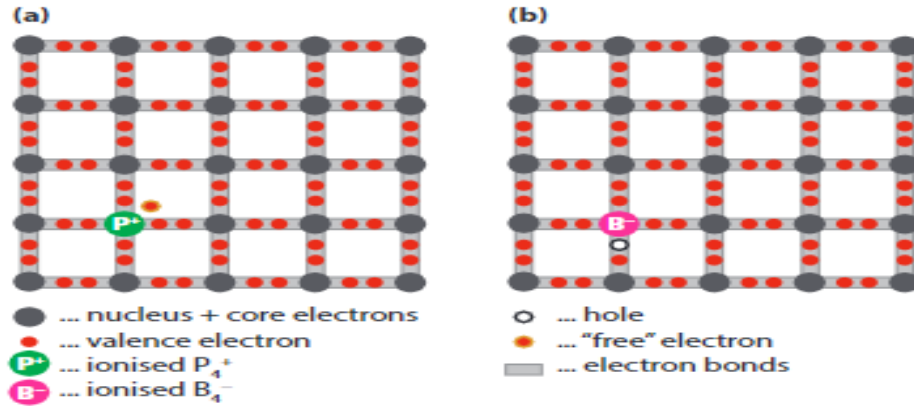
Figure 6.   N-type doping (a) and p-type doping (b). Source: [12].

The Fermi level of a material, E_F, is the hypothetic energy level of an electron such that it has a 50% chance of being occupied at any given time. This concept arises from the Heisenberg uncertainty principle, stating that there is an inherent uncertainty in the act of measuring the characteristics of a particle, such as position, velocity, momentum, and energy level. E_F, calculated by Equation 1, is approximately in the middle of the bandgap for intrinsic semiconductors but will vary based on doping concentrations (Figure 7) and temperature (Figure 8). Since n-type doping yields a net higher electron energy, the E_F will rise closer to the E_C while the opposite is true for p-type doping. The right most graphs in Figure 7 denote the density of electron energies within the given material.

$$f(E) = \frac{1}{1 + e^{(E-E_F)/kT}}$$

(2)
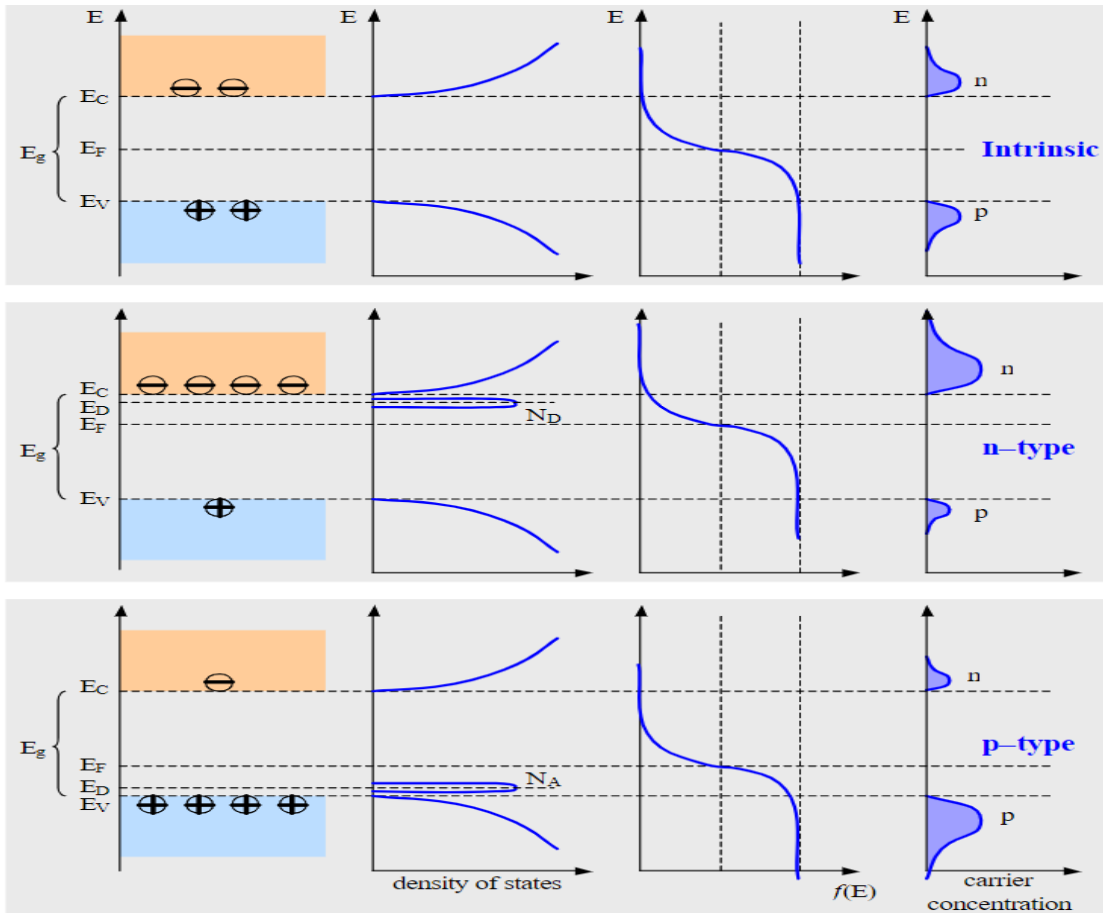
Figure 7.   Fermi level based on doping. Source: [10].
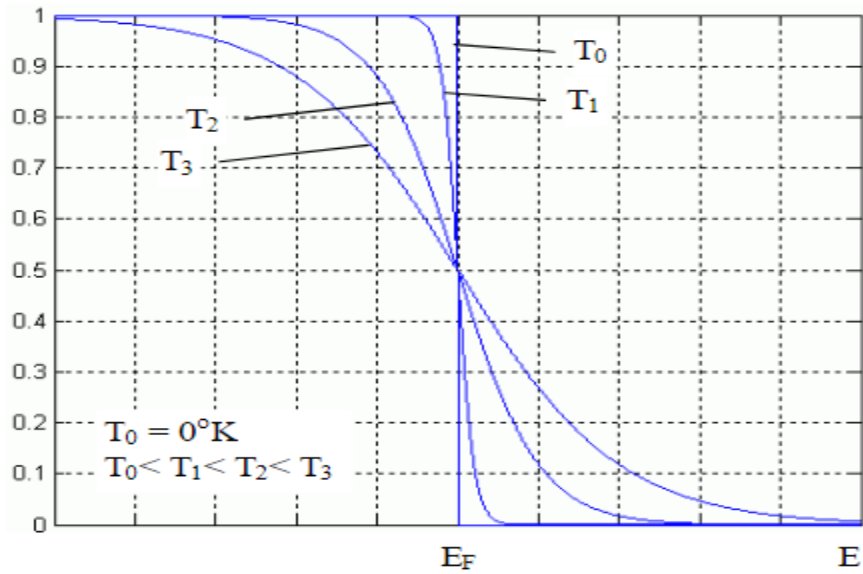
Figure 8.   Fermi level based on temperature. Source: [10].

Crystal momentum, defined by Equation 2, is a momentum-like vector associated with electrons within a crystalline lattice. When plotting energy versus the wave vector, k, materials in which the maximum E_V and minimum E_C align at the same k are called direct band gap materials while those with mismatched k values are called indirect band gap materials. The distinction between a direct and indirect band gap plays a major role in how recombination will ultimately occur.

$$P_{Crystal} = \hbar k$$

(3)

In direct band gap materials, electrons and holes will recombine without a change in crystalline momentum. Recombination rate will be the highest in this kind of material, and therefore, the lifetime of the carriers will be the shortest. EHP recombination of this type will result in the emission of a photon and is called radiative recombination. In indirect band gap materials, a change in crystalline momentum is required for electrons and holes to recombine. The energy required to be released to cause recombination is given up by emission of a phonon, or a vibration in the crystal lattice. This is called non-radiative recombination. The vibration will ultimately be lost as heat within the device and is an inherent loss.

When doping or crystalline defects are present, energy states are created within the band gap and may trap an electron while it transitions between bands. At these localized sites, non-radiative recombination will occur, and a phonon will be released. This recombination method is called Shockley-Read-Hall recombination (SRH), or trap-assisted recombination. SRH is the dominant recombination method within indirect band gap materials but may be dominant in direct bandgap materials under certain conditions. Conversely, Auger recombination is when a third particle is excited further into its energy band upon annihilation of an EHP. The highly excited particle will subsequently lose its excess energy in the form of thermal vibrations (non-radiative). This effect is normally only significant in very high carrier density, non-equilibrium conditions. Lastly, surface recombination is a trap-assisted recombination that occurs at a trap site, such as a dangling bond, near the surface of a semiconductor device. This type of recombination may play a dominant role in solar cell applications and requires passivation techniques to be used in order to minimize such loses. All loss mechanics can be seen graphically in Figures 9 -11.

11
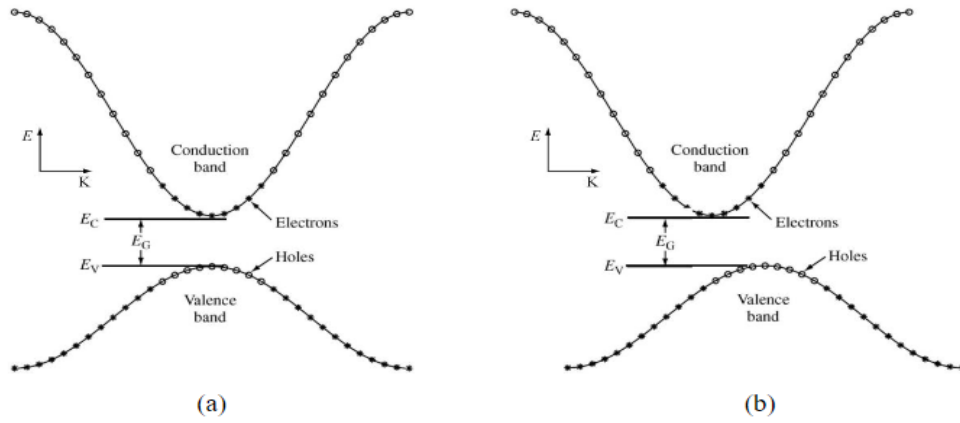
Figure 9.   Direct band gap (a) and indirect band gap materials (b). Source: [2].
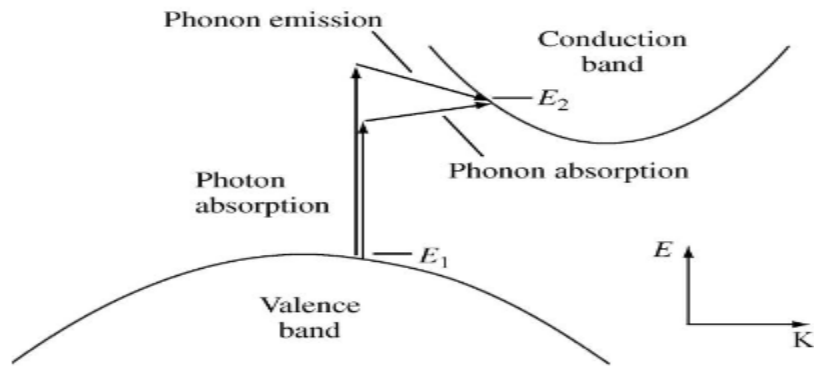
Figure 10.   Radiative and non-radiative recombination effects. Source: [2].
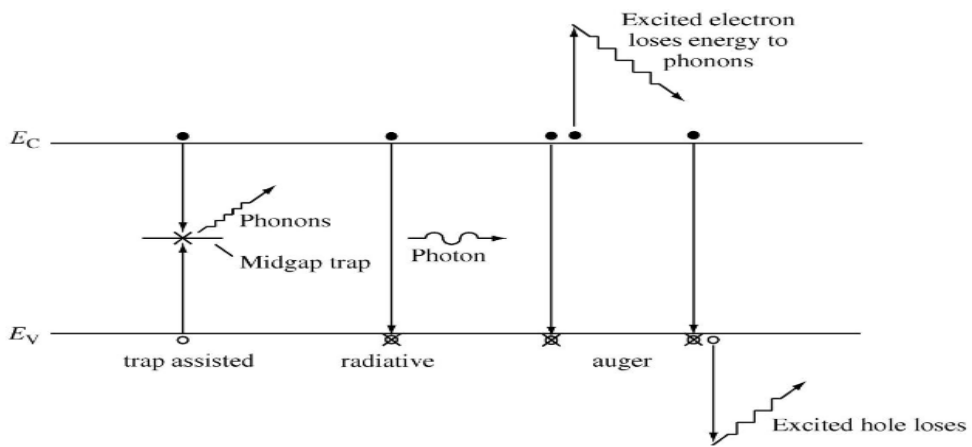
Figure 11.   Recombination processes. Source: [2].

B. SEMICONDUCTOR PHYSICS

Placing a p-type and n-type semiconductor together has unique properties. The interface between the two materials, known as the p-n junction or heterojunction, is responsible for the built-in voltages and functionality observed within modern electronics such as diodes, transistors, and solar cells. We will now explore this region in detail.

First, it is important to discuss the difference between the type of currents within semiconductors, namely diffusion and drift currents. Diffusion current (I_D) exists due to the higher concentration of carrier within one part of the semiconductor, resulting in particle movement to achieve an even distribution across the entire device. This effect is analogous to gas expanding in its container. Diffusion current is calculated by Equation 3.

$$J_{Diff,n} = qD_n \frac{dn}{dx} \quad or \quad J_{Diff,p} = -qD_p \frac{dp}{dx} \tag{4}$$

Movement of charges due to the presence of an external force, such as an electric field, is called drift current (I_S). This current will be proportional to the electric field intensity, temperature and minority charge carrier density within the device and can by calculated by Equation 4. It is important to note that both types of current are defined by the direction of motion of positive charges (holes in this case) and is therefore opposite to electron movement.

$$J_{Drift,n} = qn\mu_n E \quad or \quad J_{Drift,p} = -qp\mu_p E \tag{5}$$

As electron drift within a material, collision with other atoms within the lattice and electrostatic forces of charged impurities will slow the electron down until a constant velocity is achieved, called drift speed (v_D). The ratio of drift speed to the magnitude of the applied field is called mobility (μ) and will lower due to increased impurity concentration and rising temperatures due to scattering. Mobility is material dependent and can be calculated by Equation 5.

$$\mu_n = \frac{|v_{D,n}|}{E} \quad or \quad \mu_p = \frac{|v_{D,p}|}{E} \tag{6}$$

Under equilibrium conditions, the excess carriers on each side (holes in p-type, electrons in n-type) will diffuse across the junction to combine with the opposite carrier. In the local vicinity of the junction, a region void of charge carriers, known as the depletion

region, is now present with positively charged ions remaining on the n-type side and negatively charged ions on the p-side. This phenomenon establishes an electric field across the depletion region and will slow further diffusion of charges until an equilibrium is established. The electric field will also sweep electrons from the p-type to the n-type and holes from the n-type to the p-type. In this condition, the Fermi level on both sides must remain the same and therefore a bending of the valence and conduction bands occurs. A representation of a p-n junction is shown in Figure 12 and its associated band diagram in Figure 13.
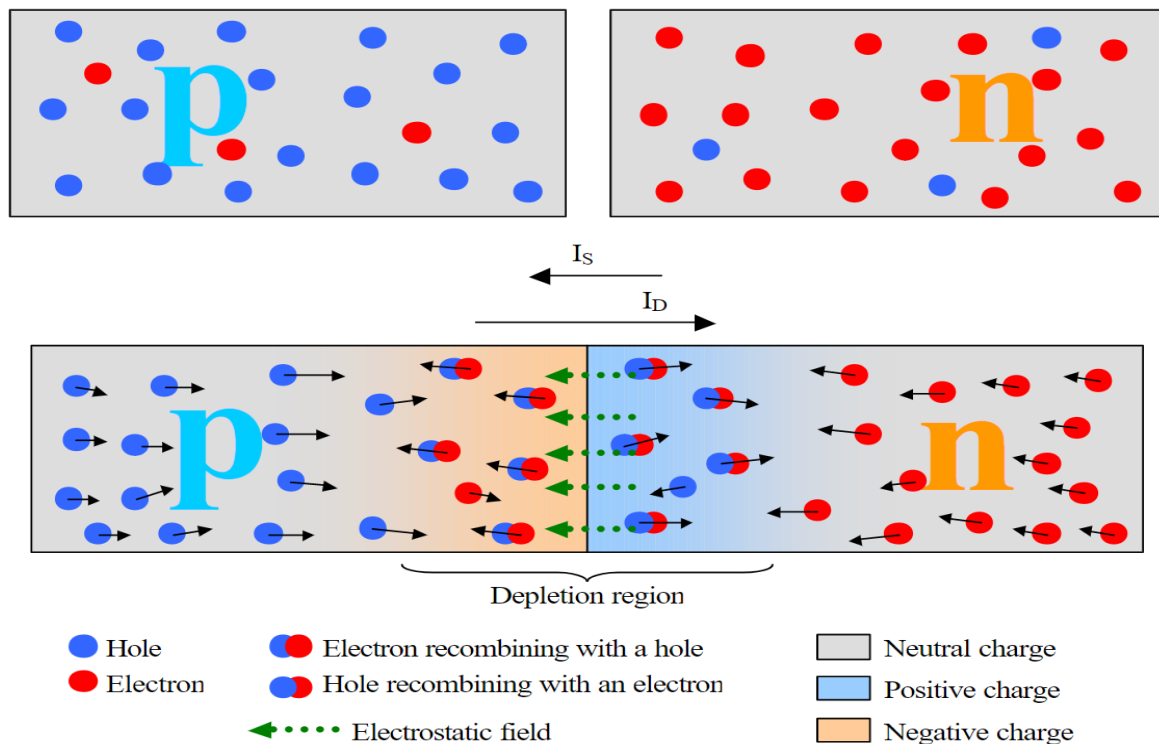
Figure 12. P-n junction and its electric field. Source: [10].
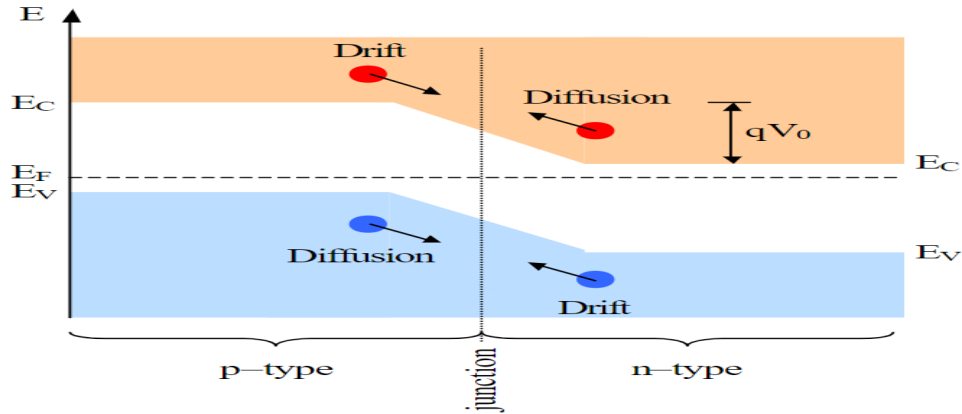
Figure 13.   Equilibrium band diagram. Source: [4].

Applying a voltage source across the junction with the positive lead on the p-type side and negative lead on the n-type side is called a forward bias. In this condition, many majority carriers are supplied to their respective sides of the device and will diffuse across the junction. Additionally, the external voltage source will neutralize the internal voltage, narrowing the depletion region. At steady state, I_S becomes very small and $I \approx I_D$, which is very large. Since the device is no longer in equilibrium due to the external field provided, the Fermi levels will no longer be equal but will be separated by the magnitude of the applied voltage. These unequal Fermi levels are called the quasi-Fermi levels. Figure 14 shows the new band diagram under the forward biased condition. Measuring the current out of the device gives us the characteristic curve of the p-n junction, as shown on the positive x-axis side of Figure 16. Note that after the turn-on voltage, V_F, a small voltage change will result in a large current change. V_F is material dependent, such as 0.7 V for Si and 0.3 V for Ge.
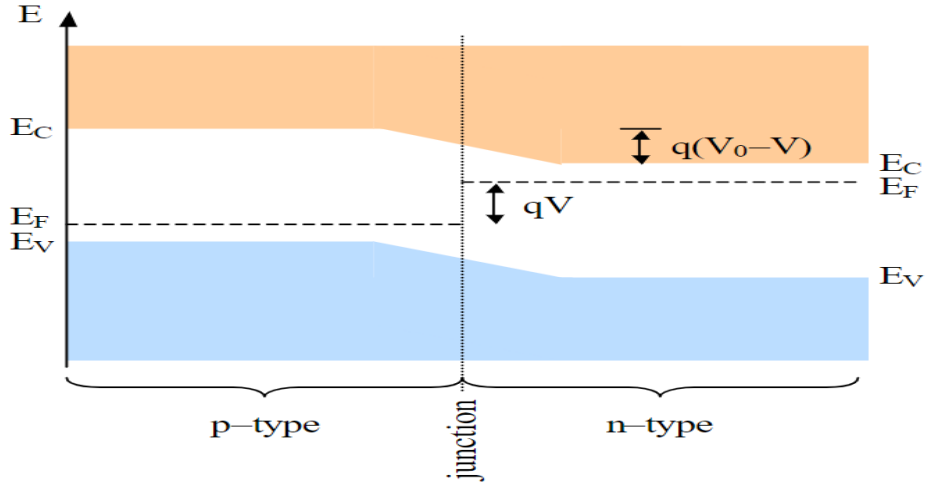
Figure 14.   Forward bias band diagram. Source: [4].

Switching the voltage polarity applied to the device yields a reversed bias condition. Here, the supplied carriers will recombine with the excess carries of the device, causing a widening of the depletion region and increase in internal voltage. In steady state, I_D becomes negligible and $I \approx I_S$, which is very small. The resulting band diagram for the reversed biased case is shown in Figure 15 and its characteristic curve resides on the negative x-axis portion of Figure 16. It is important to note that the current produced in this condition is not zero and referred to as the leakage current.
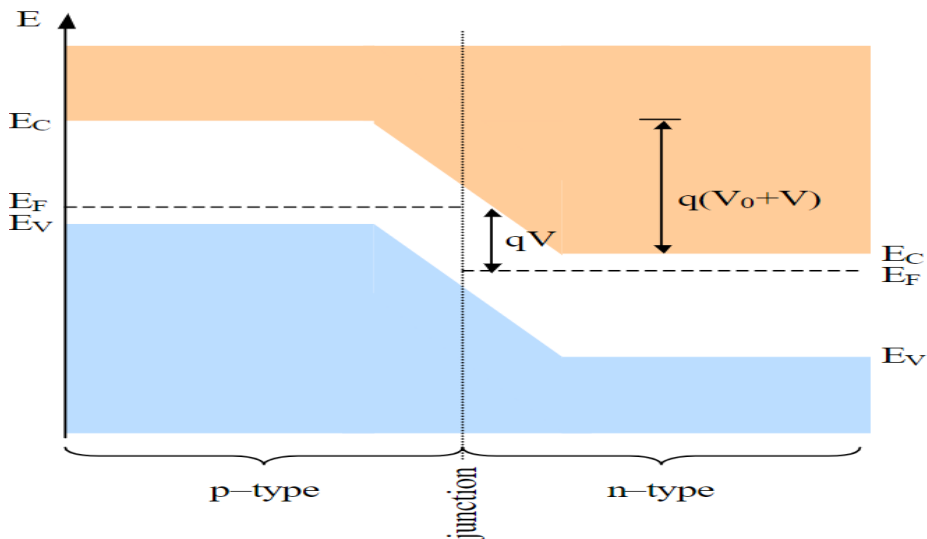
Figure 15.   Reverse bias band diagram. Source: [4].

If the reversed bias voltage is increased, we will reach our first method of breakdown known as the Zener effect. At this voltage, the internal electrostatic field becomes strong enough to strip electrons from their covalent bonds, creating EHPs. These minority carriers are swept to the opposite side, generating a current that can become quite large. The device will begin to behave as if it were forward biased but with an opposite current direction. Like the forward biased case, only a small increase in reverse biased voltage at the Zener breakdown voltage is required to produce a large change in current.

If we increase the reversed bias even further, we will reach our second breakdown method known as the avalanche effect. At this point, the minority carriers traveling through the depletion region have such high kinetic energy that their collisions with atoms will also break covalent bonds and create EHP. In addition, the EHPs generated by this method will also have enough kinetic energy to create even more EHPs, continuing the avalanche-type effect. Generated minority carriers will continue to be swept to the opposite side of the device and current will increase exponentially. This effect is more abrupt than the Zener effect, however, neither are destructive to the device if voltage and current, and therefore dissipated power, remain within their rated limits based on physical construction. For Si, the Zener effect will be dominant at $V_{Br} < 5V$ and the avalanche will dominate at $V_{Br} > 7V$. Between the onset of the Zener effect and avalanche effect, either or both effects contribute to the rise in current. The breakdown region of a p-n junction is shown in Figure 16.
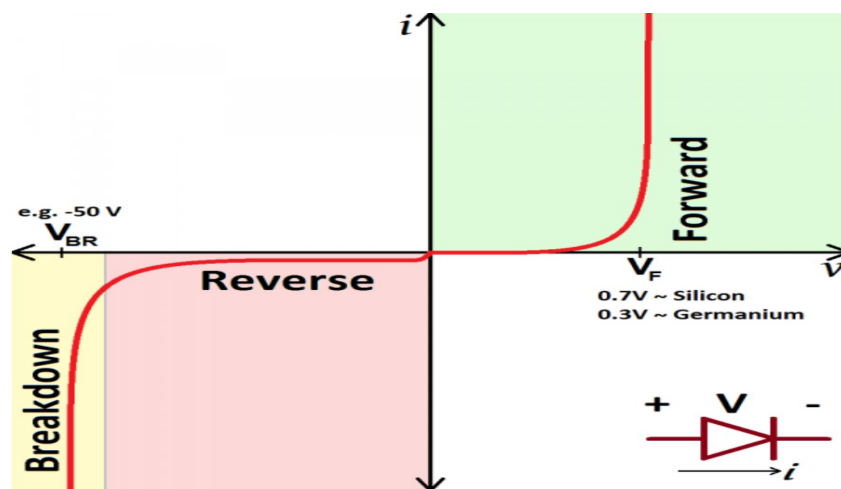
Figure 16. P-n junction characteristic curve. Source: [13].

17

THIS PAGE INTENTIONALLY LEFT BLANK

III. SOLAR CELLS

A. SOLAR SPECTRUM

The basic construction of solar cells, commonly referred to as photovoltaic (PV) cells, mimics that of a p-n junction used in electronic devices with a few extra components. Conventional photovoltaics consist of an electrical grid resting on top of a vertically stacked p-n junction with a second electrical contact on bottom to support connection to an electrical load. Unfortunately, a cell of this exact makeup will have very poor efficiency due to various phenomena originating from the interaction of sunlight with PV materials and the physics of EHP generation and collection. In this chapter, we explore the solar irradiance spectrum, PV cell construction, material considerations, concepts of operations, loss mechanics and limitations.

To understand the fundamentals of solar cells, we first need to understand the solar irradiance spectrum incident at various locations. Specifically, we need to study the ways in which energy will be lost prior to sunlight impacting our solar cell to produce useful work. In addition, we need to define industry standards to be able to calculate the optical parameters which will be used to quantify cell performance metrics. To denote the environment in which we wish to study, we use the concept of the air mass (AM). AM is "the path length that light travels through the atmosphere normalized to the shortest possible path length.[14]" It quantifies the reduction in power the light experiences as it passes through the atmosphere, is calculated by Equation 6 and shown in Figure 17. Under ideal conditions, our cells on Earth will always operate at AM1, where the sunlight is perpendicular to the front surface. However, a more realistic standard is to use AM1.5 to compensate for the fact that the sun must travel overhead in an orbital manor. Table 2 summarizes AM conditions and their approximate power as numbers vary by source. While the real output power at AM1.5 is approximately 900 W/m^2, 1 kW/m^2 is an accepted industry standard for ease of calculations.

$$AM = \frac{1}{\cos(\theta_z)}$$

(7)
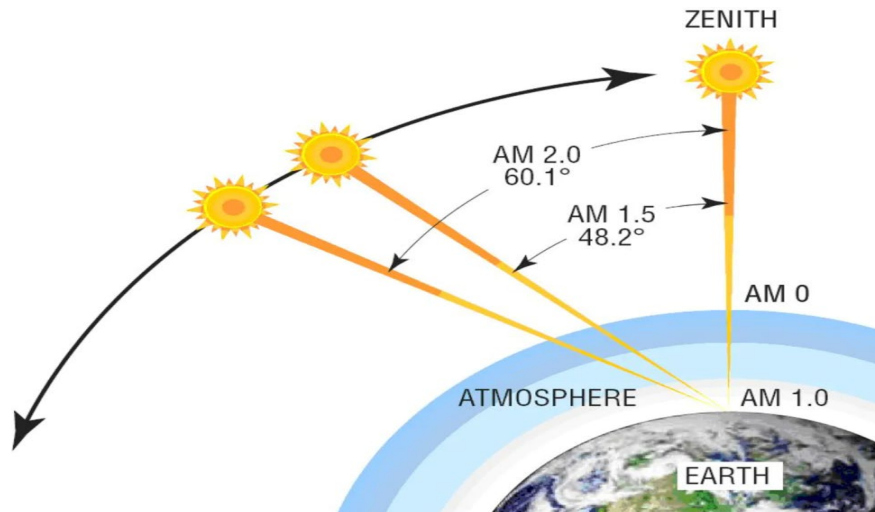
Figure 17.   AM conditions. Source: [15].

Table 2.   Spectral distribution conditions. Adapted from [14],[16].

Location	Zenith Angle (θ_z) [deg]	Approx. Incident Power [W/m^2]	AM Condition
Outside Atmosphere	N/A	1365	AM0
Surface	90	900	AM1
Surface	48.2	900 (1000 Standard)	AM1.5
Surface	60.1	800	AM2

The surface of the sun can be viewed as a black body radiation source with a temperature of 6000 K and energy spectrum, shown in Figure 18. The spectrum outside the Earth atmosphere, denoted as AM0 since zero atmosphere has been traversed, already experiences losses due to the total power of the light spreading out over a much larger surface area during its transit to Earth. When passing through the atmosphere, additional losses are accrued due to absorption, scattering and reflection from ozone (O_3), airborne particulates (dust, pollution, etc.), water vapor (humidity, clouds, rain) and carbon dioxide (CO_2). Importantly, these losses do not affect all wavelengths equally and a change in the incident spectrum occurs. A summary of these loss mechanics is shown in Figure 18 and

their effects on the AM spectrum are shown in Figure 19. Comparing the AM0 and AM1.5 curves of Figure 19, we can clearly see that a wavelength greater than 1000 nm is particularly susceptible to attenuation by the mechanics discussed in this section.
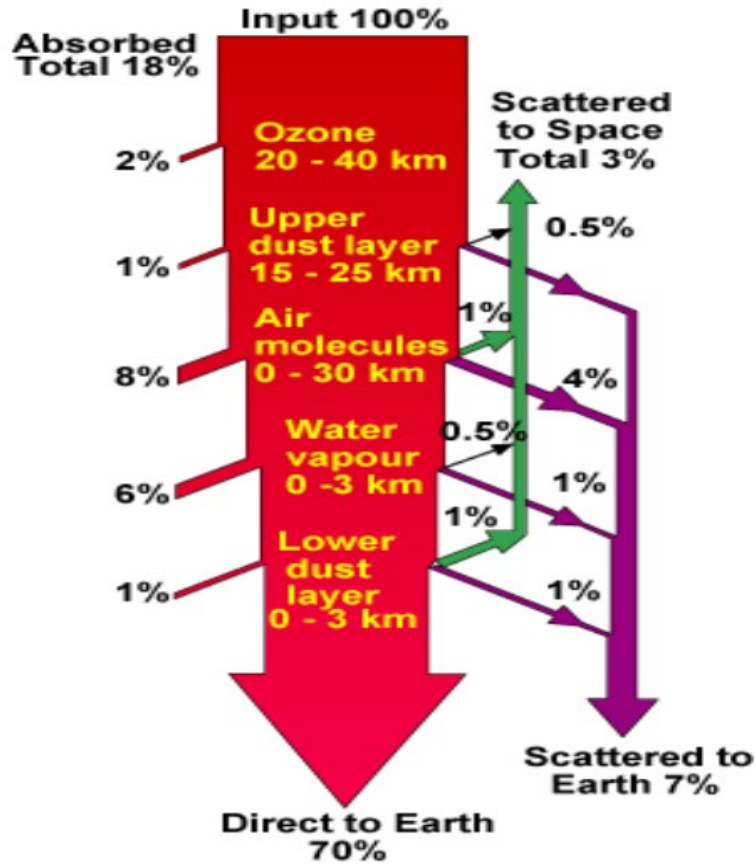
Figure 18.   Spectral intensity loss mechanics. Source: [3].
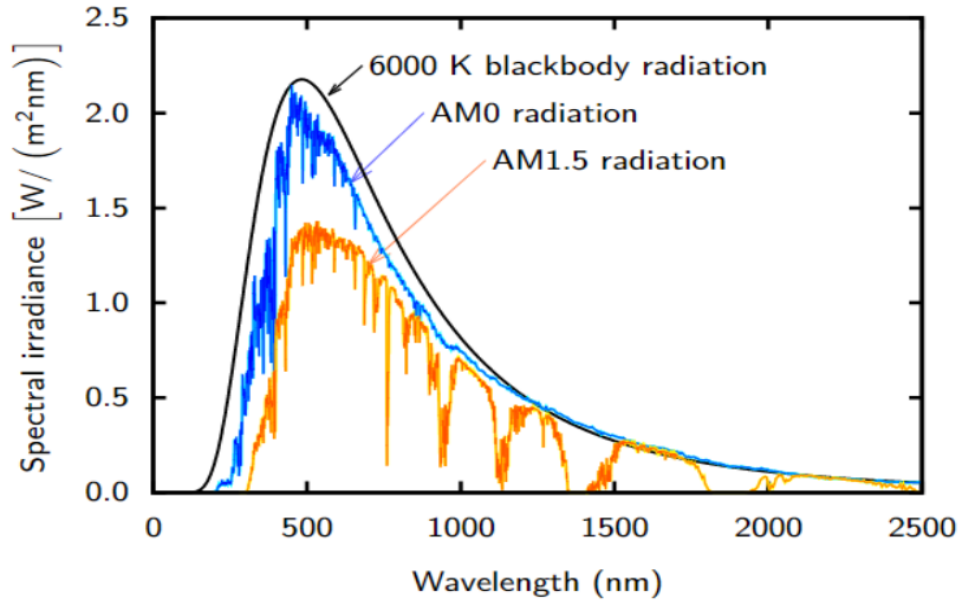
Figure 19.　Spectral irradiance vs. wavelength for different AM conditions.
Source: [12].

Equation 7 relates wavelength and energy. This equation is specifically important in PV studies because it allows us to identify which wavelengths can be used to generate EHP in cells with different bandgaps. Wavelengths with energy lower than that of the bandgap provide insufficient energy for generation and will be transmitted through the cell without being absorbed. In contrast, energies above the bandgap energy will excite electrons well above the conduction band energy, the difference of which will be lost as heat due to vibration as the electron deexcites to the lowest available state. Both phenomena combined is called spectral mismatch and is the main loss during the energy conversion process [12]. Since the spectral irradiance cannot be controlled, significant compromise and optimization must be considered to ensure maximum generation and collection occurs for a given bandgap. Figure 20 demonstrates this concept for various PV materials on the market today.

$$E = \frac{hc}{\lambda} = \frac{1.24}{\lambda_{\mu m}}$$

(8)
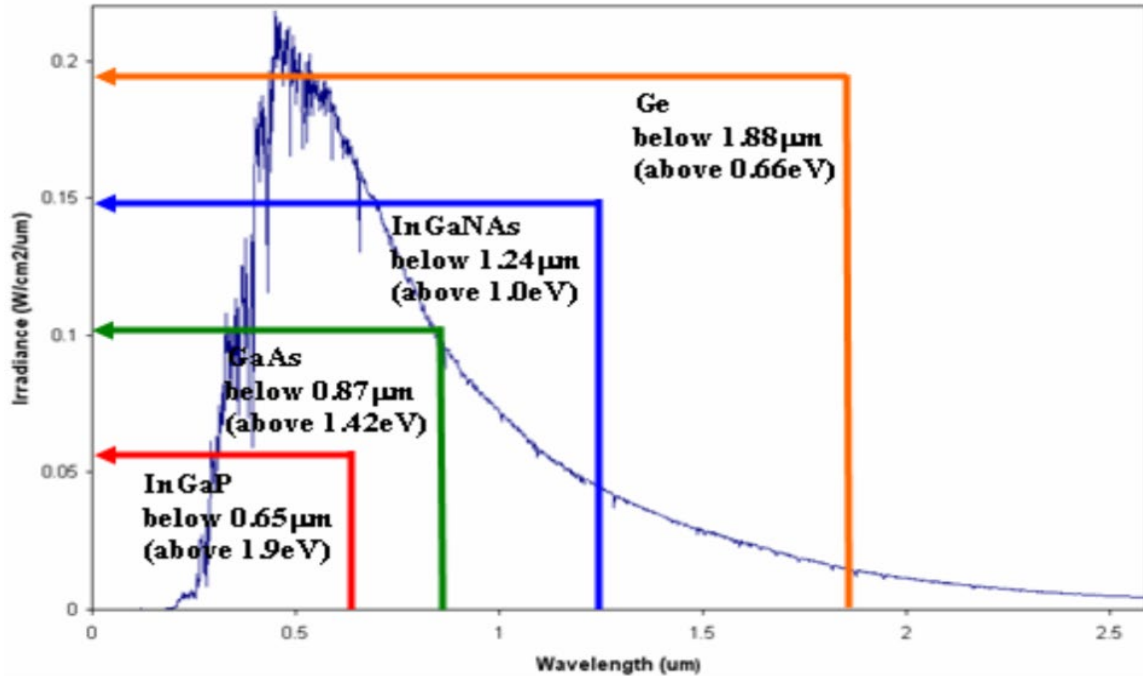
Figure 20.   Energy utilization of different bandgap materials at AM0. Source:
[17].

B.   LOSS MECHANICS

Light reflections, incomplete absorption of light with sufficient energy photons due to limited thickness, recombination, and shadowing are several other losses that exist to reduce PV efficiencies [12]. Reflection of light from the front panel of the cell may result in a 30% loss when the surface is left untreated [14]. To counter this loss, antireflective coatings (ARC) and texturing may be applied to the surface to promote light absorption. The thickness of the ARC to be applied is chosen so that the wavelength in the ARC is one quarter of the incoming light, promoting destructive interference of reflected waves from the ARC and the rest of the cell. To further minimize reflective losses, the material of the ARC is carefully designed to have a refractive index dependent on the materials on either side of it.

Texturing is the process in which pyramid-like shapes are created at the surface of the cell to increase the chance that reflected light bounces back toward the surface vice back into the surrounding air. An example of texturing is shown in Figure 21.

23
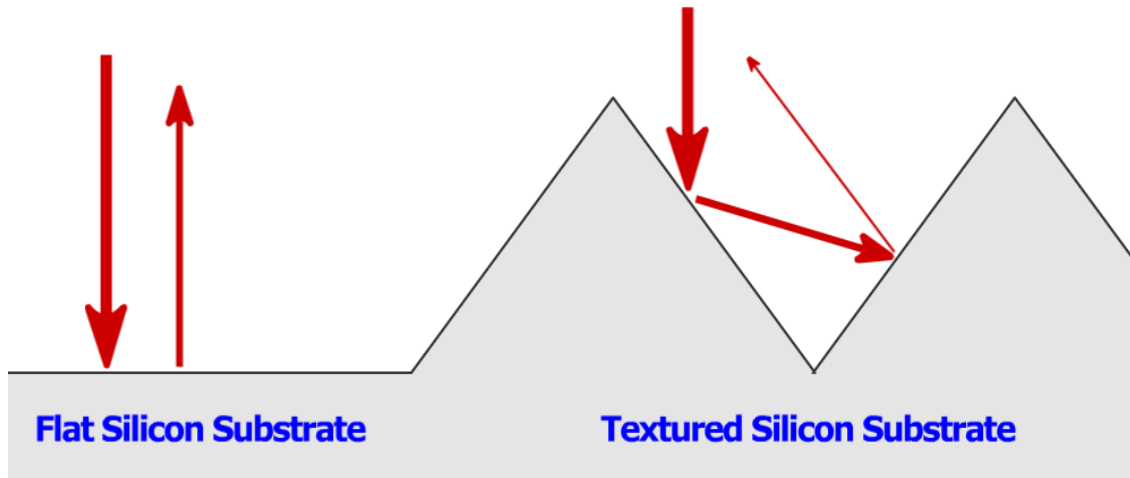
Figure 21.   Surface texturing. Source: [14].

Shadowing loss occurs from the front electrical grid blocking sunlight from interacting with the top of the cell and some of the material beneath it, an approximate loss of 5% efficiency [16]. Careful design of the metallic grid will minimize shadowing loss and ohmic resistance to ensure maximum power can be delivered.

C.   CELL CONSTRUCTION

Now that we understand the solar spectrum, bandgap utilization, and major loss mechanics we can discuss PV cell construction. To ensure even the most modern cells are understood, we will describe the layers used by various cells on the market. Figure 22 will be used to reference the order in which each layer may appear and how the individual layers interact with each other. Note that not all cell designs contain all layers shown and thicknesses will vary greatly based on materials and applications. Additional buffer layers may be required based on materials used. This type of cell is the most common in practice and will be referred to as the conventional cell throughout this thesis. The top electrical grid is shown in gray.
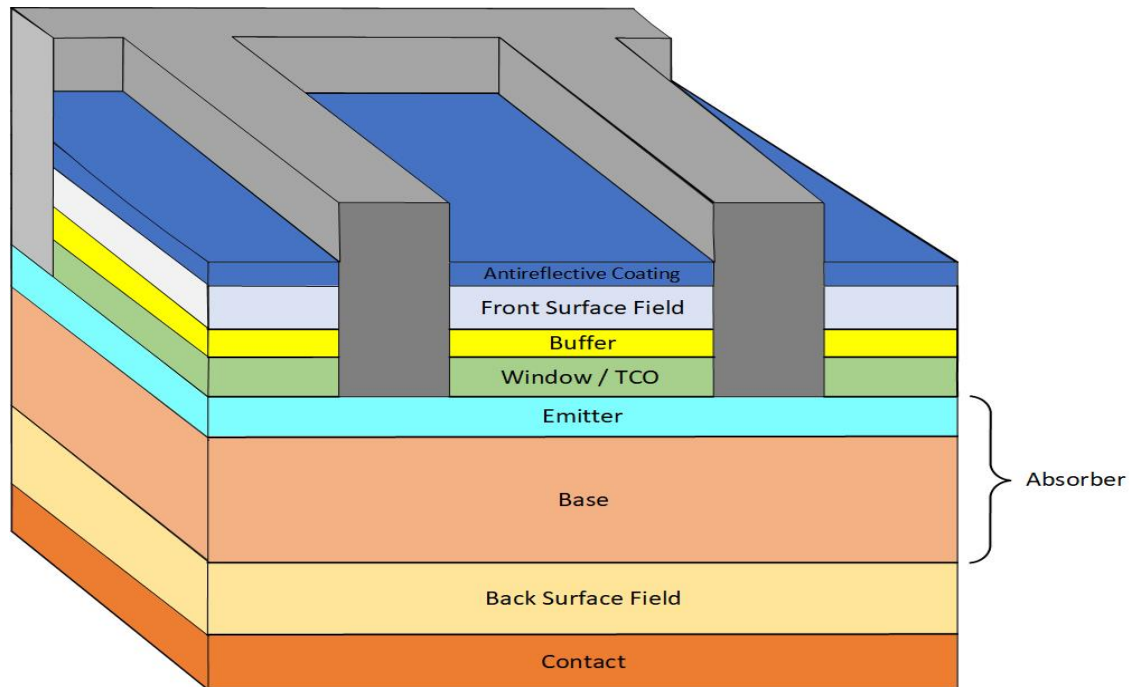
Figure 22.   Layers of typical solar cells.

Grid – Collects charge carriers and provides means of transport for use by external load. Must be carefully designed to minimize shadowing losses (not too big) and maintain low ohmic resistance values (not too small). Large busbars (horizontal grid in Figure 22) toward the center of the cell contain many smaller fingers (vertical grid in Figure 22) extending toward the edges of the cell for collection and transportation of charges.

ARC – Significantly reduces surface reflections to ensure the maximum solar spectrum is utilized for generation. Gives most solar cells, such as polysilicon, their signature blue hue. Double coating may be applied based on intended use.

Front Surface Field (FSF) – Layer of highly resistive material to significantly reduce the amount of surface recombination. In other words, deters carriers from traveling to the surface where they are likely to be lost due to the broken lattice structure at the top of the cell.

Buffer – Reduces internal stresses and number of dangling bonds by lattice matching. Used to connect two materials that would otherwise be incompatible with each other due to their mismatched lattice constants.

25

Window/ Transparent Conducting Oxide (TCO) – Layer of very low resistive material to promote the lateral flow of carriers to maximize collection. In other words, provides a path of lesser resistance than the emitter so that carriers will reach the grid interface before recombining. TCOs are typically used as electrodes because they are low resistance materials that are highly transparent and have large bandgaps to minimize parasitic losses.

Emitter – Top layer of the p-n junction. This will be very thin in comparison to the base, generally only a few microns thick, to reduce distance carriers must travel before being collected at the grid interface. Most EHPs will be generated in this layer or the upper portion of the base. Can be either n-type or p-type based on application but must be opposite polarity as the base.

Base – Bottom layer of the p-n junction, approximately 200-300 microns thick for most applications. Forms p-n junction with emitter and establishes internal voltage to separate light induced EHPs. The combination of the emitter and base is commonly referred to as the absorber. Can be either n-type or p-type based on application but must be opposite polarity as the emitter. P-type base is common due to the high mobility of electrons and therefore lower probability of recombination.

Back Surface Field (BSF) – Provides a small internal voltage to promote separation of charges in areas far from the p-n junction formed by the emitter and base where the field is weak. Made of a highly doped material with the same polarity as the base, its field will accelerate the applicable carriers generated at the bottom of the cell upward while accelerating the opposite polarity carrier in the base downward toward the back contact to help minimize recombination losses.

Back contact – Collects charge carriers. Connected to external load and front grid to make path for current flow. Commonly made highly reflective to give photons of sufficient energy a second pass through the absorber to generate an EHP.

Advanced multijunction cells have more than one absorber to maximize EHP generation. Each absorber is composed of different bandgap materials and stacked with the highest bandgap at the top and lowest bandgap on the bottom. This gives the photons that

pass through an absorber due to spectral mismatch or incomplete absorption a second chance to generate an EHP. Since the layers are stacked in series the internal voltages of the layers will add together, however the total current of the device will be limited to that of the layer with the lowest current. Optimization is extremely important in multijunction devices to ensure current matching to minimize losses. Additional buffer layers or tunnel junctions may be needed to minimize recombination and obtain high efficiency performance.

The higher efficiencies of multijunction devices makes them attractive for applications that require high power outputs or maximum efficiency, such as satellites and other space-based devices. Single junction solar cells remain the most used terrestrially due to the high cost and manufacturing complexity of multijunction cells. Most cells on the market today are made of silicon (Si) due to their relatively high efficiency, low cost and high material abundance. While the advantages of these cells are numerous, they are outside the scope of this thesis and will not be discussed further. An example of a multijunction cell is shown in Figure 23.
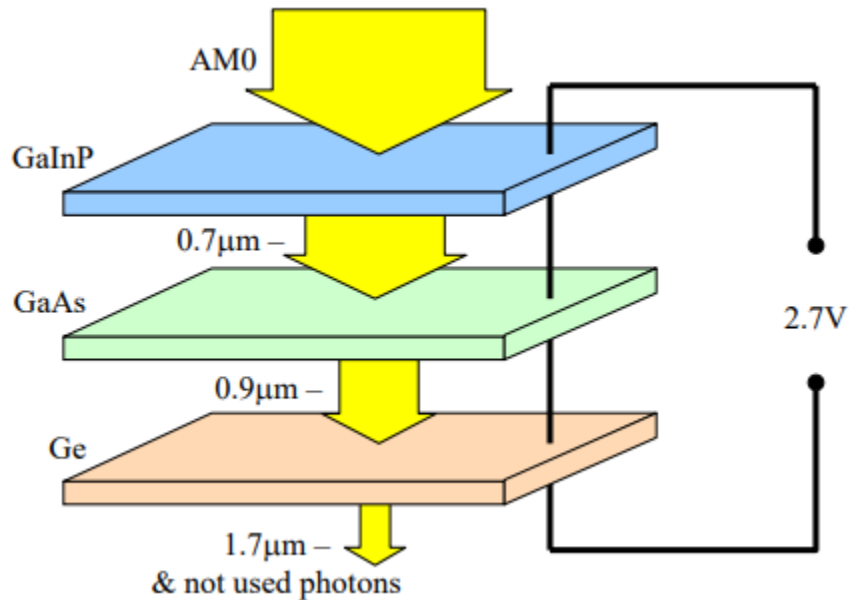
Figure 23.   Multijunction solar cell. Source: [16].

In conventional forward biased p-n junctions, an external source is used to provide excess carriers to promote the flow of charges due to diffusion and the internal voltage. In solar cells, photons with sufficient energy will generate EHP and the carriers will be swept toward their respective side of the junction by the internal voltage. An important note is that current, defined as the flow of positive charges, will move in the opposite direction of a diode current when connected to a load, as shown in Figure 24. Most EHP will be generated in the top portion of the absorber, ideally very close to the p-n junction to reduce the distance carriers must travel to be collected at the grid and minimize losses due to recombination. The addition of the window, FSF and BSF aid in minimizing further recombination losses as previously described. Cell performance will be defined based on the measured current and voltage outputs of the cell, plotted as an I-V curve shown in Figure 25 in Section 3D. Because electrons have a higher mobility than holes the most common cell design is an n-type emitter on top of a p-type base to minimize time for recombination of minority carriers in the base due to the distance they must travel.
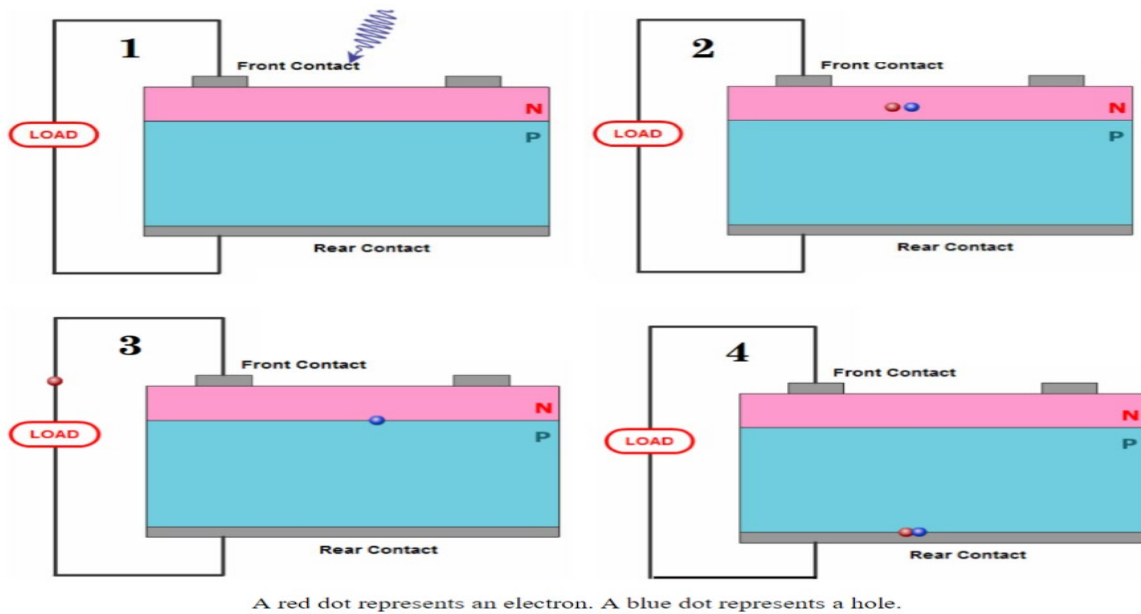
Figure 24.   Basic solar cell mechanics. Source: [2].

# D.	PERFORMANCE METRICS

In addition to the performance metrics shown in Figure 25, known as optical parameters, we also define fill factor (FF) and efficiency (η), calculated by Equations 8-13. FF is a measure of the squareness of the I-V curve; cells that effectively mitigate recombination will obtain a high FF due to their minimal current and voltage losses and therefore have a high efficiency. Because the spectral intensity varies by location on Earth and the AM condition, the input power $P_{spectrum}$ will also vary; therefore, cells can be optimized for specific conditions and applications to achieve a maximum efficiency. An example of just how much $P_{spectrum}$ varies across the globe is shown in Figure 26. By Equation 9, we can see that a material with a lower bandgap will produce a higher I_{sc} than a higher bandgap material due to the higher absorption of incident photons and thus increased generation rate, G. Similarly, we know that a material with a higher bandgap will have a higher internal voltage at the p-n junction. Combining these effects yields in varying I-V curves for different materials, as shown in Figure 27. Curves for compound materials will vary based on the alloy composition.
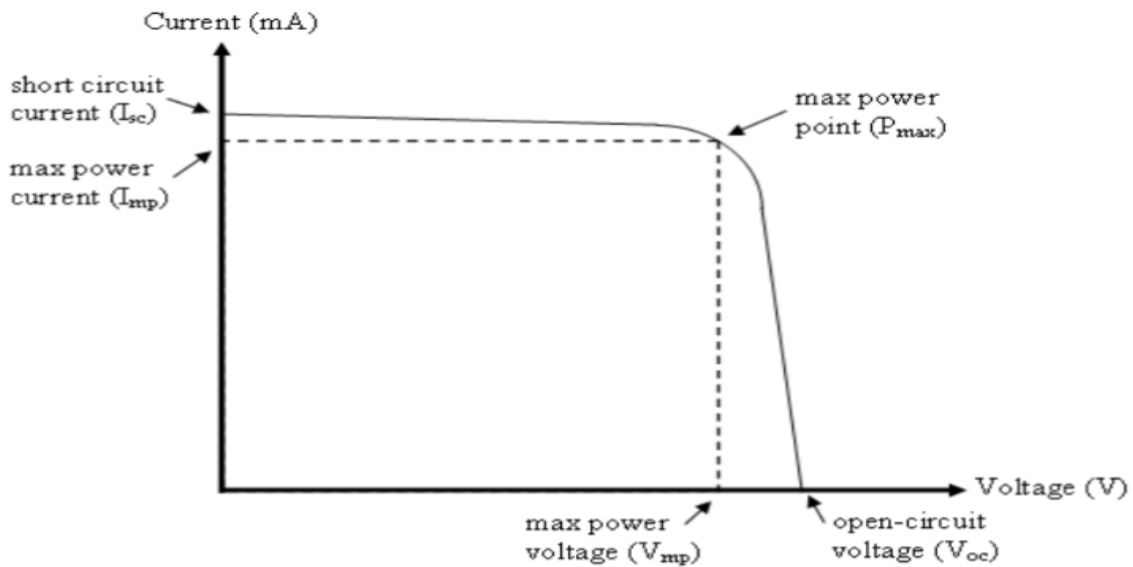
Figure 25.	Generic I-V curve of a solar cell. Source: [17].

$$V_{oc} = \frac{2kT}{e} \ln \left(\frac{G \tau_0}{n_i} \right)$$

(9)

$$I_{sc} = J_{sc} A = qGA(L_n + L_p)$$

(10)

$$P_{max} = I_{max} V_{max}$$

(11)

$$S_{max} = I_{sc} V_{oc}$$

(12)

$$FF = \frac{P_{max}}{S_{max}}$$

(13)

$$\eta = \frac{FF \, S_{max}}{P_{spectrum}}$$

(14)
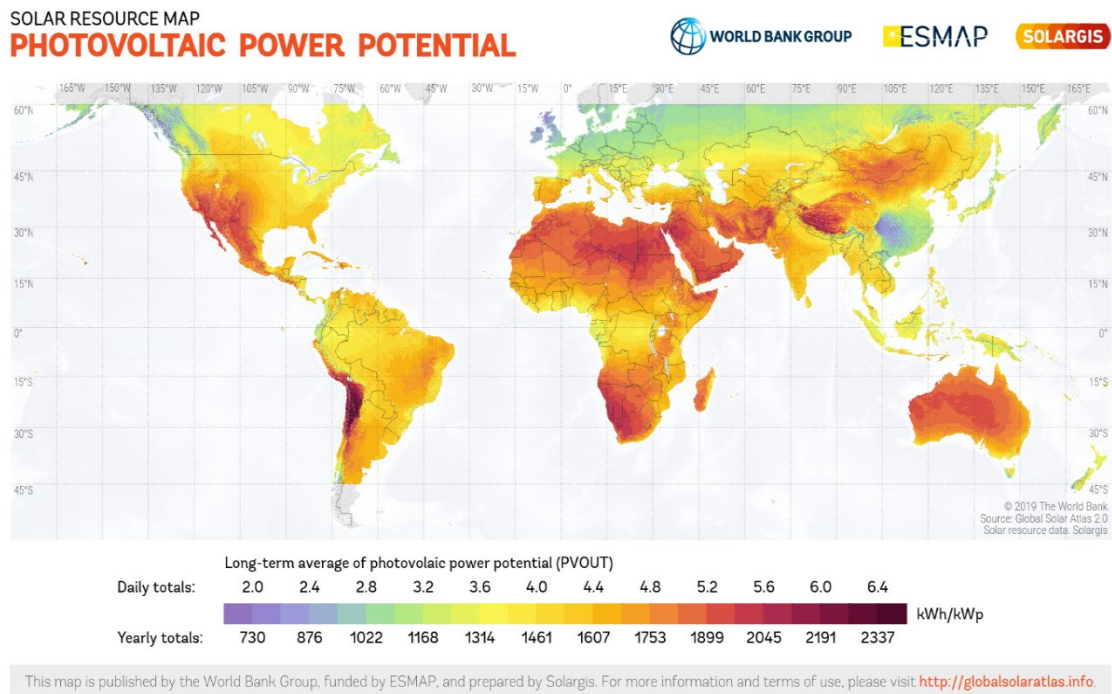
Figure 26.   Global PV power potential (2019 data). Source: [18].
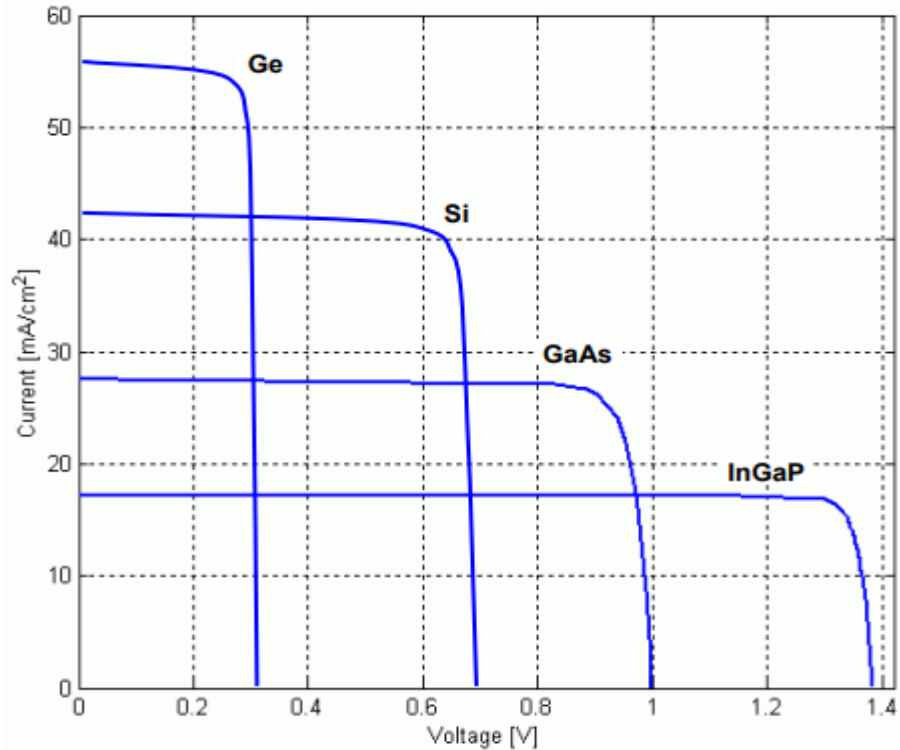
Figure 27.   I-V curve for various materials. Source: [16].

E.   BACK SURFACE CONTACTS

Unlike the wide breadth of materials used to make solar cells, only two methods of cell arrangement currently exist. The first method, conventional, as discussed in Section 3C, requires a front electrical grid and back surface contact to collect and carry charges to the electrical load. The second method, interdigitated back surface contact (IBC), uses a set of alternating p- and n-type materials connected to interdigitated electrical contacts. This method has several other names in industry, namely back surface contact (BSC), staggered back contact (SBC), and back alternating contact (BAC) even though the concept of operations remains the same. For ease of reading, this thesis will use the IBC acronym from this point forward. In this section we explore the fundamental construction and operation of IBC and the advantages/disadvantages it has over conventional cells.

First developed by SunPower Corp. in 2008, Figures 28 demonstrates the basic construction of an IBC cell and its structural orientation. To obtain an understanding of how the cell operates we will breakdown each component in detail.
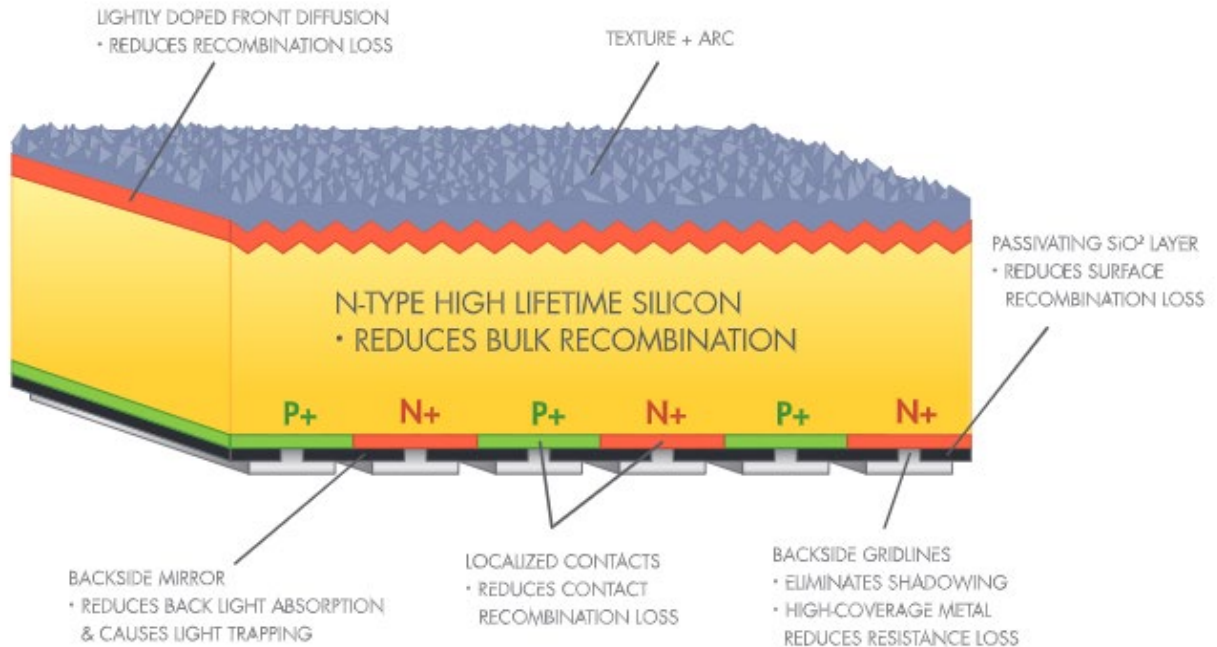
Figure 28.   IBC cell construction. Source: [1].

Surface – Moving the front electrical grid to the back of the device eliminates shadowing losses [19] and therefore generates approximately 10% more EHP due to the increased amount of sunlight captured. This cell also benefits from ease of manufacturing and ability to be textured. ARC is still applied in the same manner.

Passivation – Same functionality as FSF, Buffer, Window/TCO layer of conventional cells discussed above. Lack of lateral current flow through the diffusion layer in an IBC results in lower series resistance under high illumination conditions [19].

Contacts – In conventional cells, careful optimization of finger size was required to maximize collection of carriers while minimizing resistive and shadowing losses. Since the fingers are at the back of the device in an IBC, they can be made much larger thus reducing the series ohmic losses [19]. Heavily doped p- and n-semiconductors (denoted as

p+ and n+) alternate to capture the applicable minority carriers for transport along their respective busbars, shown in Figure 29. Based on the electron and hole mobility constants of the material used, the size of the alternating semiconductors can also be varied to further minimize losses due to recombination. For example, in the experiments run by Lammert and Schwartz [19] the p-type semiconductor was twice the size of the n-type semiconductor. A small gap, approximately 10 μm [19], is placed between each semiconductor to prevent shorting. "Use of p+ and n+ junctions on the unilluminated side can eliminate voltage saturation effects which occur under high illumination conditions without degradation in effective cell lifetime.[19]"
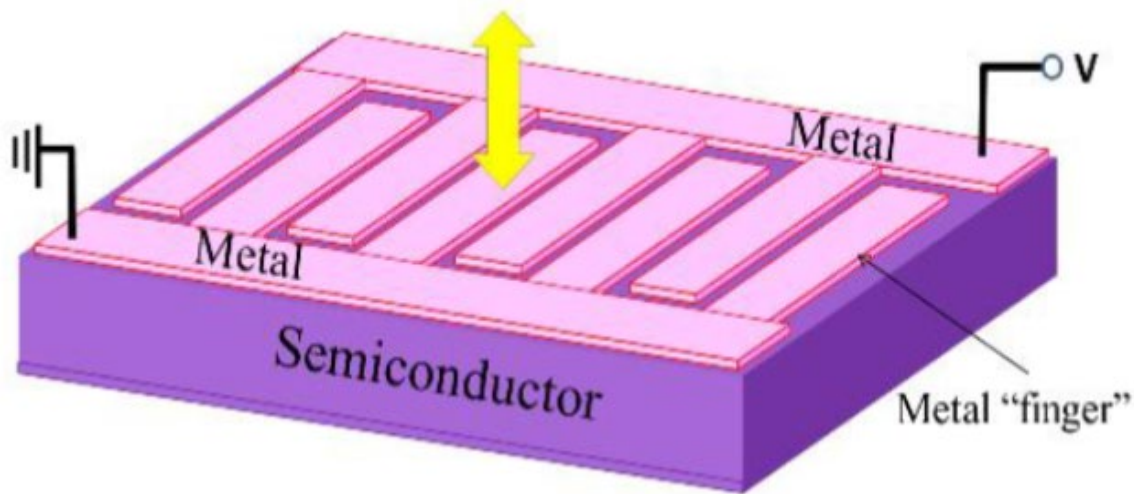
Figure 29.   IBC contact layout. Source: [6].

Bulk – The bulk of the device consists of the absorber, backside mirror and BSF materials. It is responsible for the generation of EHP and acceleration of carriers toward the contacts. In this case however, both electrons and holes must travel downward to be collected. Figure 30 depicts how the carriers will move within the device to arrive at the alternating semiconductors. Note that Figure 30 also demonstrates the difference in size of the alternating semiconductors mentioned previously.
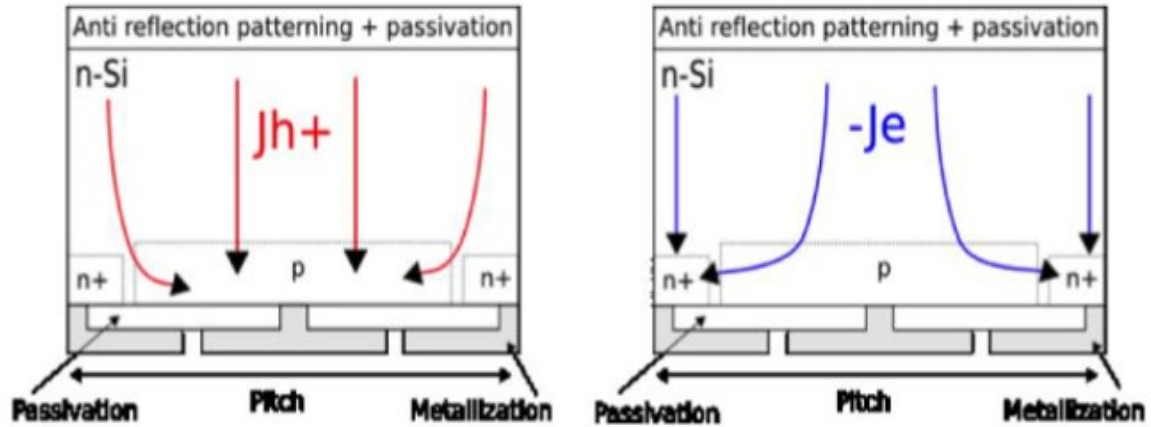
Figure 30.   Movement of minority carriers. Source: [6].

F.   CIGS AND THIN FILM CELLS

Copper indium gallium (di)selenide (CIGS) is a I-III-VI compound semiconductor used in modern photovoltaics. It is composed by alloying copper indium selenide (CIS) and copper gallium selenide (CGS) together to form $CuIn_{(1-x)}Ga_{(x)}Se_2$, where x denotes the mole fraction of Gallium as shown in Equation 14. An x of 0 denotes pure CIS whereas an x of 1 denotes pure CGS. With bandgaps of approximately 1.0 eV and 1.7 eV respectively, the bandgap of CIGS may be tuned as desired by adjusting x [20]. This is particularly useful in optimizing absorber properties to ensure our cells best suit their environment.

$$x = \frac{Ga}{Ga + In}$$

(15)

CIGS is a tetrahedrally bonded semiconductor with a chalcopyrite crystal structure shown in Figure 31. A typical cell arrangement from top to bottom is TCO, buffer, CIGS absorber, back contact, and substrate. While many material combinations exist to construct this cell, the most common materials are aluminum doped zinc oxide (ZnO:Al or AZO), cadmium sulfide (CdS), molybdenum (Mo), and soda lime glass respectively, excluding the absorber. Figure 32 displays an experimental CIGS cell by Richter et al. [21] and its associated ordered layers. An important note is that varying Ga concentration also changes the crystalline grain structure which has been linked to recombination in the absorber layer. Increasing Ga content yields smaller grains and higher defect densities leading to higher

absorber recombination rates, increasing exponentially past x≈.3 [22]. Crystalline morphology for varying Ga content is shown in Figure 33.
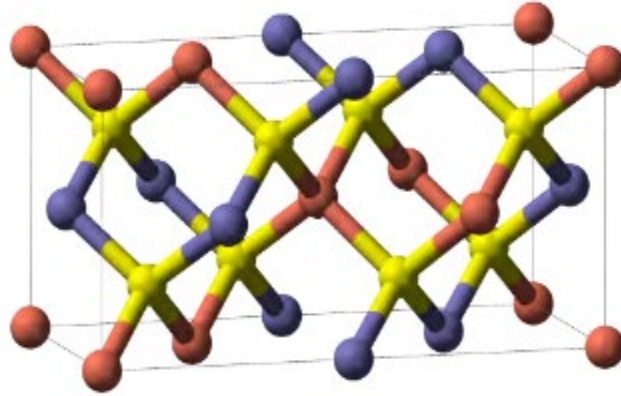
Figure 31.   Crystal structure of CIGS. Copper (red), selenium (yellow), indium or gallium (blue). Source: [12].
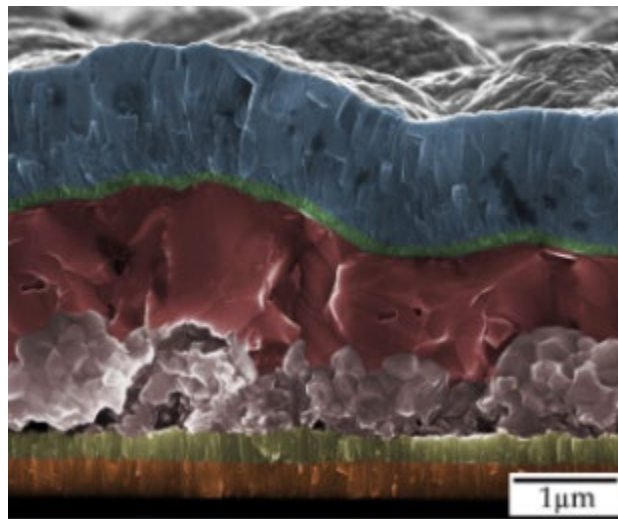
Figure 32.   Experimental CIGS cell. Top to bottom: TCO (blue), buffer (green), absorber (red and pink), back contact (olive), substrate (orange). Source: [21].
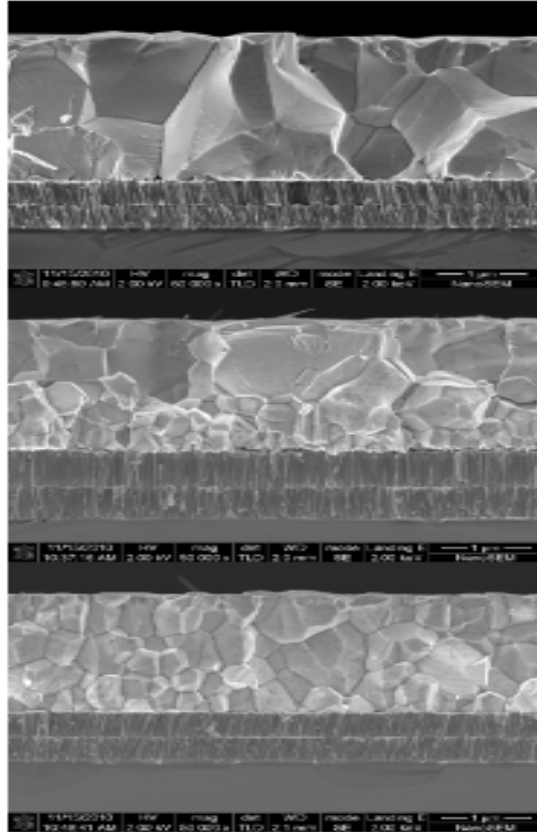
Figure 33.   Changes to CIGS crystal structure with varying x. Top: x=0.4, middle: x=0.5, bottom: x=1.0. Source: [23].

CIGS has several advantages over commonly used photovoltaic materials, such as Si. CIGS has demonstrated excellent long-term stability in outdoors applications, high radiation resistance, non-toxicity (absorber only, as other layers may contain toxic materials) and an estimated four-month payback time [24]. Additionally, its high absorption coefficient (Equation 15) permits the absorber to be much thinner, allowing it to be lightweight and placed on flexible substrates [24]. For this reason, CIGS is one of three thin film solar cells, along with cadmium telluride (CdTe) and amorphous silicon (a-Si). Thin film cells are typically only tens of microns thick and are a promising alternative for space applications. Lastly CIGS is insensitive to defects caused at the junction between CIGS and CdS. This allows highly efficient devices to be made despite CIGS exposure to air prior to junction formation [24], easing manufacturing restrictions and allowing lower-

temperature processes to be used. Figure 34 compares the absorption coefficient, bandgap, and efficiency of CIGS to other thin film cells and several III-V compounds.

$$\alpha = \frac{4\pi k}{\lambda}$$

(16)
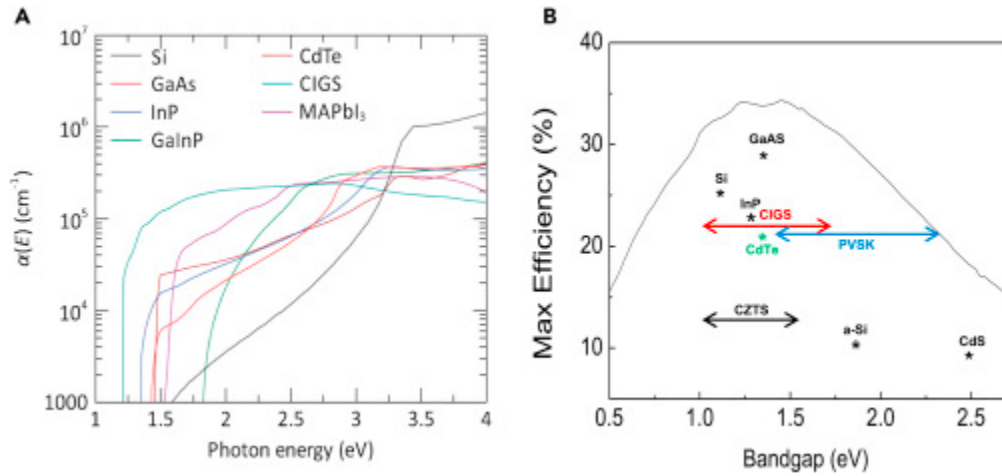
Figure 34.   Absorption coefficients of various materials (a). Bandgaps and efficiencies of various materials (b). Source: [25].

THIS PAGE INTENTIONALLY LEFT BLANK

IV.   MODELING IN SILVACO

This chapter introduces the modeling techniques of the ATLAS device simulator by Silvaco International used in this thesis. We will discuss the importance of modeling, its capabilities, and limitations regarding this thesis. See the Silvaco user manual [26] for proper modeling syntax and available parameters.

ATLAS has the capability to model a wide variety of physical devices and their characteristics. Among these models are solar cells, LEDs, FETs, etc., which can be solved for voltages, currents, doping, electron/hole concentration and many other physical parameters that define such devices. Modeling allows the researcher to predict the behavior of a constructed device without having to build, experiment, and theorize the effects of the many variables composing its makeup. Not only is this more cost beneficial, but also allows the researcher to determine if properties of the device are worth further research or impractical without having to physically build a device. Today, a significant amount of research is done via modeling for these reasons.

ATLAS simulates models based on the configuration of physical dimensions and materials used to define a device. After the simulation is completed, electrical characteristics can be extracted, and figures saved. In order to define a device, users enter data into ATLAS via a plain text interface called Deckbuild. Figure 35 displays the ATLAS input and output path while Figure 36 displays the parameters that must be entered and the order in which they need to occur. We will now break down the individual portions in detail regarding their relation to this thesis.
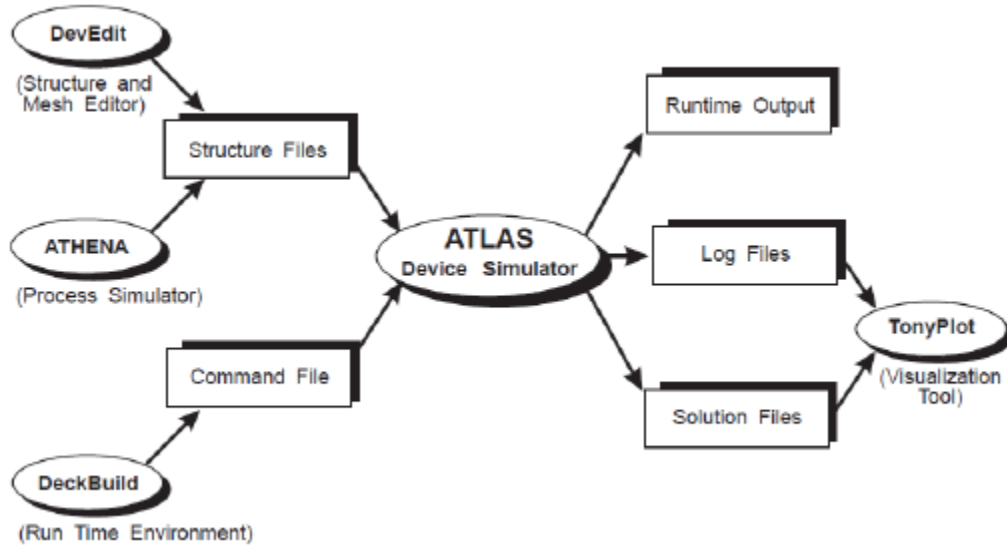
Figure 35.   ATLAS input/output path. Source: [26].

Figure 36.   ATLAS command groups. Source: [26].

1.   Mesh

The mesh is a series of vertical and horizontal lines and the spacing between them to cover the physical simulation domain. Each crossing of vertical and horizontal lines is called a grid point (or node). The finer the mesh, meaning the more grid points present, the higher the resolution the simulation output will be. However, having many nodes requires more simulation time and can be the source of convergence errors within the simulator.

ATLAS will automatically adjust grid sizing based on the spacing commands provided. When creating a mesh, it is important to note that the default length is microns, and the upper left-hand corner is denoted as the origin with positive length on the x-axis to the right and positive depth below. Devices can be modeled in any orientation desired with respect to the origin and accept variables as inputs. Figure 37 shows an example of a mesh with finer spacing defined at the top and center. Example mesh syntax is as follows:

mesh width=

x.mesh   loc=   spac=

y.mesh   loc=   spac=
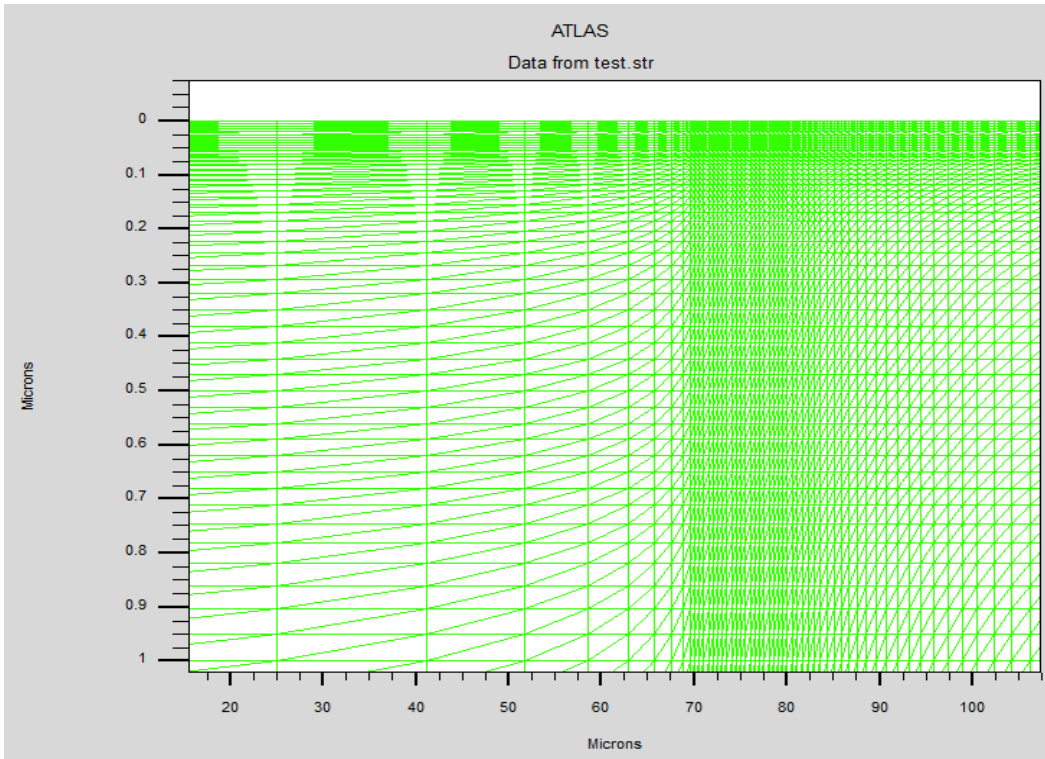
Figure 37.   Example mesh with varying nodal densities.

2.   Region, Material, and Electrode Assignments

After a mesh has been created, regions are then defined over the existing mesh. Regions are used to assign a material to a designated portion of the mesh and must cover the entire 2D

mesh area. Region boundaries must coincide with the mesh grid points defined by the mesh statements. Region numbers are then assigned a material; however specific material properties will be assigned later in the deck. Figure 38 shows a mesh overlaid by the boundaries of defined regions. Figure 39 shows how the material has been assigned to the applicable regions and conductors placed. Example region, material, and conductor assignments are as follows:

region num=1 material=ZnO   x.min=   x.max=
                                    y.min=0   y.max=

region num=10 material=Molybdenum   x.min=   x.max=
                                    y.min=   y.max=   conductor

electrode name=cathode   num=1   x.min=0   x.max=
                                    y.min=   y.max=
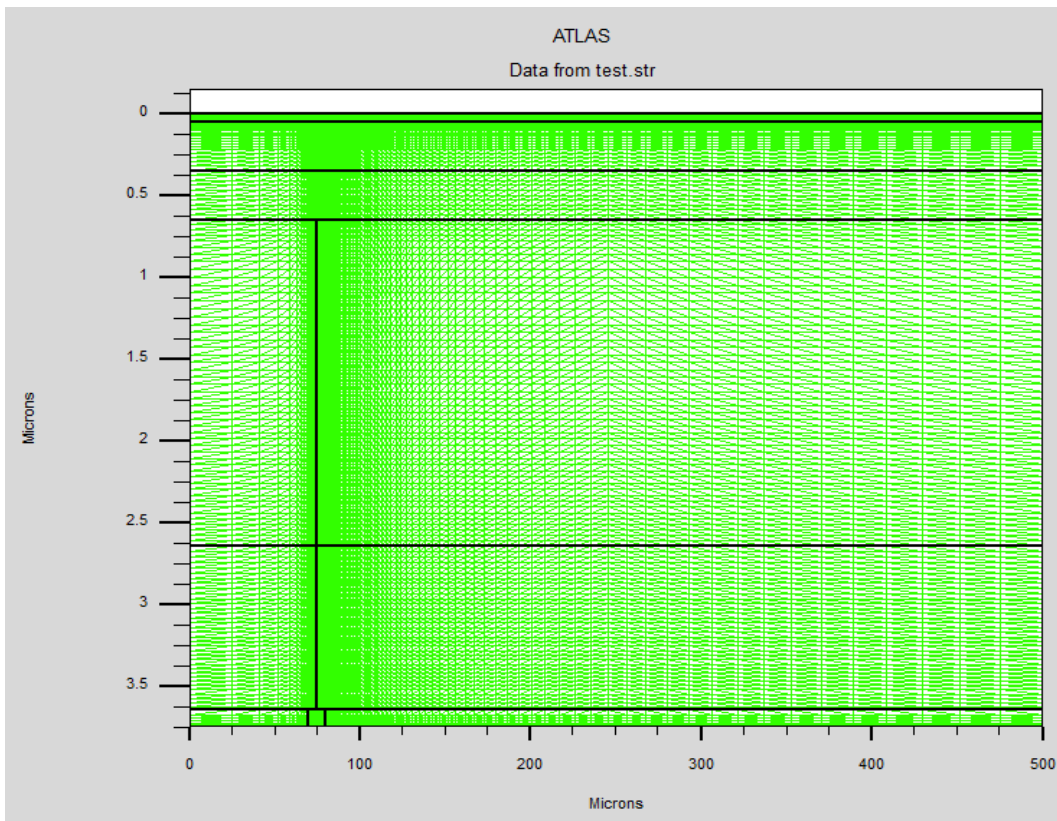
Figure 38.   Example mesh with region overlays.

42
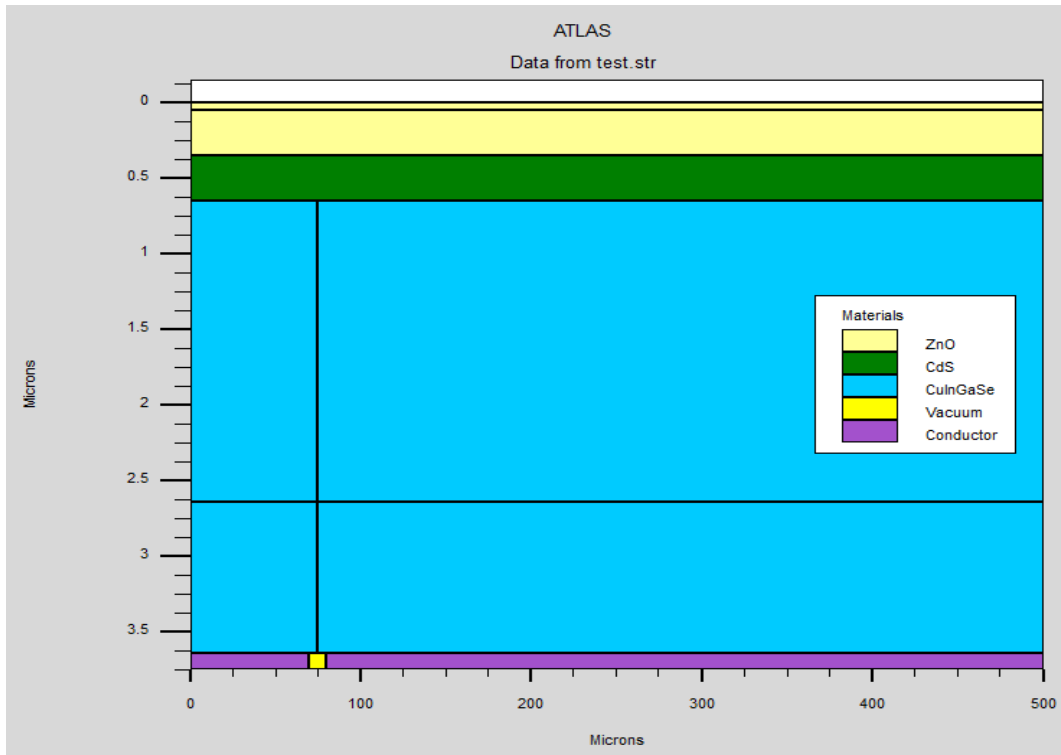
Figure 39.   Example mesh with region, material, and conductor assignments.

3.   Doping and Material Property Definitions

After regions have been assigned to the mesh, doping and material properties can be changed from their default values in the Silvaco library. Doping with specific elements and generic n-type/p-type doping are acceptable. Doping profiles may be uniform, Gaussian, or specified by any C-interpreter text file identifying the spatial distribution of composition fractions or dopants. Regional doping concentrations are also defined in this section.

Silvaco has many materials and their properties pre-loaded, however they can be changed or supplemented by user defined values. Examples of electrical property changes used during this thesis are hole/electron mobility, bandgap, electron affinity, dielectric constant, and complex refractive index. Property changes can be specific to a region or applied to a material regardless of region. Like doping, user defined values may be plain text within the Silvaco command window or read from C-interpreter files. Example doping and material adjustments are as follows:

doping AL	uniform	conc=	region=
doping n.type	Gaussian	conc=	region=
material region=2	EG300=	AFFINITY=	EPSILON=
	NC300=	NV300=	MUN=	MUP=
	index.file='name.txt'		

material material=Vacuum   real.index=   imag.index=

4.   Traps and Interfaces

Manufacturing processes of semiconductors are not perfect, leaving behind crystalline flaws and dangling bonds at interfaces or the presence of an impurity. These defect sites, or traps, may lie in the forbidden zone and exchange charges with the conduction and valence bands. Such actions may significantly influence the electrical characteristics of a device and are therefore worth modeling in cases where a non-ideal performance is desired to be simulated. Traps can be modeled at specific energy levels, densities, recombination velocities, and capture cross sections.

Interface commands describe the interaction between adjacent materials (material interface) or a material interaction with applied optical waveforms (optical interfaces). Material interfaces determine the recombination velocities (s.n, s.p) and can be specified as semiconductor to insulator (s.x), semiconductor to semiconductor (s.s), or semiconductor to metal (s.m). Optical interfaces can be used to apply anti-reflective coatings, specify refractive indices, or determine amount of reflection. Examples of trap and interface commands are as follows:

trap material=ZnO donor	e.level=	sign=	sigp=
	density=	degen.fac=	x.min=
	x.max=	y.min=	y.max=
interface x.min=	x.max=	y.min=	y.max=
s.n=	s.p=	s.x (or s.s, s.m)	

interface	optical	ar.index=	reflect=	x.min=0
	x.max=	y.min=	y.max=	coating=

5. Models, Methods, Output, and Outfiles

Many models exist within the Silvaco library in order to simulate a vast number of electrical device phenomena, as shown in Section 1.2.1 of [26]. Model commands "specifies model flags to indicate the inclusion of various physical mechanisms, models, and other parameters.[26]" Method commands "set the numerical methods to be used to solve the equations and parameters associated with these algorithms.[26]" Maximum iteration limits before program timeout can also be specified under methods commands. Output commands "allow you to specify the data that will be stored in standard structure format files.[26]" Numerous outputs may be defined, however several ones relevant to this thesis define the photogeneration rate, mobilities, traps, and current flowlines.

Various types of outfiles exist and are relevant under varying conditions. Outfiles significant to this thesis are structure files ".str" and log files ".log". Structure files contain information regarding parameters specified by output commands. For example, structure files were used with TonyPlot, the Silvaco plotting software, to create Figures 38 and 39. Log files "contain only the terminal characteristics [26]" and are used with TonyPlot to view model behavior, such as an I-V curve. All files can be saved and recalled as desired provided the simulation metadata is still present. Examples of all command type are as follows:

models	srh	fermi	optr	auger	temp=
method	gummel	newton	itlimit=		
output	photogen	recomb	traps	flowlines	

THIS PAGE INTENTIONALLY LEFT BLANK

V. RESEARCH AND RESULTS

A. RESEARCH

While still relatively new in the world of photovoltaics, published IBC cell designs have been limited. SunPower explored IBC using polysilicon, promoting O'Connor [2] to explore the use of GaAs with an IBC design. The motivation for this thesis is to combine the discussed advantages of both CIGS and IBC into a single cell to determine its optical parameters under AM1.5 conditions via simulation in Silvaco. To accomplish this, we will first simulate a conventional CIGS IBC design architecture shown in Figure 40. Upon verification that our model works and obtaining baseline optical parameters we will explore a novel design, shown in Figure 41, in which a vertical p-n junction is created to further promote the separation of charges in the absorber to minimize recombination losses. This design was first investigated by Herrera [3] in 2017, however additional variations, such as region sizing, are taken into consideration in this thesis.
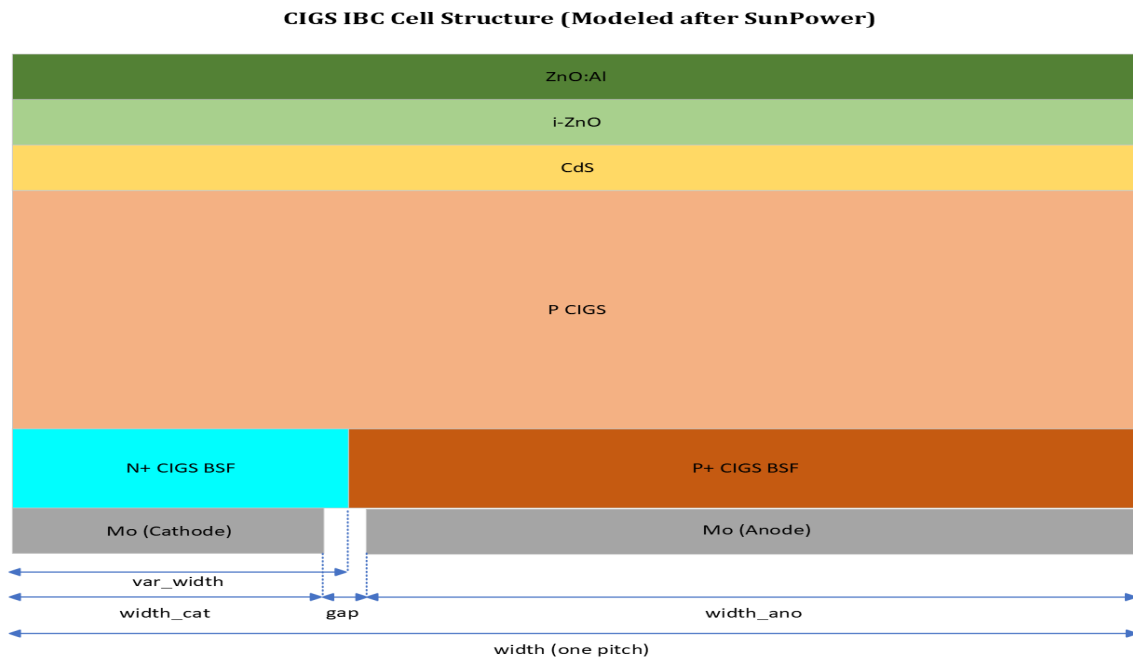
Figure 40. First CIGS cell, modeled after SunPower.

Experimental CIGS IBC Cell Structure
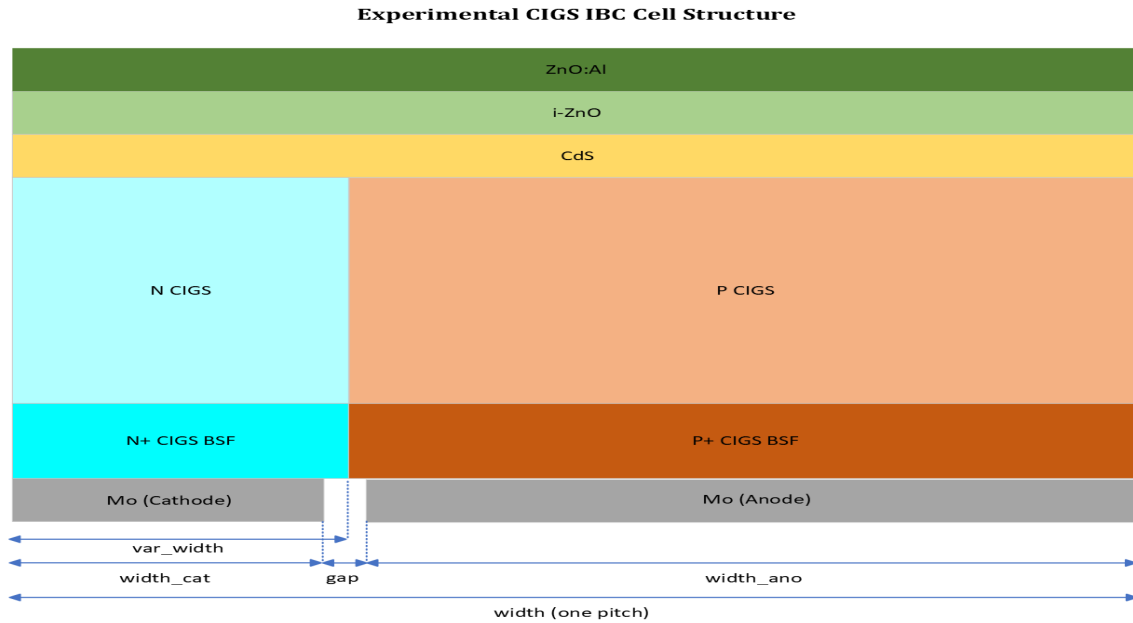
Figure 41.   Second CIGS cell, novel design.

Our passivation layer consists of an AZO TCO and CdS buffer with highly resistive intrinsic ZnO (i-ZnO) in between to reduce shunt paths [27]. The n-type CdS forms the heterojunction with the p-CIGS and protects it during ZnO/AZO deposition [27]. Highly doped n-type and p-type CIGS (n+ CIGS and p+ CIGS, respectively) attract carriers toward the contacts at the bottom of the cell. In our experimental cell, an additional n-CIGS section is added to establish a vertical electric field to separate charge carrier in the absorber and prevent recombination. In either cell design, we can vary the width of the BSF or BSF/CIGS combination to accommodate for the differences in hole and electron mobilities to obtain the most efficient cell. Both cells consist of one 500 μm pitch and can be repeated to produce a full-sized cell.

While not shown in Figures 40 and 41, a 0.10 μm MgF$_2$ ARC is simulated in Silvaco to obtain the most realistic response possible. MgF$_2$ was chosen based on Equation 16, where n_1 is the optimal refractive index of the ARC and n_o and n_2 are the refractive indices of the materials bordering the ARC, air and AZO in this case. The refractive indices of air, AZO, and MgF$_2$ are 1.0, 2.0, and 1.413 respectively, a perfect match. With the highest energy light concentrates around the 0.6 μm range, an optimal thickness of 0.10

μm is obtained based on optimal transmittance at one quarter wavelength [14]. In all cases, a gap of 10 μm was used to prevent contact shorting.

$$n_1 = \sqrt{n_0 n_2}$$

(17)

Compared to other PV materials, the properties of CIGS and its optimal parameters are much less extensively published. Adding complexity, all values vary based on the mole fraction of Ga used; thus, a large set of values may exist. Several former NPS students quote their properties used, however an extensive independent study was conducted to verify the validity of their research. Table 3 summarizes the optimal parameters discussed in journal articles while Table 4 summarizes the parameters that will be used as a starting point for research in this thesis. Table 4 contains values that were either identical across all articles or the most recurring and were found of comparable magnitude to those cited by Herrera [3].

Table 3.　Journal cited optimal parameters. Adapted from [3],[22]-[24],[27]-[34].

	Thickness	Doping	Bandgap [eV]	Ga Mole Fraction, x
CIGS	1.6-2.1 μm [28][30][33][34]	Not cited	1.16-1.4 (dir) [23][29][30][32][34]	0.2-0.31 [24][29][22][31]
ZnO	50 nm [3][24][28]	Not cited	3.3 (fixed, dir)	N/A
CdS	50 nm [3][27][30][34]	1e17 [27]	2.42 (fixed, dir)	N/A

Table 4.   Starting research parameters. Adapted from [4],[20],[27]-[31],[34]-[40].

	ZnO:Al (AZO)	i-ZnO	CdS	CIGS (X=.3)
Thickness [μm]	0.05	0.05	0.05	2 1 (BSF)
E_g [eV]	3.3	3.3	2.48	1.20 [31]
χ_e [eV]	4.5	4.5	4.18	4.26 [38]
ε_r [cm^{-3}]	9	9	10	13.6
N_c [cm^{-3}]	2.2e18	2.2e18	2.2e18	2.2e18
N_v [cm^{-3}]	1.8e19	1.8e19	1.8e19	1.8e19
μ_n [cm^2/Vs]	100	100	100	100
μ_p [cm^2/Vs]	25	25	25	25
Doping [cm^{-3}]	1e20	1e18	1e17	8e16 4e18 (BSF)
Type	N	N	N	P
σ_e [cm^2]	1e-14	1e-15	1e-15	4e-16
σ_h [cm^2]	3e-13	1e-15	1e-12	4e-14
N_t [cm^{-3}]	3e16	1e16	1e16	7.5e13
E_t [eV]	0	0	0	0
S_e [cm/s]	1e5	1e5	1e5	1e5
S_h [cm/s]	1e5	1e5	1e5	1e5

During research, it was noted that different CIGS bandgap equations exist [20],[24],[31] with only minor deviations in their outputs. Given that this thesis utilizes Silvaco software the bandgap equation quoted by Larez et al. [31] will be used, displayed by Equation 17. A discrepancy between the values calculated by Larez et al. [31] and the ATLAS user manual [26] was discovered and verified by Silvaco engineers (corrected by Silvaco for newer version); therefore, the calculation from [31] was manually entered during simulation to ensure model accuracy. Table 5 displays the calculated CIGS bandgap from Equation 17 for various mole fractions of interest at T=300 K whereas Figure 42 plots the resulting bandgap over a wide range of mole fraction and absolute temperature. Both Table 5 and Figure 42 demonstrate that a mole fraction of 0.3 will yield a bandgap within the optimal band of Table 3 and will thus be used as a starting point for this thesis research.

$$Eg_{CIGS}(x,T) = \{1.036 + 225(4.238*10^{-5}) - 170(8.75*10^{-5})[\coth(\frac{170}{2T}) - 1]\}(1-x)$$

$$+\{1.691 + 259(8.82*10^{-5}) - 189(16*10^{-5})[\coth(\frac{189}{2T}) - 1]\}x - .02x(1-x)$$

$$(18)$$

Table 5.   CIGS bandgap, calculated by Equation 17 at T=300 K.

x		0.2	0.22	0.24	0.26	0.28	0.30	0.32	0.34
Eg [eV]		1.137	1.150	1.163	1.176	1.189	1.202	1.215	1.228
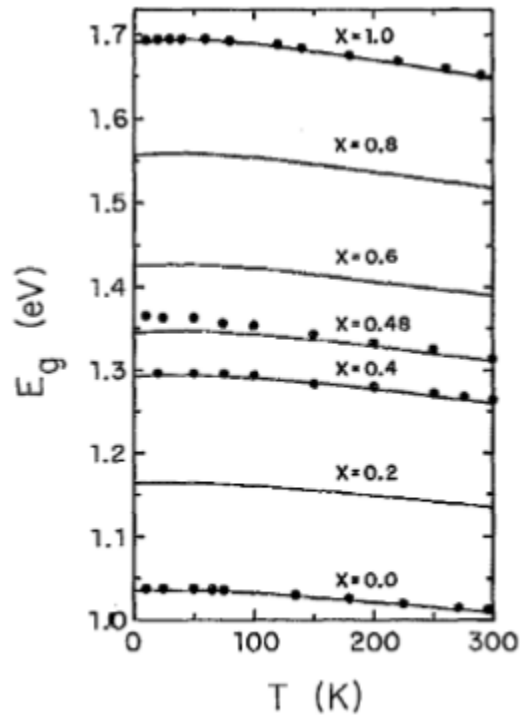
Figure 42.   CIGS bandgap equation for varying mole fraction and temperature.
Source: [31].

B.   RESULTS

First step in our research was to develop working models of both the Sunpower and experimental design architectures in Silvaco. To do so, the modeling techniques of Chapter IV and parameters in Table 4 were applied to develop a complete cell. Region assignments,

51

doping concentrations, material properties, trap concentrations, material interfaces, optical interfaces, models, methods, and outputs were all assigned in this phase. Refer to Appendices A and B for the coding of both cell designs and Figures 43 and 44 for their structure under Table 4 parameter specifications.
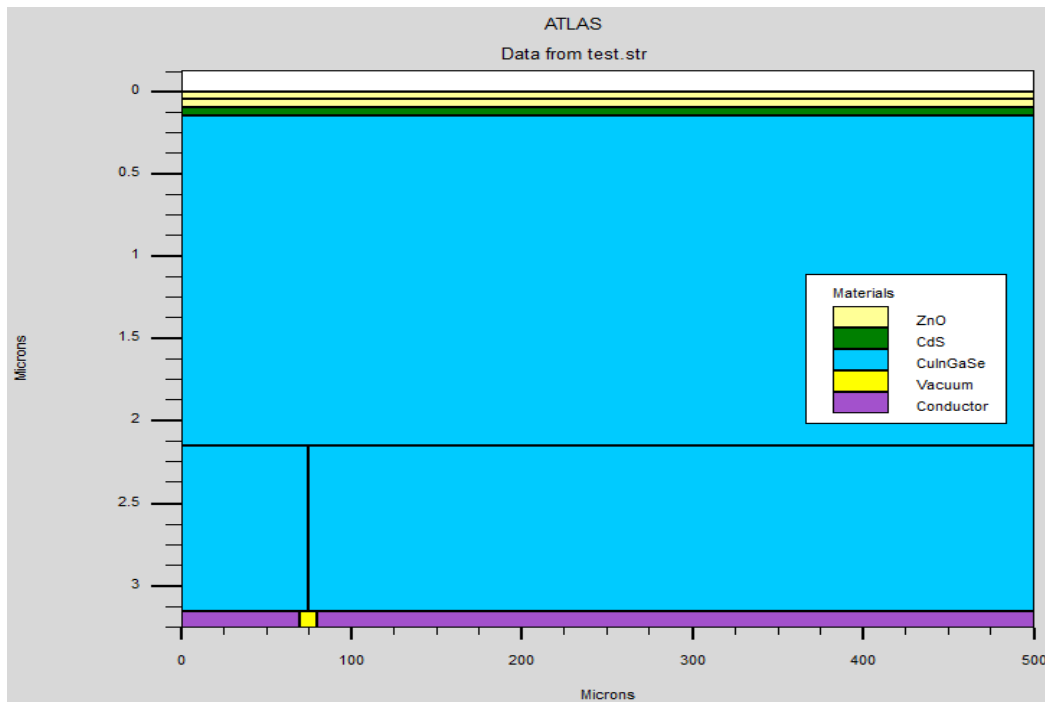
Figure 43.   SunPower model produced in Silvaco.
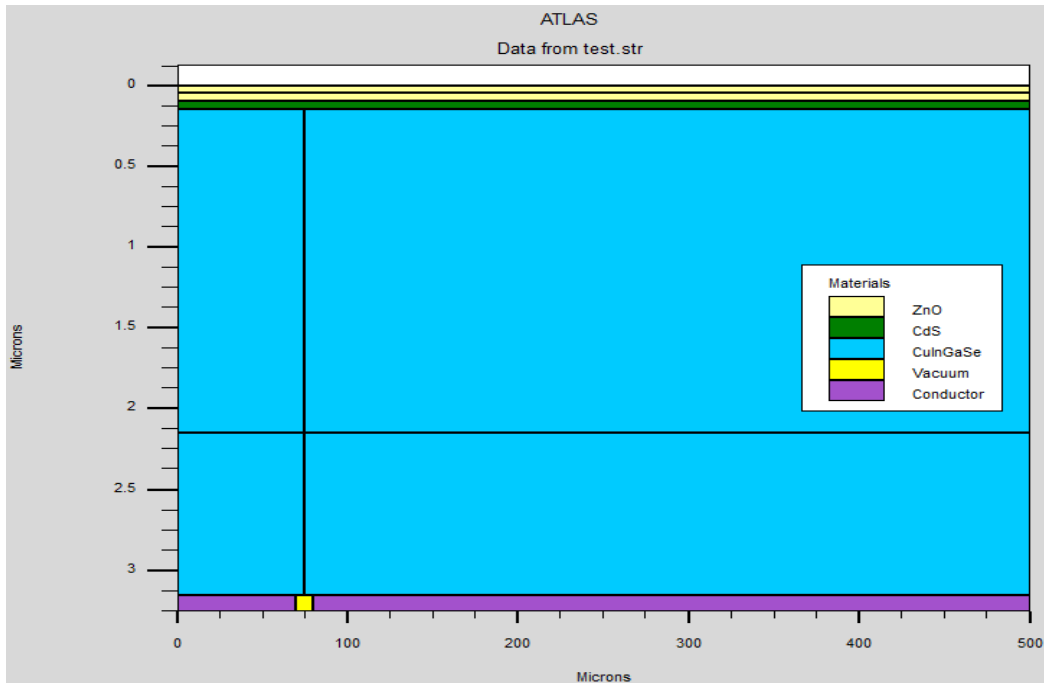
Figure 44.   Experimental model produced in Silvaco.

To find the optimal performance characteristics of our cells, an iterative trial and error approach was taken. First, our researched based optimal values were simulated to obtain baseline optical parameters and compared to the results of the optimal values obtained by Herrera [3]. Next, each layer was varied independently of each other in six different layer thicknesses to determine/verify its effect on the overall cell. When each layer was varied, the other layers were kept at the research-based optimal values defined in Table 4. Six thicknesses, from 0.05-0.30 μm, were chosen for the passivation layers to provide an adequate sample size for trend analysis of individual layer effects and total cell composition. To minimize the number of variable changes, all doping concentrations remained constant per Table 4 during all trials. Ga mole fraction remained at .3 and var_width remained at 15% of the cell width until the optimal cell was found. Further experimentation with these parameters occurred on the passivation layer thickness optimized cell only. Table 6 shows the baseline test results of both cell configurations under defined optimal conditions from Herrera [3] and Table 4.

Table 6. Baseline test results of defined optimal cell parameters.

	SunPower Model		Experimental Model	
	Herrera	Research	Herrera	Research
AZO [μm]	0.4	0.05	0.4	0.05
ZnO [μm]	0.4	0.05	0.4	0.05
CdS [μm]	0.45	0.05	0.45	0.05
CIGS [μm]	11	2	11	2
CIGS+ [μm]	6	1	6	1
Mo [μm]	0.4	0.1	0.4	0.1
Var width	0.15	0.15	0.15	0.15
Ga x	0.3	0.3	0.3	0.3
I_{SC} [mA]	2.67	11.84	32.39	34.61
V_{OC} [V]	0.769	0.816	0.792	0.817
P_M [mW]	1.75	7.96	20.80	11.84
V_M [V]	0.680	0.710	0.670	0.540
I_M [mA]	2.57	8.23	21.04	21.93
FF	0.851	0.824	0.811	0.419
Eff [%]	1.75	7.96	20.79	11.83

After approximately 50 trial and error simulations, the following conclusions were obtained regarding the SunPower cell design. The most efficient cell parameters are listed in Table 7. While outside the scope of layer variations chosen for this thesis, the optimal passivation layer thicknesses defined by Herrera [3] were applied to several trials based on the observations listed. These results championed all other trials and were therefore included in our observation of the most efficient cell. Figure 45 shows cell construction in Silvaco under Table 7 conditions.

1. Increasing CIGS absorber layer thickness from 2.0-4.0 μm reduced I_{SC} from 10.73 mA to 7.50 mA. V_{OC} remained at 0.800 V. Cell efficiency dropped from 7.14% to 5.03%.

2. Reducing CIGS absorber layer thickness from 2.5-1.0 μm raised I_{SC} from 10.90 mA to 15.77 mA. V_{OC} raised from 0.814 V to 0.833 V. Cell efficiency raised from 7.36% to 10.47%.

3. Increasing BSF layer thickness from 0.75-2.0 μm raised I_{SC} from 11.66 mA to 12.14 mA. V_{OC} remained at 0.817 V. Cell efficiency raised from 7.96% to 8.18%.

4. No performance difference with Mo contact thickness changes. All optical parameters remained the same.

5. Increasing AZO layer thickness from 0.10-0.30 μm raised I_{SC} from 12.28 mA to 13.69 mA. V_{OC} remained constant at 0.816 V. Cell efficiency raised from 8.24% to 9.20%.

6. Increasing ZnO layer thickness from 0.10-0.30 μm raised I_{SC} from 14.10 mA to 17.90 mA. V_{OC} remained constant at 0.814 V. Cell efficiency raised from 9.47% to 12.01%.

7. Increasing CdS layer thickness 0.10-0.30 μm raised I_{SC} from 11.72 mA to 13.25 mA. V_{OC} remained constant at 0.815 V. Cell efficiency raised from 7.85% to 8.92%.

Table 7.   SunPower cell design trials optimal parameters.

	SunPower
AZO [μm]	0.4
ZnO [μm]	0.4
CdS [μm]	0.45
CIGS [μm]	1
CIGS+ [μm]	0.75
Mo [μm]	0.1
Var_width	0.15
Ga x	0.3
I_{SC} [mA]	29.1
V_{OC} [V]	0.822
P_M [mW]	19.45
V_M [V]	0.710
I_M [mA]	27.39
FF	0.812
Eff [%]	19.44
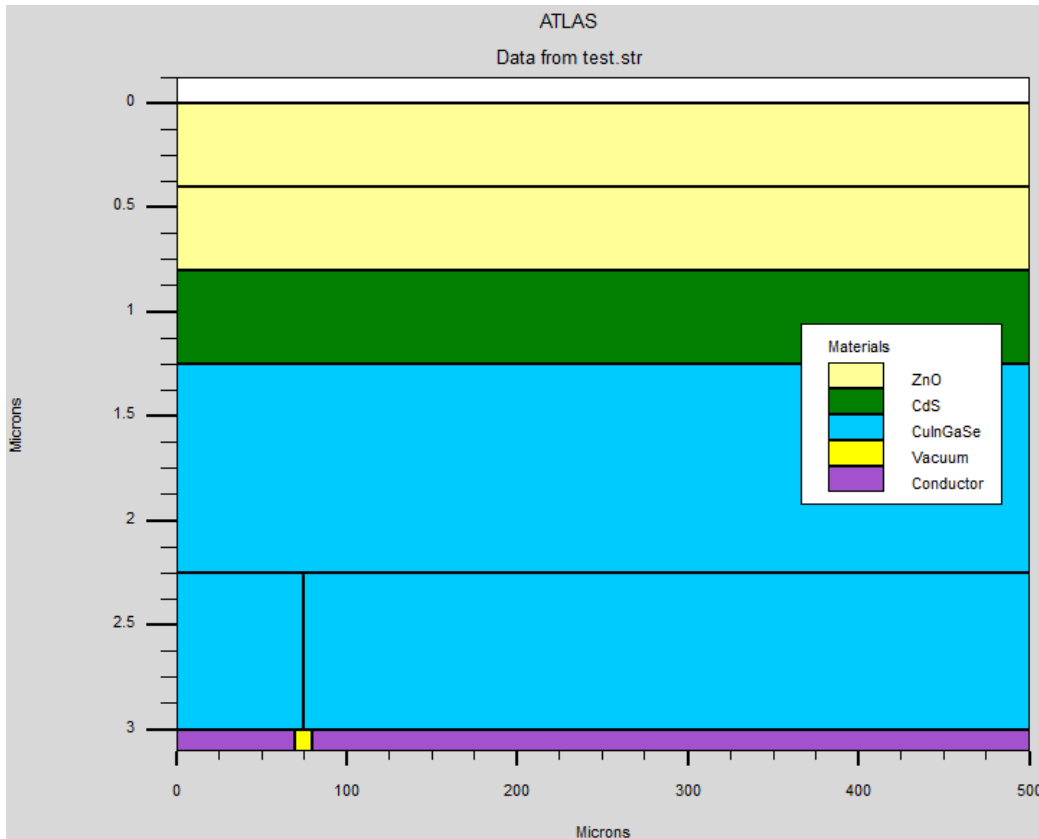
Figure 45. Silvaco design of SunPower cell in Table 7.

While these initial trial results seem promising, several points must be addressed. First, the improvements in I_{SC} with changing CIGS/BSF layer thickness are likely due to the proportionally larger, higher doped BSF rather than the characteristics of the absorber as we expect I_{SC} to improve as the CIGS layer is increased. Second, the I_{SC} gains by increasing the passivation layers dominate those of the absorber layers. While the cell described by Table 7 is highly efficient, its passivation layer is very thick when compared to the typical proportions of a solar cell.

After approximately 30 trial and error simulations, the following conclusions were obtained regarding the experimental cell design. The most efficient cell parameters are listed in Table 8 and Silvaco construction shown in Figure 49. Due to the experimental nature of this cell, strict adhesion to the layer thickness restrictions were observed.

1. No significant difference in performance with changing BSF thickness until less than 1μm. This confirms the observations found by Herrera [3]. Below 1μm V_{OC} began to suffer sharply. Reducing BSF thickness from 1.50-1.0 μm lowered V_{OC} from 0.819 V to 0.817 V while further lowering from 1.0-0.25 μm lowered V_{OC} from 0.817 V to 0.804 V. From a thickness of 1.5-0.25 μm, I_{SC} lowered form 34.65 mA to 34.36 mA. Cell efficiency dropped from 11.90% at 1.5 μm to 11.48% at 0.25 μm.

2. No performance difference with Mo contact thickness changes. This confirms the observations found by Herrera [12] for this cell design. All optical parameters remained the same.

3. Increasing CIGS absorber layer thickness from 2.0-6.0 μm lowered I_{SC} from 34.61 mA to 34.33 mA. V_{OC} lowered from 0.817 V to 0.799 V. Cell efficiency dropped from 11.83% to 11.41%

4. Increasing AZO layer thickness from 0.05-0.30 μm lowered I_{SC} from 34.61 mA to 34.12 mA. V_{OC} remained constant at 0.817 V. I-V curve knee extended from 0.100 V to ~0.325 V as thickness increased from 0.10-0.30μm. P_M increased from 11.84 mW to 14.32 mW. I_M increased from 21.93 mA to 26.52 mA. V_M remained constant at 0.540 V. FF raised from 0.419 to 0.514. Cell efficiency increased from 11.83% to 14.32%. See Figure 46.

5. Increasing ZnO layer thickness from 0.05-0.30 μm lowered I_{SC} from 34.61 mA to 33.57 mA. V_{OC} lowered from 0.817 V to 0.814 V. I-V curve knee extended from 0.450 V to ~0.650 V as thickness increased from 0.10-0.30μm. P_M increased from 11.84 mW to 21.19 mW. I_M increased from 21.93 mA to 31.62 mA. V_M increased from 0.540 V to 0.670 V. FF raised from 0.419 to 0.775. Cell efficiency increased from 11.83% to 21.18 %. See Figure 47.

6. Increasing CdS layer thickness 0.05-0.30 μm raised I_{SC} from 34.61 mA to 34.69 mA. V_{OC} remained constant at 0.817 V. I-V curve knee extended

from 0.100 V to ~0.350 V as thickness increased from 0.10-0.30µm. P_M increased from 11.84 mW to 14.96 mW. I_M increased from 21.93 mA to 27.70 mA. V_M remained constant at 0.540 V. FF raised from 0.419 to 0.529. Cell efficiency increased from 11.83 % to 14.95 %. See Figure 48.

To distinguish between the common effects of increased AZO and CdS layer thicknesses, additional trials were run where ZnO thickness was kept constant and only AZO or CdS was varied. At the conclusion of these trials, it was found that increasing CdS had a slightly more significant effect in extending the knee of the I-V curve and led to greater positive changes in PM, IM and FF. These additional trials were included in this trial set and are reflected in Table 8.
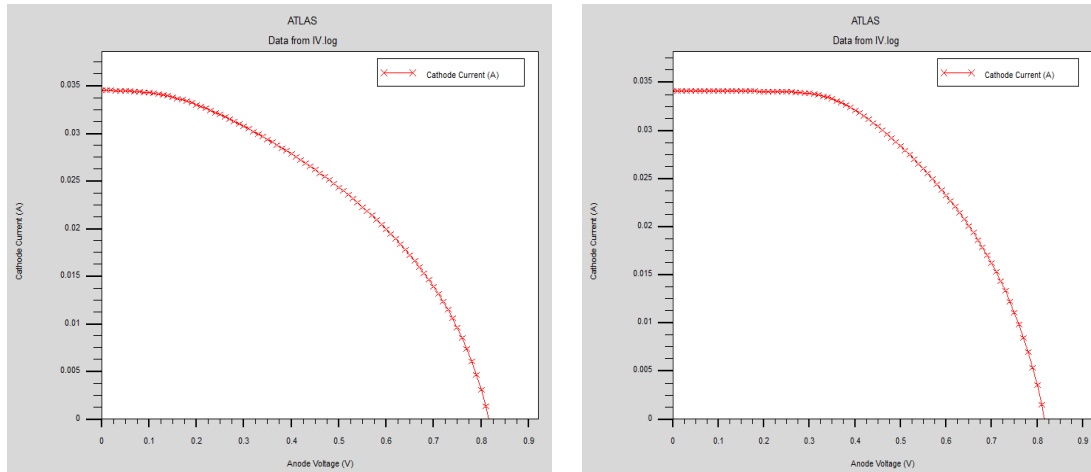
Figure 46.   Increasing AZO thickness. Left: 0.10µm, right: 0.30µm.
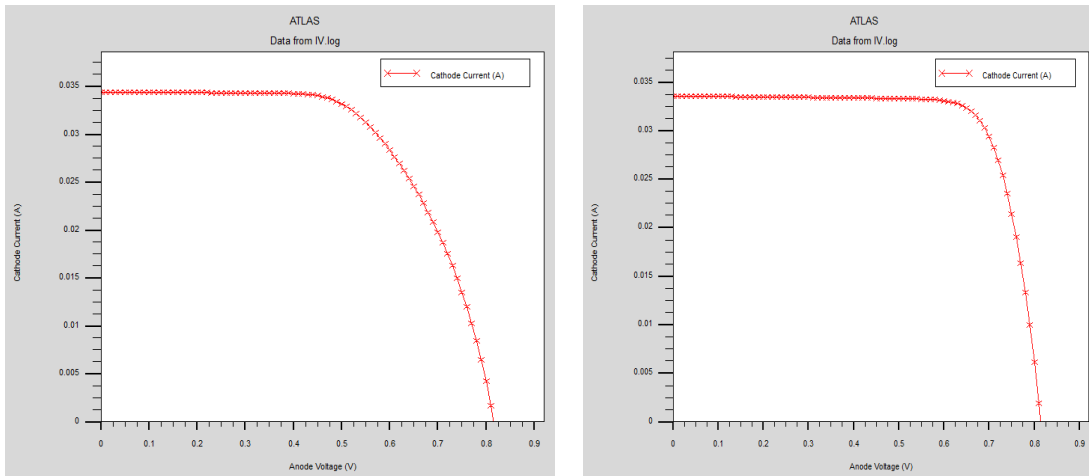
Figure 47.   Increasing ZnO thickness. Left: 0.10µm, right: 0.30µm.
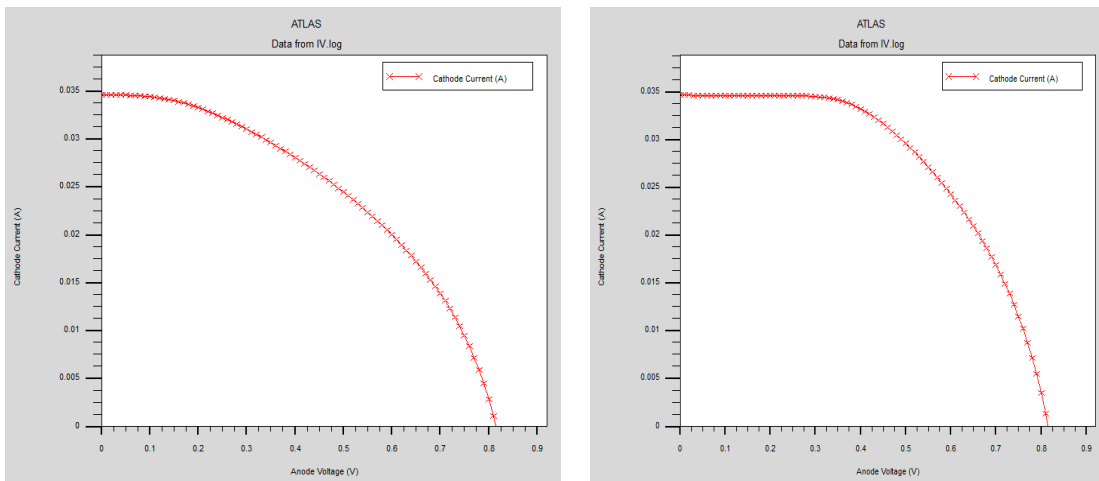
Figure 48.   Increasing CdS thickness. Left: 0.10µm, right: 0.30µm.

Table 8.   Experimental cell design trials optimal parameters.

	Experimental
AZO [μm]	0.05
ZnO [μm]	0.3
CdS [μm]	0.3
CIGS [μm]	2
CIGS+ [μm]	1
Mo [μm]	0.1
Var_width	0.15
Ga x	0.3
I_{SC} [mA]	33.34
V_{OC} [V]	0.814
P_M [mW]	21.43
V_M [V]	0.670
I_M [mA]	31.99
FF	0.790
Eff [%]	21.43
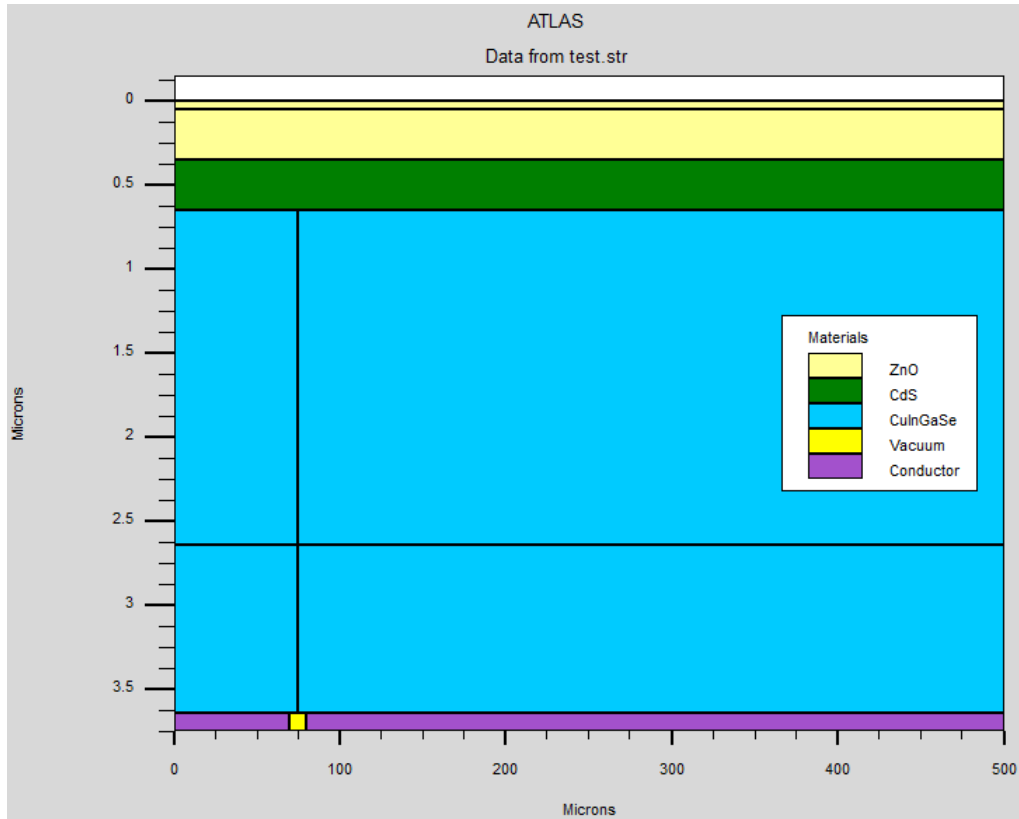
Figure 49.   Silvaco design of experimental cell in Table 8.

Based on the results of the baseline tests and primary trials of both cell architectures, we can clearly see that our experimental cell outperforms the SunPower model cell. Recognizing the validity of our models and the enhanced performance of our experimental cell, the remainder of this thesis will focus specifically on optimizing the experimental cell, however comparisons to the SunPower model will be made. Following experimentation with CIGS absorber thickness on all previously run trials, 2 μm proved to be an effective balance between cell performance and proper design architecture and will therefore be used in our passivation layer variation trials. Once an optimal cell structure is found, the Ga mole fraction and var_width parameters will be changed to further refine cell characteristics. Later our refined cell will be varied in temperature to observe its performance in varying environmental conditions.

Under the passivation layer variation trials, all possible combinations of each layer thickness from 0.05 μm to 0.30 μm are trialed. Between the initial trials and all combinations of the passivation layer thicknesses, a total of 228 trials were completed for our experimental cell design. Table 9 displays the cell parameters of the seven most efficient cells, those achieving over 21.30% efficiency.

Table 9.   Top seven performing cells under passivation layer trials.

	TRIAL NUMBER						
	#1	#2	#3	#4	#5	#6	#7
AZO [μm]	0.05	0.1	0.15	0.2	0.25	0.3	0.05
ZnO [μm]	0.3	0.3	0.3	0.3	0.3	0.3	0.3
CdS [μm]	0.3	0.3	0.3	0.3	0.3	0.3	0.25
CIGS [μm]	2	2	2	2	2	2	2
CIGS+ [μm]	1	1	1	1	1	1	1
Mo [μm]	0.1	0.1	0.1	0.1	0.1	0.1	0.1
Var_width	0.15	0.15	0.15	0.15	0.15	0.15	0.15
Ga x	0.3	0.3	0.3	0.3	0.3	0.3	0.3
I_{SC} [mA]	33.34	33.28	33.22	33.15	33.09	33.03	33.35
V_{OC} [V]	0.814	0.814	0.814	0.814	0.814	0.814	0.814
P_M [mW]	21.43	21.41	21.40	21.39	21.38	21.37	21.34
V_M [V]	0.670	0.670	0.680	0.680	0.680	0.680	0.670
I_M [mA]	31.99	31.96	31.47	31.45	31.44	31.42	31.86
FF	0.790	0.790	0.791	0.793	0.794	0.795	0.787
Eff [%]	21.43	21.40	21.39	21.38	21.37	21.36	21.34

Regarding the results from Table 9, it is interesting to note that all cells contain the largest thickness of both ZnO and CdS and that Trials 1-6 contain sequentially increasing AZO thicknesses. This confirms our previous analysis that both ZnO and CdS are the dominant materials regarding increased performance of this cell, as depicted in Figures 46-48. Using the cell proportions of Trial #1, Table 10 is derived by varying and recording the effects of varying Ga mole fraction. A mole fraction range slightly larger than the optimal window defined in Table 3 was used to verify trend analysis but remain low enough to not produce significant changes to the grain structure and its follow-on effects [22].

Table 10.   Effects of varying Ga mole fraction, x.

	MOLE FRACTION							
	x=0.20	x=0.22	x=0.24	x=0.26	x=0.28	x=0.30	x=0.32	x=0.34
I_{SC} [mA]	33.34	33.34	33.34	33.34	33.34	33.34	33.34	33.34
V_{OC} [V]	0.749	0.762	0.775	0.788	0.801	0.814	0.827	0.840
P_M [mW]	19.37	19.38	20.19	20.61	21.02	21.43	21.84	22.26
V_M [V]	0.610	0.620	0.630	0.640	0.650	0.660	0.670	0.690
I_M [mA]	31.76	31.90	31.55	31.71	31.85	31.99	31.66	31.81
FF	0.776	0.778	0.782	0.784	0.787	0.790	0.792	0.795
Eff [%]	19.36	19.77	20.19	20.60	21.01	21.43	21.84	22.26

Increased performance is expected when varying x due to the increasing CIGS bandgap, shown in Table 5. By raising the bandgap, only higher energy photons can cause photogeneration. Of particular interest are the high energy photons of blue light at approximately 400 nm wavelength vice the lower energy photons in the ultraviolet portion of the light spectrum. Using the maximum efficiency cell from Tables 9 and 10, Table 11 describes the effects of changing the var_width parameter. A minimum width of 5% was kept ensuring sufficiently large (25 µm) n-type material remained present to establish an electric field and maintain model validity.

Table 11.   Effect of varying n-p length on mole fraction optimized
experimental cell.

	VAR_WIDTH				
	VW=0.05	VW=0.10	VW=0.15	VW=0.20	VW=0.25
I_{SC} [mA]	37.23	35.29	33.34	31.40	29.46
V_{OC} [V]	0.840	0.840	0.840	0.840	0.840
P_M [mW]	24.33	23.32	22.26	21.15	20.03
V_M [V]	0.690	0.690	0.690	0.700	0.710
I_M [mA]	35.26	33.8	31.81	30.22	28.21
FF	0.778	0.787	0.795	0.802	0.809
Eff [%]	24.32	23.31	22.26	21.14	20.02

Based on Table 11, we observe that reducing the length of the n/n+ CIGS portion of the cell yields performance gains due to an increase in I_{SC}. This effect is expected since

minority carriers are responsible for current densities, and electrons are the minority carrier in p-type materials. Thus, by increasing the length of the p-type material a larger current density will occur. Additionally, the smaller the n-CdS to n-CIGS interface the more carriers can be separated by the electric field of the heterojunction. Figure 50 shows the physical construction of the optimized cell. Adapted from Tables 9-11, Table 12 describes the optimal cell based on the experimental variations performed in this thesis.
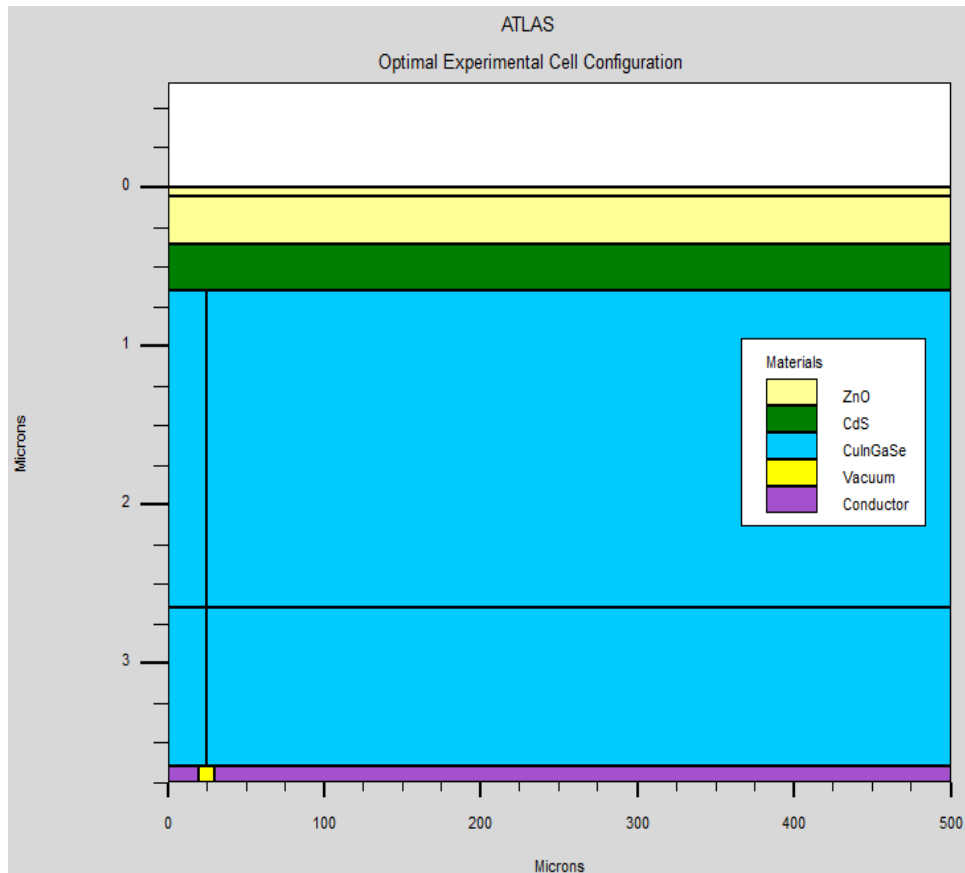
Figure 50.   Optimal experimental cell construction.

Table 12.   Experimental cell optimal parameters.

	Experimental
AZO [μm]	0.05
ZnO [μm]	0.3
CdS [μm]	0.3
CIGS [μm]	2
CIGS+ [μm]	1
Mo [μm]	0.1
Var width	0.05
Ga x	0.34
I_{SC} [mA]	37.23
V_{OC} [V]	0.840
P_M [mW]	24.33
V_M [V]	0.690
I_M [mA]	35.26
FF	0.778
Eff [%]	24.32

Having found the optimal parameters for our experimental cell we then observed the effects of the temperature environment. Table 13 lists the temperature effects on the optical parameters of the optimized cell described in Table 12. Temperature was varied from a nominal 300 K (26.85 °C) to 80 °C to simulate cell sun exposure on a warm, clear day. This simulation held a constant uniform temperature over the entire device to assess performance changes vice establishing a thermal gradient across the cell. Based on these results, experimentally derived temperature coefficients are provided in Table 14 and compared to those cited Fathi et al. [32]. Figure 51 depicts these effects on the I-V curves of this cell.

Table 13.   Temperature effects on optimal experimental cell.

	TEMPERATURE [°C]					
	T=26.85	T=40	T=50	T=60	T=70	T=80
I_{SC} [mA]	37.23	37.24	37.24	37.23	37.23	37.23
V_{OC} [V]	0.840	0.821	0.806	0.790	0.775	0.759
P_M [mW]	24.33	23.40	22.63	21.86	21.10	20.34
V_M [V]	0.690	0.660	0.640	0.620	0.610	0.590
I_M [mA]	35.26	35.45	35.36	35.26	34.59	34.48
FF	0.778	0.765	0.754	0.743	0.732	0.720
Eff [%]	24.32	23.39	22.62	21.86	21.09	20.33
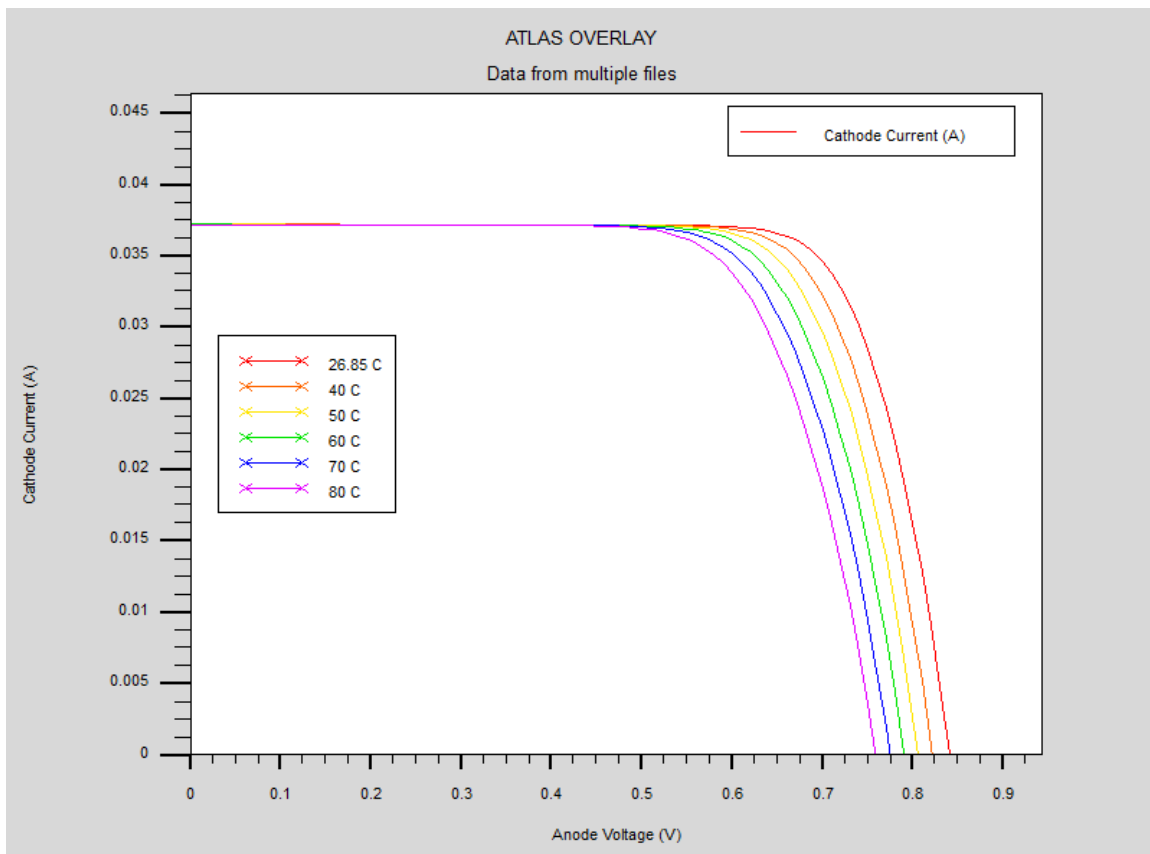
Figure 51.   I-V curves of cell described in Table 13.

Table 14.   Derived vs cited parameter temperature coefficients, experimental optimal cell.

Parameter	Derived Coefficient	Fathi et al. [32]
V_{OC} [mV/°C]	-1.5284	-2.0000
I_{SC} [mA/°C]	-0.0828	-0.0162
P_M [mW/°C]	-0.0750	-0.0780
FF [%/°C]	-0.1087	-0.0880
Eff [%/°C]	-0.0750	-0.0820

To compare the performance of our cell against the SunPower design of the same dimensions, Table 13, Figure 51, and Table 14 were reproduced using the SunPower model. The results of these test are shown in Table 15, Figure 52, and Table 16, respectively.

Table 15.   Temperature effects of SunPower cell with experimental cell optimal parameters.

	TEMPERATURE [°C]					
	T=26.85	T=40	T=50	T=60	T=70	T=80
I_{SC} [mA]	9.32	9.57	9.51	9.43	9.36	9.29
V_{OC} [V]	0.840	0.822	0.806	0.791	0.775	0.759
P_M [mW]	6.53	6.52	6.31	6.11	5.90	5.70
V_M [V]	0.750	0.730	0.710	0.690	0.680	0.660
I_M [mA]	8.71	8.93	8.89	8.85	8.68	8.64
FF	0.834	0.828	0.824	0.819	0.814	0.808
Eff [%]	6.53	6.51	6.31	6.10	5.90	5.70
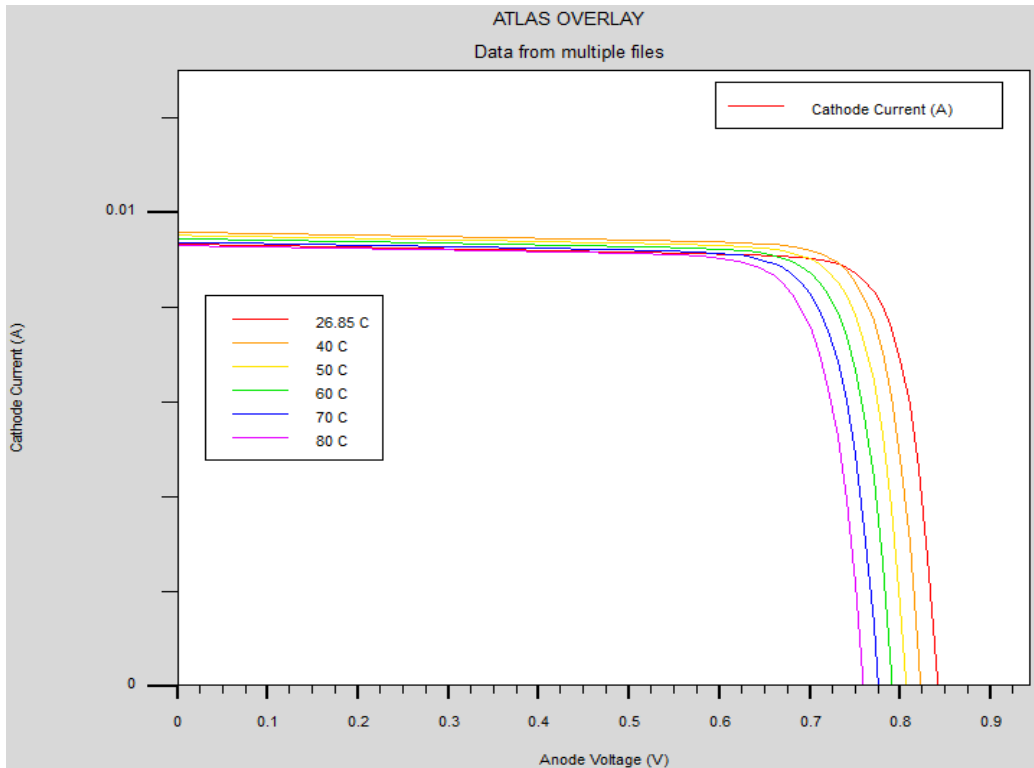
Figure 52.   I-V curves of cell described in Table 15.

Table 16.   Derived vs. cited parameter temperature coefficients, SunPower
cell with experimental cell optimal parameters.

Parameter	Derived Coefficient	Fathi et al. [32]
V_{OC} [mV/°C]	-1.5235	-2.0000
I_{SC} [mA/°C]	-0.0056	-0.0162
P_M [mW/°C]	-0.1557	-0.0780
FF [%/°C]	-0.0478	-0.0880
Eff [%/°C]	-0.0156	-0.0820

Figures 53-66 show various electrical properties and behaviors of our optimized cell due to its spectral response. Figure 53 displays the layered bandgap of materials in which the device is constructed. Figure 54 shows the photogeneration rate within the cell

under AM1.5 conditions. Figure 55 and Figure 56 denote the hole and electron concentrations within the cell under illumination.
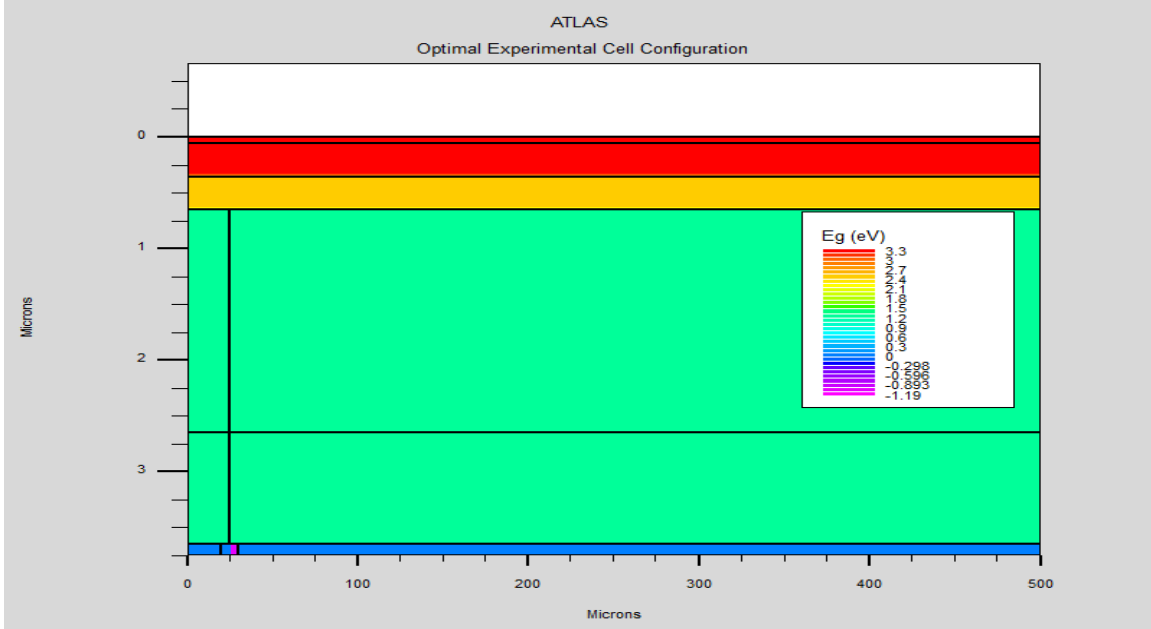
Figure 53.   Bandgap of optimal cell layers.
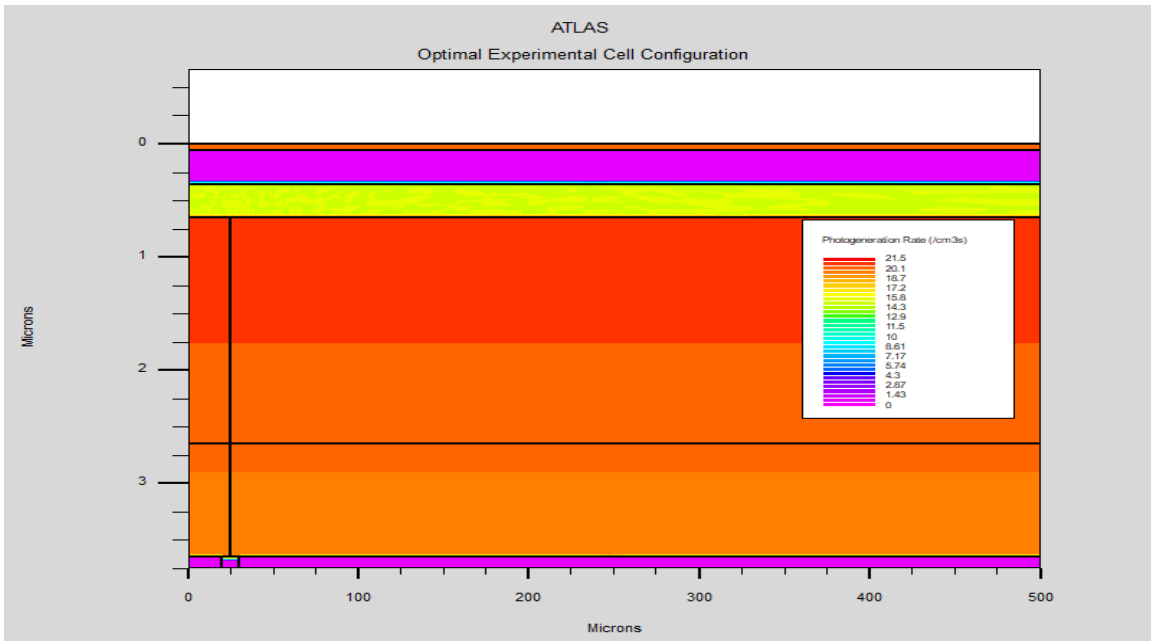
Figure 54.   Photogeneration within optimal cell under AM1.5 conditions.
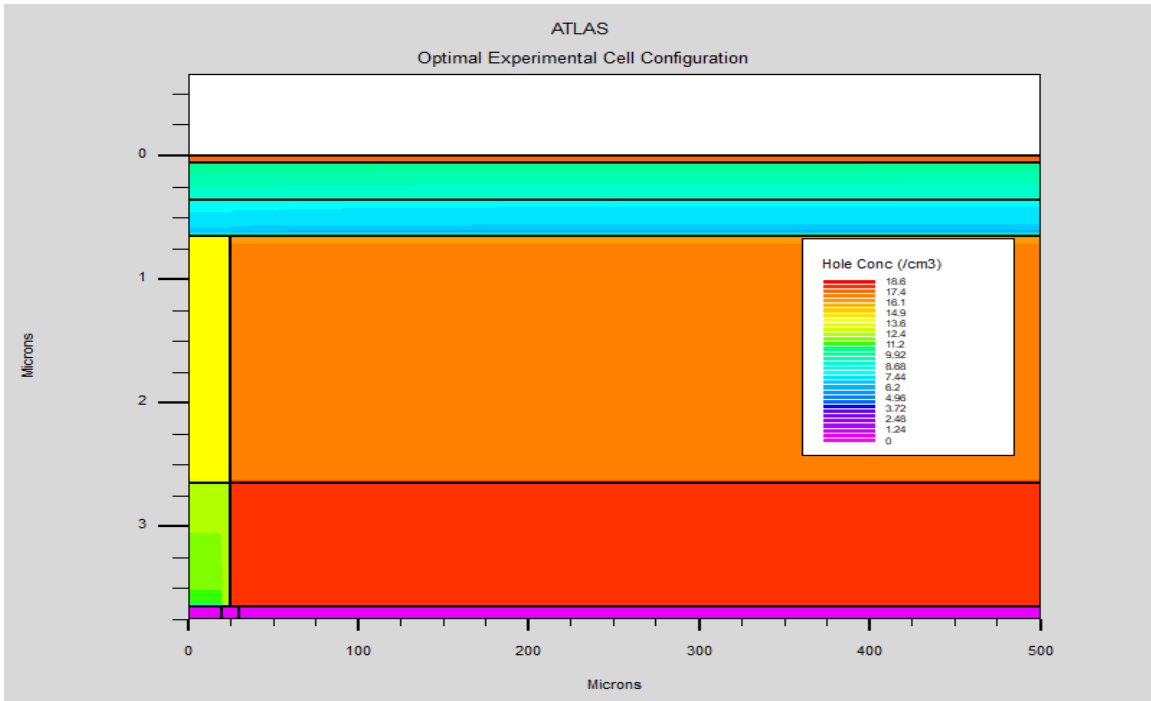
Figure 55.   Hole concentration within optimal cell under AM1.5 conditions.
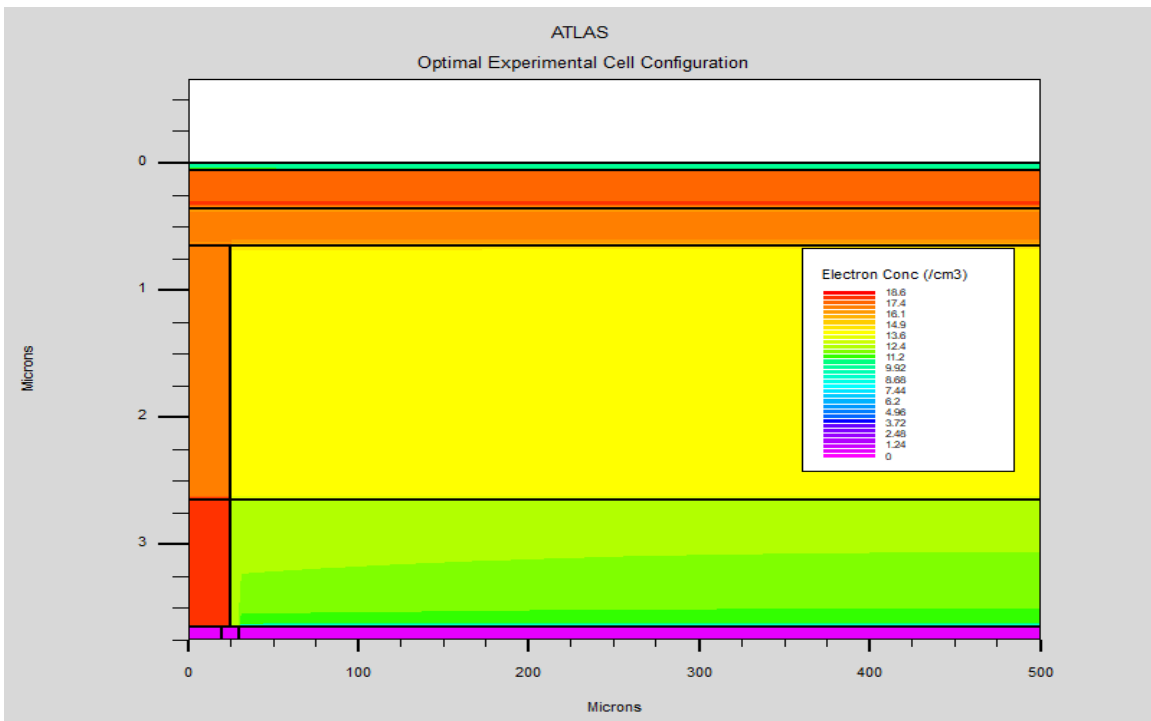
Figure 56.   Electron concentration within optimal cell under AM1.5 conditions.

We will now observe how our novel design affects cell performance under AM1.5 conditions. Figure 57 is an enlargement of the interfaces between the n-CIGS, p-CIGS, n+ CIGS and p+ CIGS regions to demonstrate the creation of the vertical electric field we desired to introduce. We observe an electric field of approximately 5 kV/cm at the BSF interface and approximately a 2.5 kV/cm electric field at the n-CIGS/p-CIGS interface. The intent of this field is to attract electrons to the n-CIGS region (left) while attracting holes to the p-CIGS region (region) after they have been pushed into the absorber by the p-n junction formed by CdS and CIGS. Figure 58 demonstrates how this concept works by showing the magnitude of the current flow lines within the cell under AM1.5 conditions. We can clearly see that the area surrounding the p-n interfaces contain current flow lines of significantly less magnitude than those at the extreme ends of the cell. This separation of charges is what limits recombination within the absorber and gives our cell the performance advantage over conventionally designed cells.
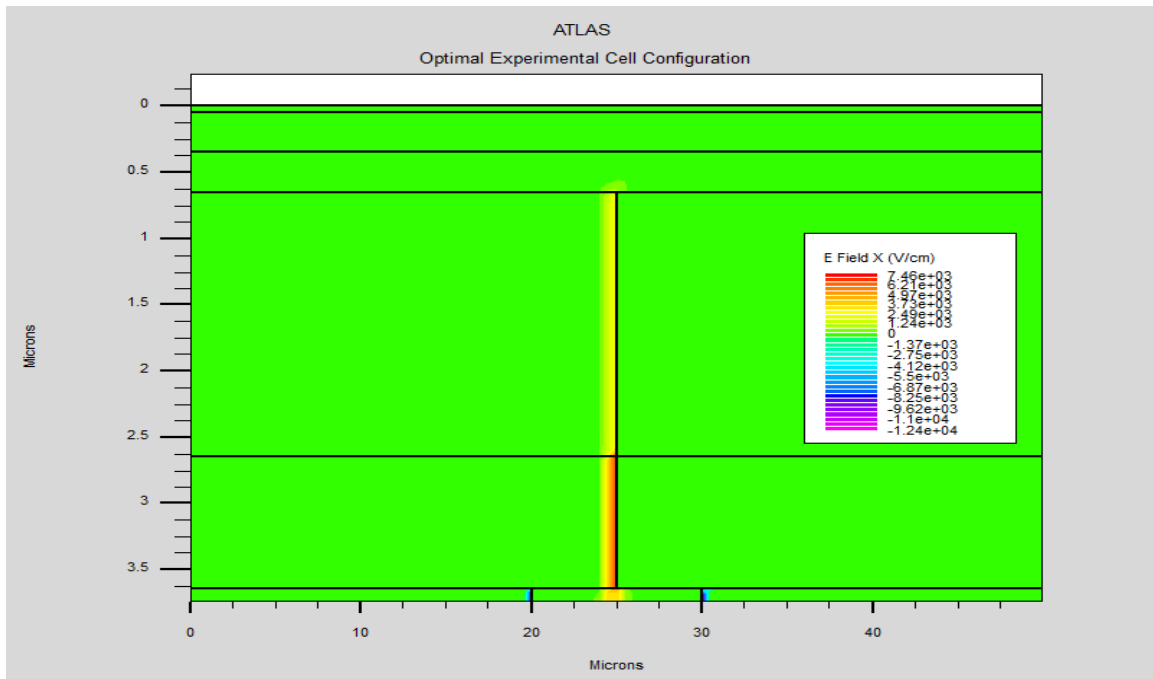
Figure 57.   Electric field produced by adjacent p-n interfaces in optimal cell.
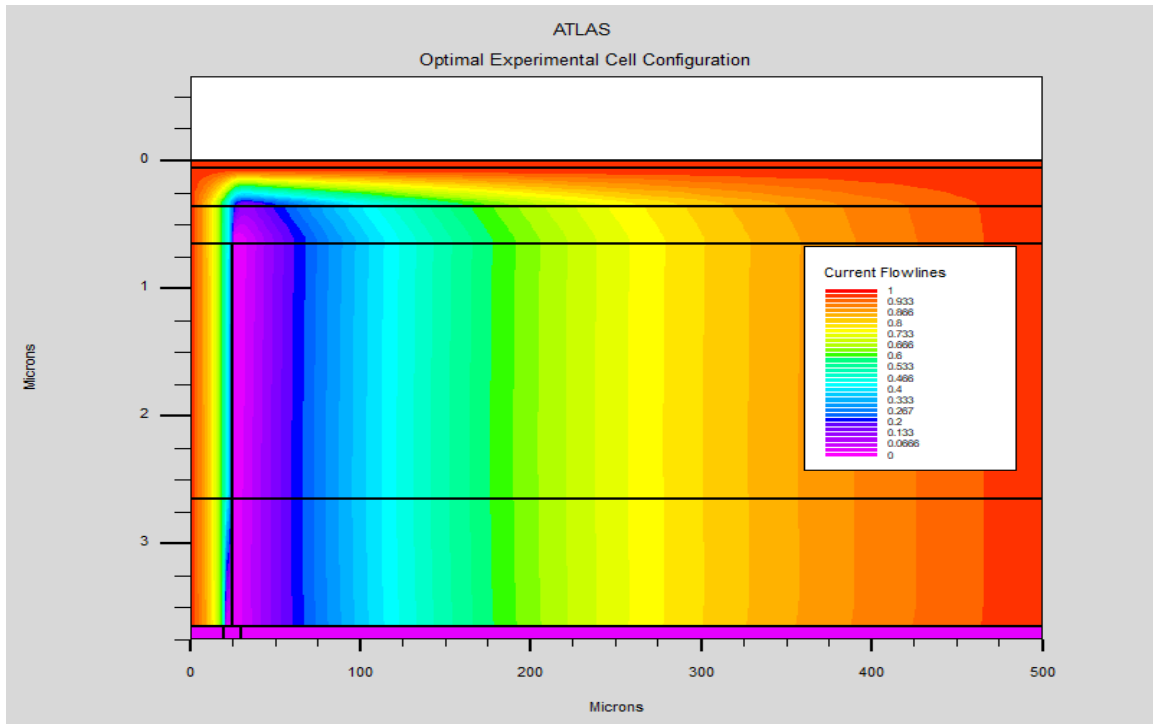
Figure 58.   Current flow lines in optimal cell under AM1.5 conditions.

Lastly, Table 17 compares the optimal cell designs of Herrera [3] and this thesis at 300 K. In addition to the 5.74% relative efficiency increase, our cell boasts a 79.45% reduction in cell thickness and therefore a significant reduction in cell weight. Not only does our cell bolster Herrera's research regarding extending PUMA flight duration, but also shows promising applications terrestrially or where weight is of significant concern. Of note, Herrera conducted his research prior to the CIGS bandgap equation in Silvaco being corrected. Since the error erroneously inflated the bandgap value for a given Ga mole fraction, his cell efficiency is likely lower than quoted and the relative efficiency increase of our cell is larger.

Table 17.   Comparison of optimal cell performances.

	Herrera	Exp. (Optimized)	Difference [%]
AZO [μm]	-	0.05	-
ZnO [μm]	0.40	0.3	-25.00
CdS [μm]	0.45	0.3	-33.33
CIGS [μm]	11	2	-82.82
CIGS+ [μm]	6	1	-83.33
Mo [μm]	0.40	0.1	-75.00
Tot.Thick.[μm]	18.25	3.75	-79.45
Var width	0.15	0.05	-
Ga x	0.45	0.34	-
I_{SC} [mA]	35.08	37.23	+6.13
V_{OC} [V]	0.845	0.840	-0.59
P_M [mW]	23.00	24.33	+5.78
V_M [V]	0.730	0.690	-5.48
I_M [mA]	31.50	35.26	+11.94
FF	0.776	0.778	+0.26
Eff [%]	23.00	24.32	+5.74

THIS PAGE INTENTIONALLY LEFT BLANK

VI.   CONCLUSION AND RECOMMENDATIONS

A.   CONCLUSION

After many trial and error experiments, our research objectives were achieved. Not only were we able to simulate CIGS and IBC in a single cell, but we also explored and further optimized Herrera's novel design as shown in Table 17 and discussed in Section 5B. The significant advances in cell efficiency and thickness reduction make our cell even more competitive in the PV market against the leading 23.4% efficient cell verified by NREL [41]. Cell construction and performance data can be viewed in Figures 44, 50, 51, and 53-58 and Tables 12-14, and 17.

Herrera [3] quoted difficulty replicating a working CIGS device utilizing the SunPower design architecture. Successful implementation of this model was achieved; however, its performance was championed by our novel design. Several comparisons were made between both models and I-V curves plotted against temperature. The SunPower version was trialed with the optimal parameters for the novel design and was again verified inferior. Replication of this cell design and its performance can be viewed in Figures 43 and 52, along with Tables 15-17.

Aside from the above performance accomplishments, our research serves as a launching point for future CIGS-related research. Having a consolidated list of relevant references, optimal layer parameters, well documented data from 228 trials, and knowledge of several layer correlation effects will assist in weighing the multitude of factors surrounding the construction of a solar cell. Examples of such correlations and their impact on optimization are discussed in detail in Section 5B. As new research comes to light, even further optimization can be performed to enhance the optical parameters or assist in the creation of a new cell design from the ground up.

B.   RECOMMENDATIONS

Due to its experimental nature, there were several assumptions made during the trial phases of this thesis that may not be true under all testing conditions. Some examples of these assumptions are constant doping concentrations, absorber thickness fixed at 2 μm,

static trial variable adjustment increments, and effects of temperature and mole fraction only being considered on the passivation layer optimized cell. We recommend using a high-performance computing environment to allow several variables to be changed at once in order to find more in-depth correlations between the effects of layer interactions and further optimizing cell parameters.

A relevant but infant field in photovoltaics is the incorporation of 3D printing into cell construction. This process could possibly ease manufacturing efforts and speed up production if a reputable method is discovered. Based on the simple geometries of this cell, recommend investigating the possibility of incorporating 3D into cell design.

The effects of radiation on solar cells are widely known in the photovoltaic industry. While CIGS is known for being rad-hard [24], recommend using Silvaco radiation simulation processes to investigate the effects on our novel CIGS IBC cell to gain a further understand of the physical interaction this cell has with nature. Favorable results from this experiment could make this design more favorable in radiation-dense environment, such as space.

Another novel design discussed during the creation of this thesis is the sectioning of a single cell so that it acts as a multijunction cell. Physically, this would require a form of insulator to separate the cell into multiple regions, say two for example. By connecting the two regions in series, the voltages would add and current be limited to the lower of the two. Since the cell is composed of the same material, the output voltage would be twice the original and current remain the same since it is a normalized parameter of the material. This type of cell would be extremely useful in applications where high voltages are required.

Rather than forcing a uniform temperature over the device to assess performance metrics, thermal simulation, such as Silvaco Giga, can obtain localized hot spot and thermal gradient data utilizing a thermal boundary condition. This simulation will show the most realistic performance changes and will be useful in determining the proper applications for our cell.

APPENDIX A. SILVACO CODE

The following code was produced by the author to complete the research performed in this thesis. It includes both the Sunpower model and novel design model. Variables may be different from the finalized versions used in Section 5B.

```
##################### SUNPOWER CELL DESIGN ###################
go atlas simflag="-P 8"
##### STRUCTURE DEFINITIONS #####
#Layer thicknesses
set AZO=            0.05
set ZnO=            0.30
set CdS=            0.30
set CIGS=           2.00
set CIGS_plus=      1.00
set Mo=             0.1
set gap=            10
#Y-dimensions
set L1=             $AZO
set L2=             $AZO+$ZnO
set L3=             $AZO+$ZnO+$CdS
set L4=             $AZO+$ZnO+$CdS+$CIGS
set L5=             $AZO+$ZnO+$CdS+$CIGS+$CIGS_plus
set L6=             $AZO+$ZnO+$CdS+$CIGS+$CIGS_plus+$Mo
#X-dimensions
set width=          500
set width3d=        100e6/$width
set div=            20
set var_width=      0.05*$width
set width_cat=      $var_width-($gap/2)
set width_ano=      $var_width+($gap/2)
#Miscellaneous
set x.comp=         0.34
set Eg_CIGS=        1.228
#ATLAS User Manual equation for Eg_CIGS verified wrong by Silvaco Engineer
(updated in version 5.32 only). Eg manually entered instead, change as needed below
# x=.20 Eg=1.1374    x=.22 Eg=1.150    x=.24 Eg=1.163    x=.26 Eg=1.176
# x=.28 Eg=1.189     x=.30 Eg=1.202    x=.32 Eg=1.215    x=.34 Eg=1.228


##### MESH #####
# Using Mesh 3D to normalize optical parameters to A/cm2
mesh width=  $width3d
```

```
x.mesh loc=0               spac=$width/$div
x.mesh loc=$width_cat      spac=$gap/($div/4)
x.mesh loc=$var_width      spac=$width/($div/4)
x.mesh loc=$width_ano      spac=$gap/($div/4)
x.mesh loc=$width          spac=$width/$div

y.mesh loc=0               spac=$L1/($div/4)
y.mesh loc=$L1             spac=$AZO/($div/4)
y.mesh loc=$L2             spac=$ZnO/($div/4)
y.mesh loc=$L3             spac=$CdS/($div/4)
y.mesh loc=($L4-$L3)/2     spac=($L4-$L3)/(2*$div)
y.mesh loc=$L4             spac=$CIGS/(3*$div)
y.mesh loc=$L5             spac=$CIGS_plus/(2*$div)
y.mesh loc=$L6             spac=$Mo/($div/2)

##### MATERIAL DEFINITIONS #####
region num=1  material=ZnO         x.min=0                    x.max=$width
      y.min=0             y.max=$L1
region num=2  material=ZnO         x.min=0                    x.max=$width
      y.min=$L1    y.max=$L2
region num=3  material=CdS         x.min=0                    x.max=$width
      y.min=$L2    y.max=$L3
region num=4  material=CIGS        x.min=0                    x.max=$width
      y.min=$L3    y.max=$L4       x.comp=$x.comp
region num=5  material=CIGS        x.min=0                    x.max=$var_width
      y.min=$L4    y.max=$L5       x.comp=$x.comp
region num=6  material=CIGS        x.min=$var_width  x.max=$width
      y.min=$L4    y.max=$L5       x.comp=$x.comp
region num=7  material=Molybdenum  x.min=0           x.max=$width_cat
      y.min=$L5    y.max=$L6 conductor
region num=8  material=Vacuum      x.min=$width_cat  x.max=$width_ano
      y.min=$L5    y.max=$L6
region num=9  material=Molybdenum  x.min=$width_ano  x.max=$width
      y.min=$L5    y.max=$L6 conductor

electrode name=cathode     num=1       x.min=0           x.max=$width_cat
      y.min=$L5    y.max=$L6
electrode name=anode       num=2       x.min=$width_ano  x.max=$width
      y.min=$L5    y.max=$L6

doping AL      uniform      conc=1e18     region=1
doping n.type  uniform      conc=1e18     region=2
doping n.type  uniform      conc=1e17     region=3
doping p.type  uniform      conc=8e16     region=4
doping n.type  uniform      conc=4e18     region=5
```

78

doping p.type uniform   conc=4e18   region=6

material region=1   EG300=3.3   AFFINITY=4.5   EPSILON=9
       NC300=2.2e18   NV300=1.8e19   MUN=100   MUP=25
       index.file='ZnO_Al.txt'
material region=2   EG300=3.3   AFFINITY=4.5   EPSILON=9
       NC300=2.2e18   NV300=1.8e19   MUN=100   MUP=25
       index.file='ZnO.txt'
material region=3   EG300=2.48   AFFINITY=4.18   EPSILON=10
       NC300=2.2e18   NV300=1.8e19   MUN=100   MUP=25
material material=CIGS   EG300=$Eg_CIGS   AFFINITY=4.26
       EPSILON=13.6   NC300=2.2e18   NV300=1.8e19   MUN=100
       MUP=25   COPT=5e-17 TAUN=2e-7   TAUP=2e-7 AUGN=8.3e-32
AUGP=1.8e-31
material material=Molybdenum
material material=Vacuum   real.index=1   imag.index=0

TRAPS
trap   material=ZnO donor   e.level=0   sign=1e-14   sigp=3e-13
        density=3e16 degen.fac=1   x.min=0   x.max=$width
        y.min=0   y.max=$L1
trap   material=ZnO donor   e.level=0   sign=1e-15   sigp=1e-15
        density=1e16 degen.fac=1   x.min=0   x.max=$width
        y.min=$L1   y.max=$L2
trap   material=CdS donor   e.level=0   sign=1e-15   sigp=1e-12
        density=1e16 degen.fac=1   x.min=0   x.max=$width
        y.min=$l2   y.max=$L3
trap   material=CIGS   acceptor   e.level=0   sign=4e-16   sigp=4e-14
        density=7.5e13   degen.fac=1   x.min=0   x.max=$width
        y.min=$L3   y.max=$L4
trap   material=CIGS   donor   e.level=0   sign=4e-16   sigp=4e-14
        density=7.5e13   degen.fac=1   x.min=0   x.max=$var_width
        y.min=$L4   y.max=$L5
trap   material=CIGS   acceptor   e.level=0   sign=4e-16   sigp=4e-14
        density=7.5e13   degen.fac=1   x.min=$var_width x.max=$width
        y.min=$L4   y.max=$L5

INTERFACES
s.x = semiconductor to insulator
s.s= semiconductor to semiconductor
s.m= semiconductor to metal
interface x.min=0   x.max=$width   y.min=0   y.max=0   s.n=45
        s.p=45 s.x
interface x.min=0   x.max=$width   y.min=$L1   y.max=$L1   s.n=5
        s.p=5   s.s

```
interface x.min=0           x.max=$width        y.min=$L2    y.max=$L2    s.n=5
        s.p=5   s.s
interface x.min=0           x.max=$width        y.min=$L3    y.max=$L3    s.n=5
        s.p=5   s.s
interface x.min=0           x.max=$var_width    y.min=$L4    y.max=$L4    s.n=5
        s.p=5   s.s
interface x.min=$var_width  x.max=$width        y.min=$L4    y.max=$L4    s.n=5
        s.p=5   s.s
interface x.min=0           x.max=$width_cat    y.min=$L5    y.max=$L5    s.n=45
        s.p=45 s.m
interface x.min=$width_ano  x.max=$width        y.min=$L5    y.max=$L5    s.n=45
        s.p=45 s.m
interface x.min=$width_cat  x.max=$width_ano    y.min=$L5    y.max=$L5    s.n=45
        s.p=45 s.x
interface x.min=$var_width  x.max=$var_width    y.min=$L3    y.max=$L4    s.n=5
        s.p=5   s.s
interface x.min=$var_width  x.max=$var_width    y.min=$L4    y.max=$L5    s.n=45
        s.p=45 s.m

# Refractive index of MgF2 = 1.413
interface     optical      ar.index=1.413      x.min=0       x.max=$width
        y.min=0      y.max=-0.1        coating=1
interface     optical      reflect=0.9         x.min=0       x.max=$width_cat
        y.min=$L5    y.max=$L5
interface     optical      reflect=0.9    x.min=$width_cat   x.max=$width
        y.min=$L5    y.max=$L5

contact num=1 name=cathode con.resist=.05e-8
contact num=2 name=anode   con.resist=.05e-8

# Verifying cell structure matches desired (see picture)
save out.file= "test.str"
tonyplot test.str

##### Modeling the cell #####
models srh fermi ni.fermi bgn optr auger print temp=300 bound.trap
method newton itlimit=100 maxtraps=20
output photogen recomb u.auger u.srh u.trap traps u.radiative  band.param con.band
val.band gaussian.band  flowlines opt.intens j.electron j.hole j.total j.drift j.diffusion
e.mobility h.mobility qfn qfp

##### Solar Spectrum #####
beam num=1 x.origin=$width/2 y.origin=-0.5 AM1.5 wavel.start=0.3 wavel.end=1.2
wavel.num=100 front.refl back.refl reflects=1 min.power=1e-6 angle=90
solve init
```

```
solve previous
# Solving illuminated condition
#solve b1=0.001
solve b1=0.01
solve b1=0.1
solve b1=0.5
solve b1=1.0

log outfile="IV.log"
# Sweeping anode voltage. Voc assumed to be around .8V
solve name=anode vanode=0        vstep=0.01    vfinal=0.85
log off
tonyplot IV.log
save outfile=  IBC_sweep.str
tonyplot       IBC_sweep.str

# Extracting optical parameters
extract init infile="IV.log"
# Short Circuit Current [uA]
extract name="Isc" y.val from curve(v."anode",i."cathode") where x.val=0.0
# Open Circuit Voltage [V]
extract name="Voc" x.val from curve(v."anode",i."cathode") where y.val=0.0
# Max Power [uW]
extract name="Pm" max(curve(v."anode",(v."anode"*i."cathode")))
# Voltage at Max Power [V]
extract name="Vm" x.val from curve(v."anode",(v."anode"*i."cathode")) where
y.val=$"Pm"
# Current at Max Power [uA]
extract name="Im" $"Pm"/$"Vm"
# Fill Factor
extract name="FF" $"Pm"/($"Isc"*$"Voc")
# Optical Intensity (P_spectrum_in)
extract name="Opt Int"       max(beam."1")
# Efficiency
extract name="Eff" (abs($"Pm")/$"Opt Int")

# Solving frequency response
solve b1=1 beam=1    lambda=0.3    wstep=0.01           wfinal=0.53
solve b1=1 beam=1    lambda=0.53   wstep=0.001          wfinal=0.54
solve b1=1 beam=1    lambda=0.54   wstep=0.01           wfinal=0.93
solve b1=1 beam=1    lambda=0.93   wstep=0.001          wfinal=0.94
solve b1=1 beam=1    lambda=0.94   wstep=0.00001        wfinal=0.95
solve b1=1 beam=1    lambda=0.95   wstep=0.01    wfinal=1.20
save outfile=  SP_IBC.str
tonyplot       SP_IBC.str
```

```
log outfile="IV.log"
# Sweeping anode voltage. Voc assumed to be around .8V
solve name=anode vanode=0        vstep=0.01     vfinal=0.83
log off
tonyplot IV.log
save outfile=  IBC_sweep.str
tonyplot        IBC_sweep.str


  #################### EXPERIMENTAL CELL DESIGN ###################

go atlas simflag="-P 8"
##### STRUCTURE DEFINITIONS #####
#Layer thicknesses
set AZO=            0.30
set ZnO=            0.30
set CdS=            0.25
set CIGS=           2.0
set CIGS_plus=      1
set Mo=             .1
set gap=            10
#Y-dimensions
set L1=             $AZO
set L2=             $AZO+$ZnO
set L3=             $AZO+$ZnO+$CdS
set L4=             $AZO+$ZnO+$CdS+$CIGS
set L5=             $AZO+$ZnO+$CdS+$CIGS+$CIGS_plus
set L6=             $AZO+$ZnO+$CdS+$CIGS+$CIGS_plus+$Mo
#X-dimensions
set width=          500
set width3d=        100e6/$width
set div=            20
set var_width=      0.15*$width
set width_cat=      $var_width-($gap/2)
set width_ano=      $var_width+($gap/2)
#Miscellaneous
set x.comp=         0.3
set Eg_CIGS=        1.2022
#ATLAS User Manual equation for Eg_CIGS verified wrong by Silvaco Engineer. Eg
manually entered instead
# x=.20 Eg=1.1374   x=.22 Eg=1.150     x=.24 Eg=1.163     x=.26 Eg=1.176
# x=.28 Eg=1.189    x=.30 Eg=1.202     x=.32 Eg=1.215     x=.34 Eg=1.228


##### MESH #####
#surface is 200 sq micron = 1/500000 sq cm
```

```
mesh width=   $width3d
x.mesh loc=0                 spac=$width/$div
x.mesh loc=$width_cat        spac=$gap/($div)
x.mesh loc=$var_width        spac=$width/$div
x.mesh loc=$width_ano        spac=$gap/$div
x.mesh loc=$width            spac=$width/$div

y.mesh loc=0                 spac=$L1/($div/2)
y.mesh loc=$L1               spac=$AZO/($div/2)
y.mesh loc=$L2               spac=$ZnO/($div/2)
y.mesh loc=$L3               spac=$CdS/($div/2)
y.mesh loc=($L4-$L3)/2       spac=($L4-$L3)/(2*$div)
y.mesh loc=$L4               spac=$CIGS/(3*$div)
y.mesh loc=$L5               spac=$CIGS_plus/(2*$div)
y.mesh loc=$L6               spac=$Mo/($div/2)

##### MATERIAL DEFINITIONS #####
region num=1  material=ZnO        x.min=0              x.max=$width
      y.min=0           y.max=$L1
region num=2  material=ZnO        x.min=0              x.max=$width
      y.min=$L1     y.max=$L2
region num=3  material=CdS        x.min=0              x.max=$width
      y.min=$L2     y.max=$L3
region num=4  material=CIGS       x.min=0              x.max=$var_width
      y.min=$L3     y.max=$L4
region num=5  material=CIGS       x.min=$var_width     x.max=$width
      y.min=$L3     y.max=$L4
region num=6  material=CIGS       x.min=0              x.max=$var_width
      y.min=$L4     y.max=$L5
region num=7  material=CIGS       x.min=$var_width     x.max=$width
      y.min=$L4     y.max=$L5
region num=8  material=Molybdenum     x.min=0          x.max=$width_cat
      y.min=$L5     y.max=$L6 conductor
region num=9  material=Vacuum     x.min=$width_cat     x.max=$width_ano
      y.min=$L5     y.max=$L6
region num=10 material=Molybdenum     x.min=$width_ano     x.max=$width
      y.min=$L5     y.max=$L6 conductor

electrode name=cathode       num=1        x.min=0           x.max=$width_cat
      y.min=$L5     y.max=$L6
electrode name=anode         num=2        x.min=$width_ano     x.max=$width
      y.min=$L5     y.max=$L6

doping AL      uniform        conc=1e18      region=1
doping n.type  uniform        conc=1e18      region=2
```

```
doping n.type  uniform        conc=1e17     region=3
doping n.type  uniform        conc=8e16     region=4
doping p.type  uniform        conc=8e16     region=5
doping n.type  uniform        conc=4e18     region=6
doping p.type  uniform        conc=4e18     region=7


material region=1    EG300=3.3    AFFINITY=4.5       EPSILON=9
        NC300=2.2e18      NV300=1.8e19      MUN=100    MUP=25
        index.file='ZnO_Al.txt'
material region=2    EG300=3.3    AFFINITY=4.5       EPSILON=9
        NC300=2.2e18      NV300=1.8e19      MUN=100    MUP=25
        index.file='ZnO.txt'
material region=3    EG300=2.48   AFFINITY=4.18      EPSILON=10
        NC300=2.2e18      NV300=1.8e19      MUN=100    MUP=25
material material=CIGS      EG300=$Eg_CIGS    AFFINITY=4.26
        EPSILON=13.6      NC300=2.2e18      NV300=1.8e19       MUN=100
        MUP=25     COPT=5e-17  AUGN=8.3e-32  AUGP=1.8e-31  TAUN=2e-7
TAUP=2e-7
material material=Molybdenum
material material=Vacuum          real.index=1   imag.index=0


##### TRAPS #####
trap    material=ZnO donor              e.level=0      sign=1e-14    sigp=3e-13
        density=3e16 degen.fac=1        x.min=0       x.max=$width
        y.min=0       y.max=$L1
trap    material=ZnO donor              e.level=0      sign=1e-15    sigp=1e-15
        density=1e16 degen.fac=1        x.min=0       x.max=$width
        y.min=$L1    y.max=$L2
trap    material=CdS donor              e.level=0      sign=1e-15    sigp=1e-12
        density=1e16 degen.fac=1        x.min=0       x.max=$width
        y.min=$l2    y.max=$L3
trap    material=CIGS       donor       e.level=0      sign=4e-16    sigp=4e-14
        density=7.5e13      degen.fac=1 x.min=0       x.max=$var_width
        y.min=$L3    y.max=$L4
trap    material=CIGS       acceptor    e.level=0      sign=4e-16    sigp=4e-14
        density=7.5e13      degen.fac=1 x.min=$var_width x.max=$width
        y.min=$L3    y.max=$L4
trap    material=CIGS       donor       e.level=0      sign=4e-16    sigp=4e-14
        density=7.5e13      degen.fac=1 x.min=0        x.max=$var_width
        y.min=$L4    y.max=$L5
trap    material=CIGS       acceptor    e.level=0      sign=4e-16    sigp=4e-14
        density=7.5e13      degen.fac=1 x.min=$var_width x.max=$width
        y.min=$L4    y.max=$L5


##### INTERFACES #####
```

```
interface x.min=0          x.max=$width      y.min=0      y.max=0      s.n=45
        s.p=45 s.x
interface x.min=0          x.max=$width      y.min=$L1    y.max=$L1    s.n=5
        s.p=5   s.s
interface x.min=0          x.max=$width      y.min=$L2    y.max=$L2    s.n=5
        s.p=5   s.s
interface x.min=0          x.max=$var_width  y.min=$L3    y.max=$L3    s.n=5
        s.p=5   s.s
interface x.min=$var_width x.max=$width      y.min=$L3    y.max=$L3    s.n=5
        s.p=5   s.s
interface x.min=0          x.max=$var_width  y.min=$L4    y.max=$L4    s.n=5
        s.p=5   s.s
interface x.min=$var_width x.max=$width      y.min=$L4    y.max=$L4    s.n=5
        s.p=5   s.s
interface x.min=0          x.max=$width_cat  y.min=$L5    y.max=$L5    s.n=45
        s.p=45 s.m
interface x.min=$width_ano x.max=$width      y.min=$L5    y.max=$L5    s.n=45
        s.p=45 s.m
interface x.min=$width_cat x.max=$width_ano  y.min=$L5    y.max=$L5    s.n=45
        s.p=45 s.x
interface x.min=$var_width x.max=$var_width  y.min=$L3    y.max=$L4    s.n=5
        s.p=5   s.s
interface x.min=$var_width x.max=$var_width  y.min=$L4    y.max=$L5    s.n=45
        s.p=45 s.m

# Refractive index of MgF2 = 1.413
interface     optical      ar.index=1.413     x.min=0
        x.max=$width       y.min=0             y.max=0              coating=1
interface     optical      reflect=0.9    x.min=0
        x.max=$width_cat   y.min=$L5      y.max=$L5
interface     optical      reflect=0.9    x.min=$width_cat   x.max=$width
        y.min=$L5     y.max=$L5

contact num=1 name=cathode con.resist=.05e-8
contact num=2 name=anode    con.resist=.05e-8

#save out.file= "test.str"
#tonyplot test.str

##### Modeling the cell #####
models srh fermi ni.fermi bgn optr auger print temp=300 bound.trap
method gummel newton itlimit=200 maxtraps=20
output photogen recomb u.auger u.srh u.trap traps u.radiative   band.param con.band
val.band gaussian.band   flowlines opt.intens j.electron j.hole j.total j.drift j.diffusion
e.mobility h.mobility qfn qfp
```

85

```
#Solar spectrum
beam  num=1  x.origin=$width/2  y.origin=-0.5  AM1.5  wavel.start=0.3  wavel.end=1.2
wavel.num=100 front.refl back.refl reflects=1 min.power=1e-6 angle=90
solve init
solve previous
# Solving illuminated condition
# b#=# --> beam # intensity
solve b1=0.001
solve b1=0.01
solve b1=0.1
solve b1=0.5
solve b1=1.0

log outfile="IV.log"
solve vanode=0 name=anode vstep=0.01 vfinal=0.83
log off
tonyplot IV.log
#save outfile= IBC_sweep.str
#tonyplot     IBC_sweep.str

extract init infile="IV.log"
extract name= "Isc"        y.val from curve(v."anode",i."cathode") where x.val=0.0
extract name= "Voc"        x.val from curve(v."anode",i."cathode") where y.val=0.0
extract name= "Pm"         max(curve(v."anode",(v."anode"*i."cathode")))
extract name= "Vm"         x.val from curve(v."anode",(v."anode"*i."cathode")) where
y.val=$"Pm"
extract name="Im"          $"Pm"/$"Vm"
extract name="FF"          $"Pm"/($"Isc"*$"Voc")
extract name="Opt Int"     max(beam."1")
extract name="Eff"         (abs($"Pm")/$"Opt Int")

# Solving frequency response
# lambda = starting wavelength
# wstep = step size
# wfinal = final wavelength
# extract function syntax in DevEdit User Manual pg 150
# ow.""=        optical wavelength
# spc.""=       source photo current
# apc.""=       available photo current
solve b1=1 beam=1    lambda=0.3    wstep=0.01      wfinal=0.53
solve b1=1 beam=1    lambda=0.53   wstep=0.001     wfinal=0.54
solve b1=1 beam=1    lambda=0.54   wstep=0.01      wfinal=0.93
solve b1=1 beam=1    lambda=0.93   wstep=0.001     wfinal=0.94
solve b1=1 beam=1    lambda=0.94   wstep=0.00001   wfinal=0.95
```

```
solve b1=1 beam=1    lambda=0.95   wstep=0.01                wfinal=1.20
save outfile=   ATL_IBC.str
tonyplot        ATL_IBC.str




##### BELOW NOT EXPLORED IN THIS THESIS #####

#Plotting EQE
beam  num=2  x.origin=$width/2  y.origin=-.5  AM1.5  wavel.start=.3  wavel.end=1.2
wavel.num=50 front.refl back.refl reflects=1 min.power=1e-6
#solve   init
log outfile=    CIGS_EQE.log
solve  b2=1   beam=2        lambda=.3        wstep=.05        wfinal=1.2
log off
tonyplot        CIGS_EQE.log

extract init inf=       "CIGS_EQE.log"
extract name=          "EQE" curve(ow."2",abs(i."cathode")/spc."2") outf="EQE.dat"
extract name=          "IQE" curve(ow."2",abs(i."cathode")/apc."2") outf="IQE.dat"
tonyplot               -overlay IQE.dat EQE.dat
tonyplot               EQE.dat

#Plotting spectrum power density vs cell power output power density
beam  num=4  x.origin=$width/2  y.origin=-.5  AM1.5  wavel.start=.3  wavel.end=1.2
wavel.num=500 front.refl back.refl reflects=1 min.power=1e-6 out.power=spectrum.log
solve init
solve previous
solve vanode=1.0
log outfile=    CIGS_pwr.log
solve b4=1    beam=4        lambda=.3        wstep=.05        wfinal=1.3
log off

#extract function syntax in DevEdit User Manual pg 150
#ow.""=        optical wavelength
#spc.""=       source photo current
#apc.""=       available photo current
extract init inf=        "CIGS_pwr.log"
extract name=           "CIGS_pwr"    curve(ow."4",(v."anode"*i."cathode"*1e3/$width))
outf=                   "CIGS_pwr.dat"
extract name=           "spectrum_pwr"
curve(ow."4",spc."4"*1e3/$width)*(1.24/ow."4"))) outf=spectrum_pwr.dat
tonyplot               -overlay spectrum_pwr.dat CIGS_pwr.dat
```

THIS PAGE INTENTIONALLY LEFT BLANK

APPENDIX B. SILVACO MATERIAL INDEX FILES

This section includes the n and k values of different materials at different wavelengths and was required because Luminous (Silvaco solar simulator) did not contain all necessary wavelengths for all materials. These materials were taken from research instead and used in lieu of the pre-coded Luminous values. Copy thesis sections into .txt files to use in material definitions as done in the material region command in Appendix A. The format for how to create this text file is in the ATLAS user manual.

Molybdenum

nm
51

300	1.6	2.53
320	1.76	2.52
340	1.86	2.51
360	1.92	2.53
380	1.96	2.57
400	2	2.63
420	2.04	2.69
440	2.09	2.77
460	2.14	2.86
480	2.21	2.95
500	2.31	3.03
520	2.42	3.07
540	2.51	3.07
560	2.56	3.07
580	2.59	3.08
600	2.62	3.11
620	2.65	3.14
640	2.69	3.17
660	2.72	3.19
680	2.76	3.21
700	2.78	3.22
720	2.8	3.23
740	2.81	3.23
760	2.81	3.23
780	2.8	3.24
800	2.78	3.24
820	2.75	3.25
840	2.72	3.27

860	2.68	3.29
880	2.63	3.31
900	2.58	3.35
920	2.52	3.39
940	2.46	3.44
960	2.41	3.5
980	2.35	3.57
1000	2.29	3.64
1020	2.24	3.72
1040	2.19	3.8
1060	2.14	3.89
1080	2.1	3.99
1100	2.06	4.09
1120	2.02	4.19
1140	1.99	4.29
1160	1.96	4.39
1180	1.94	4.49
1200	1.92	4.6
1220	1.9	4.7
1240	1.89	4.8
1260	1.88	4.9
1280	1.87	5.01
1300	1.86	5.11

ZnO
nm
51

300	1.99	0.46
320	2.06	0.45
340	2.13	0.43
360	2.21	0.39
380	2.32	0.3
400	2.3	0.07
420	2.19	0.03
440	2.14	0.02
460	2.1	0.01
480	2.07	0.01
500	2.05	0.01
520	2.04	0.01
540	2.03	0
560	2.02	0
580	2.01	0
600	2	0
620	1.99	0

640	1.99	0
660	1.98	0
680	1.98	0
700	1.97	0
720	1.97	0
740	1.97	0
760	1.96	0
780	1.96	0
800	1.96	0
820	1.96	0
840	1.95	0
860	1.95	0
880	1.95	0
900	1.95	0
920	1.95	0
940	1.95	0
960	1.94	0
980	1.94	0
1000	1.94	0
1020	1.94	0
1040	1.94	0
1060	1.94	0
1080	1.94	0
1100	1.94	0
1120	1.94	0
1140	1.94	0
1160	1.94	0
1180	1.94	0
1200	1.94	0
1220	1.94	0
1240	1.94	0
1260	1.94	0
1280	1.94	0
1300	1.94	0

ZnO_Al

nm
51
300	2.52	0.44
320	2.46	0.26
340	2.37	0.14
360	2.28	0.07
380	2.2	0.03
400	2.14	0.02

420	2.09	0.01
440	2.05	0
460	2.02	0
480	2	0
500	1.98	0
520	1.96	0
540	1.95	0
560	1.93	0
580	1.92	0
600	1.91	0
620	1.9	0
640	1.9	0
660	1.89	0
680	1.88	0
700	1.87	0
720	1.87	0
740	1.86	0
760	1.85	0
780	1.85	0
800	1.84	0
820	1.84	0
840	1.83	0
860	1.83	0
880	1.82	0
900	1.82	0
920	1.81	0
940	1.81	0
960	1.8	0.01
980	1.8	0.01
1000	1.8	0.01
1020	1.79	0.01
1040	1.79	0.01
1060	1.78	0.01
1080	1.78	0.01
1100	1.77	0.01
1120	1.77	0.01
1140	1.76	0.01
1160	1.76	0.01
1180	1.75	0.01
1200	1.75	0.02
1220	1.74	0.02
1240	1.73	0.02
1260	1.73	0.02
1280	1.72	0.02
1300	1.72	0.03

APPENDIX C. PROGRAMMER NOTES

The purpose of this Appendix is to provide programming recommendations for new Silvaco users based on experience gained during this thesis. While no programming ability is necessary to begin using its features, familiarity with general syntax structure is recommended. Like MATLAB, Silvaco calls a series of commands to execute certain functions, making it the user's job to apply the correct syntax, variables, and models to achieve the desired output. Simply because the program executes without error does not mean the output is correct or even logical. Always review the simulation print for warning and errors as Silvaco may continue to execute the code after ignoring crucial information.

- Review your sources for errors! During research, it was discovered that the CIGS bandgap calculation performed by the Silvaco software disagreed with the journal article calculation quoted in its user manual. This mismatch was confirmed and corrected by Silvaco engineers for the newest software version (ATLAS 5.32.1.R at the time of this thesis). Similar grammatical and numerical mistakes are possible in journal articles and scholarly papers so always pull information from multiple sources when possible.

- Width3d: calculates the width of the third dimension required to achieve an area of 1 cm^2. This statement was incredibly useful in calculating the optical parameters since test cells can be configured in any size. Setting the mesh width to the value of width3d eliminated the need to perform unit conversions when calculating performance metrics.

- Reference the ATLAS and DevEdit user manual often. Several syntax changes were observed between prior theses code and those required to complete this thesis. Additionally, default units may differ from those desired, such as the default unit of length being microns instead of centimeters or meters. Older syntax might not flag while searching the document so use the table of contents or keywords of the desired function

to help narrow down relevant sections of the text. The appendices also contain very useful information, such as lists of available materials and their electrical or optical parameters.

- Read old code to familiarize yourself with general syntax and function calls. Search the user manual for any unfamiliar syntax and note whether it is relevant to your simulation as some models only apply to certain materials. For example, the "conmob" model used in prior theses researching GaAs is irrelevant to this thesis as that model only applies to Si and GaAs.

- Use variables whenever possible when creating your device to minimize the amount of code changes required to execute different trials. Not only will this save you time but also minimizes human error. Code using variables linked to device dimensions will automatically adjust following any changed made to device size or orientation.

- Create and review .str files following any significant changes to your device to help narrow down possible sources of error in your simulation. Reviewing mesh construction, region definitions, dopant concentrations, electrode placements, etc. for accuracy ensures your device is created as intended prior to simulation. Following review, simply comment out the save and Tonyplot commands to minimize obstruction. Review of devices after simulation can verify expected behaviors or ensure the simulation ran as desired. For example, early on it was noticed that placing the light beam at 0.25 microns did not illuminate the ensure top surface of the cell. A simple heigh adjustment to .5 microns above the cell allowed full illumination.

- The SOPRA appendix of the ATLAS user manual contains complex refractive index files of numerous materials, however not all files encompass the full spectrum of wavelengths you may wish to simulate.

Luminous will automatically use these files if defined in your simulation, however user defined text files can also be used. For example, this thesis utilized user defined information for AZO, ZnO and CdS from [21] due to the SOPRA file for CdS only ranging from 0.35-0.9 μm when the desired simulation was from 0.3–1.2 μm. Proper syntax to execute this can be reviewed in the user manual and Appendix A. Text file ready versions of this data can be reviewed in Appendix B.

- Stay organized. Group similar functions together and make ample comments to denote important sections or lines of code. Similarly, adopt a file naming and storage convention and stick to it to recall trials for re-execution. Keep electronic records of everything, especially simulation prints and figures. Recommend using a cloud storage system, such as Box or OneDrive, to ensure your files will not be lost if anything happens to your computer. This also lets you access your data from any computer for remote work. Frequently verify that the most current edition of your research is uploaded to your storage before closing your programs or leaving for the weekend or a holiday break.

- Depending on the complexity of your device, trials may take quite some time to complete. Utilize this downtime for other research related efforts.

- Achieving convergence can be tricky. Lack of convergence can occur for a variety of reasons but is most commonly due to mesh coarseness, iteration limit (method), max traps (method) or step size (solve). Try adjusting these parameters before adjusting your model entirely. Using the Gummel method may give the simulator a good initial guess for the solve function before using the Newton method to further assist convergence. Recommend raising the iteration limit and max traps above the default to prevent simulation timeout before a possible solution is achieved. Several instances were noted when convergence occurred at iterations in the 90s whereas the default limit is 25.

- Make your own Figures with Microsoft Visio if you cannot find any suitable images to portray your research. Figures 22, 40, and 41 were created to allow the reader to visually understand our though process and intentions when simulating our cell.

LIST OF REFERENCES

[1] SunPower Corporation, More power. A better investment. [Online]. Available: https://silo.tips/download/more-power-a-better-investment

[2] J. O'Connor, "Design and simulation of novel, high-efficiency, back-contact solar cells" Ph. D dissertation, Dept. of Elec. & Comp. Eng., NPS, Monterey, CA, USA, 2015.

[3] J. Herrera, "Novel design of copper indium gallium diselenide (CIGS) solar cell with application on UAS puma 3 AE," M.S. thesis, Dept. of Elec. & Comp. Eng., NPS, Monterey, CA, USA, 2015. [Online]. Available: https://calhoun.nps.edu/handle/10945/67203

[4] K. Fotis, "Modeling and simulation of dual-junction CIGS solar cell using Silvaco ATLAS," M.S. thesis, Dept. of Elec. & Comp. Eng., NPS, Monterey, CA, 2012.

[5] D. Columbus, "Design and optimization of copper indium gallium selenide solar cells for lightweight battlefield application," M.S. thesis, Dept. of Elec. & Comp. Eng., NPS, Monterey, CA, 2014. [Online]. Available: https://calhoun.nps.edu/handle/10945/42600

[6] S. Green, "Interdigitated back-surface-contact solar cell modeling using Silvaco ATLAS," M.S. thesis, Dept. of Elec. & Comp. Eng., NPS, Monterey, CA, USA, 2015. [Online]. Available: https://calhoun.nps.edu/handle/10945/45861

[7] R. Hazen, "Light-matter interactions at the atomic level." Accessed October 7, 2021 [Online]. Available: https://www.thegreatcoursesdaily.com/light-matter-interactions-at-the-atomic-level/

[8] C. Hu, and R.M. White, *Solar Cells: From Basic to Advanced Systems*, New York, NY, USA: McGraw Hill 1983.

[9] Wikipedia, "Electronic band structure." Accessed September 12, 2021 [Online]. Available: https://en.wikipedia.org/wiki/Electronic_band_structure

[10] P. Michalopoulous, "A novel approach for the development and optimization of state-of-the-art photovoltaic devices using Silvaco," M.S. thesis, Dept. of Elec. & Comp. Eng., NPS, Monterey, CA, USA, 2002. [Online]. Available: https://calhoun.nps.edu/handle/10945/5609

[11] Lumen, "States of matter, unit cells." Accessed September 16, 2021 [Online]. Available: https://courses.lumenlearning.com/cheminter/chapter/unit-cells/

[12]   K. Jager, O. Isabella, A. Smets, R. A. van Swaaij, and M. Zeman, *Solar Energy: Fundamentals, Technology, and Systems*, Delft University of Technology, 2014. [Online]. Available: https://courses.edx.org/c4x/DelftX/ET.3034TU/asset/solar_energy_v1.1.pdf

[13]   J. Blom, "Diodes." Accessed October 1, 2021 [Online]. Available: https://learn.sparkfun.com/tutorials/diodes/real-diode-characteristics

[14]   C. Honsberg and S. Bowden, "PV Education." Accessed November 15, 2021 [Online]. Available: https://www.pveducation.org/

[15]   J. Jeong, "Photovoltaics: measuring the 'sun'." Accessed October 13, 2021 [Online]. Available: https://www.laserfocusworld.com/lasers-sources/article/16566681/photovoltaics-measuring-the-sun

[16]   S. Michael, "'EC3230- Space power and radiation effect' lecture notes," unpublished.

[17]   A. Bates, "Novel optimization technique for multijunction solar cell design using Silvaco ATLAS", M.S. thesis, Dept. of Elec. & Comp. Eng., NPS, Monterey, CA, USA, 2004. [Online]. Available: https://calhoun.nps.edu/handle/10945/46458

[18]   Solargis, "Solar resource maps of World," Accessed October 28, 2021 [Online]. Available: https://solargis.com/maps-and-gis-data/download/world

[19]   M. Lammert and R. Schwartz, "Silicon solar cells for high concentration applications" in *Proc. Electron Devices Mtg*, 1975, pp. 350-352. [Online]. doi: 10.1109/IEDM.1975.188896

[20]   S. Kuo, M. Hsieh, D. Hsieh, H. Kuo, C. Chen, and F. Lai, "Device modeling of the performance of Cu(In,Ga)Se2 solar cells with v-shaped bandgap profiles" *International Journal of Photoenergy*, 2014. [Online]. Available: https://www.hindawi.com/journals/ijp/2014/186579/

[21]   M. Richter, C. Schubbert, P. Eraerds, I. Riedel, J. Keller, J. Parisi, T. Dalibor, and A. Avellan-Hampe, "Optical characterization and modeling of Cu(In,Ga)(Se,S)2 solar cells with spectroscopic ellipsometry and coherent numerical simulation" *Thin Solid Films*, vol *535*, 2013, pp. 331-335. [Online]. doi: 10.1016/j.tsf.2012.11.078

[22]   K. Nagaich, S. Campbell and E. Aydil, "Wide band-gap CuIn1−XGaXSe2 based chalcopyrite absorbers for tandem cell applications," in *37th IEEE Photo. Spec. Conf.*, 2011, pp. 425-429. [Online]. doi: 10.1109/PVSC.2011.6185984

[23]   M. Contreras, L. Mansfield, B. Egaas, J. Li, M. Romero, R. Noufi, E. Rudiger-Voigt, and W. Mannstadt, "Improved energy conversion efficiency in wide-bandgap Cu(In,Ga)Se2 solar cells" in *37ᵗʰ IEEE Photo. Spec. Conf.*, 2011, pp. 26-31. [Online]. doi: 10.1109/PVSC.2011.6185837

[24]   W. Shafarman and L. Stolt, *Handbook of Photovoltaic Science and Engineering*, John. Wiley & Sons, 2003, ch. 13, pp. 567-616. [Online]. doi: 10.10002/0470014008

[25]   S. Bae, H. Zhao, Y. Hsieh, L. Zuo, N. deMarco, Y. Rim, G. Li, Y. Yang, "Printable solar cells from advanced solution-processible materials" in *Chem 1*, 2016, pp. 197-219. [Online]. doi: 10.1016/j.chempr.2016.07.010

[26]   Silvaco, Inc., Atlas User Manual, Santa Clara, CA, 2020.

[27]   M. Hsieh, S. Kuo, F. Lai, M. Kao, P. Huang, H. Wang, M. Tsai, and H. Kuo, "Optimization of CdS buffer layer on the performance of copper indium gallium selenide solar cells" in 2011 Conference on Lasers and Electro-Optics Pacific Rim, 2011. [Online]. Available: https://opg.optica.org/abstract.cfm?uri=cleopr-2011-C765

[28]   I. Gharibshahian, A. Abbasi, and A. Orouji, "Modeling of GaAsxP1-x/CIGS tandem solar cells under stress conditions" *Superlattices and Microstructures,* vol. 153, 2021, pp. 106860-106865.

[29]   S. Sharbati, I. Gharibshahian, and A. Orouji, "Designing of AlxGa1-xAs/CIGS tandem solar cell by analytical model" *Solar Energy* vol.188, 2019, pp 1-9.

[30]   M. Asaduzzaman, M. Hosen, M. Ali, and A. Bahar, "Non-toxic buffer layers in flexible Cu(In,Ga)Se2 photovoltaic cell applications with optimized absorber thickness" *International Journal of Photoenergy*, 2017. [Online]. doi: 10.1155/2017/4561208

[31]   C. Larez, C. Bellabarba, and C. Rincon, "Alloy composition and temperature dependence of the fundamental absorption edge in CuGaxIn1-xSe2" in *Applied Physics Letters 65*, 1994, pp. 1650-1652. [Online]. doi: 10.1063/1.112944

[32]   M. Fathi, M. Abderrezek, F. Djahli, and M. Ayad, "Study of thin film solar cells in high temperature condition" in *Energy Procedia 74*, 2015, pp. 1410-1417. [Online]. doi: 10.1016/j.egypro.2015.07.788

[33]   A. Han, Y. Zhang, W. Song, B. Li, W. Liu, and Y. Sun, "Structure, morphology and properties of thinned Cu(In,Ga)Se2 films and solar cells" *Semiconductor Science and Technology*, vol 27, 2012. [Online]. Available: https://iopscience.iop.org/article/10.1088/0268-1242/27/3/035022/meta

[34]   N. Amin, M. Tang, and K. Sopian, "Numerical modeling of the copper-indium-selenium (CIS) based solar cell performance by AMPS-1D" in *5th Student Conf. on Research and Dev. (SCOReD)*, 2007, pp. 1-6. [Online]. doi: 10.1109/SCORED.2007.4451382

[35]   A. Bauer, S. Sharbati, and M. Powalla, "Systematic survey of suitable buffer and high resistive window layer materials in CuIn1-xGaxSe2 solar cells by numerical simulations" *Solar Energy Materials & Solar Cells,* vol. 165, 2017, pp. 119-127. [Online]. doi: 10.1016/j.solmat.2016.12.035

[36]   I. Gharibshahian, S. Sharbati, and A. Orouji, "Potential efficiency improvement for Cu(In, Ga)Se2 thin-film solar cells by the window layer optimization" *Thin Solid Films,* vol. 655, 2018, pp. 95-104. [Online]. doi: 10.1016/j.tsf.2018.04.014

[37]   M. Gloeckler, "Device physics of Cu(In,Ga)Se2 thin-film solar cells", Ph. D dissertation, Dept. of Physics, Colorado State University, Fort Collins, CO, 2005. [Online]. Available: https://www.yumpu.com/en/document/read/50809695/device-physics-of-cuingase2-thin-film-solar-cells-the-

[38]   S. Lee, J. Lee, Y. Lee, B. Min, and M. Shin, "Numerical simulation of CIGS solar cell for defect modeling" in *IEEE 7th World Conf. on Photo. Energy Conversion (WCPEC)*, 2018, pp. 1914-1917. [Online]. doi: 10.1109/PVSC.2018.8547778

[39]   A. Khadir, A. Gueddim, M. Abdelhafidi, and L. Gacem, "Optimization and design of gallium gradients for CIGS thin film solar cells high efficiency" in *1st Intl. Conf. on Sustainable Renewable Energy Sys. And App. (ICSRESA)*, 2019, pp. 1-5. [Online]. doi: 10.1109/ICSRESA49121.2019.9182681

[40]   F. Troni, F. Dodi, G. Sozzi, and R. Menozzi, "Modeling of thin-film Cu(In,Ga)Se2 solar cells" in *Intl' Conf. on Sim. Of Semiconductor Processes and Devices (SISPAD)*, Article ID 03-A.2, 2010, pp. 33-36. [Online].

[41]   National Renewable Energy Lab (NREL), "Best research-cell efficiency chart." Accessed October 21, 2021 [Online]. Available: https://www.nrel.gov/pv/cell-efficiency.html

INITIAL DISTRIBUTION LIST

1. Defense Technical Information Center
    Ft. Belvoir, Virginia

2. Dudley Knox Library
    Naval Postgraduate School
    Monterey, California